2010

Development Of An Improved Microwave Ocean Surface Emissivity Radiative Transfer Model

Salem El-Nimri
University of Central Florida

DEVELOPMENT OF AN IMPROVED MICROWAVE OCEAN SURFACE EMISSIVITY RADIATIVE TRANSFER MODEL

by

SALEM FAWWAZ EL-NIMRI
M.S. University of Central Florida, 2006

A dissertation submitted in partial fulfillment of the requirements
for the degree of Doctor of Philosophy
in the School of Electrical Engineering and Computer Science
in the College of Engineering and Computer Science
at the University of Central Florida
Orlando, Florida

Spring Term
2010

Major Professor: W. Linwood Jones

ABSTRACT

An electromagnetic model is developed for predicting the microwave blackbody emission from the ocean surface over a wide range of frequencies, incidence angles, and wind vector (speed and direction) for both horizontal and vertical polarizations. This ocean surface emissivity model is intended to be incorporated into an oceanic radiative transfer model to be used for microwave radiometric applications including geophysical retrievals over oceans. The model development is based on a collection of published ocean emissivity measurements obtained from satellites, aircraft, field experiments, and laboratory measurements. This dissertation presents the details of methods used in the ocean surface emissivity model development and comparisons with current emissivity models and aircraft radiometric measurements in hurricanes.

Especially, this empirically derived ocean emissivity model relates changes in vertical and horizontal polarized ocean microwave brightness temperature measurements over a wide range of observation frequencies and incidence angles to physical roughness changes in the ocean surface, which are the result of the air/sea interaction with surface winds. Of primary importance are the Stepped Frequency Microwave Radiometer (SFMR) brightness temperature measurements from hurricane flights and independent measurements of surface wind speed that are used to define empirical relationships between C-band (4 – 7 GHz) microwave brightness temperature and surface wind speed. By employing statistical regression techniques, we develop a physical-based ocean emissivity model with empirical coefficients that depends on geophysical parameters, such as wind speed, wind direction, sea surface temperature, and observational

parameters, such as electromagnetic frequency, electromagnetic polarization, and incidence angle.

To The Person Who Gave Life a Meaning, a Milestone has Passed, Hand By Hand Together We Made It

To My Beloved Wife:

Ruba Amarin El-Nimri

Deep Appreciation to the People Who Brought Me to Life, and Taught Me How to Reach For the Skies, To My Parents

Fawwaz El-Nimri Maysoon El-Nimri

To the Flowers of My Life ... Sandy, Batool and Sireena

ACKNOWLEDGMENT

I would like to thank my advisor Prof. Linwood Jones for all the hard work, dedication, and support he provided throughout my graduate years, it was his vision and trust that gave me the opportunity to excel. He taught me that with hard work nothing is impossible.

Also I would like to thank my committee members, Dr. Timothy Miller, Dr. Peter Gaiser, Dr. Takis Kasparis, Dr. Parveen Wahid, Mr. James Johnson, for their guidance, advice, interests and time. Also, I am thankful to my team members at the Central Florida Remote Sensing Lab. CFRSL, for their assistance especially Liang Hong, Pet Laupattarakasem, and Rafik Hanna.

I would like to give my warmest appreciation to Suleiman Al Sweiss and Diala Gammoh whose support was a major driver that made this journey enjoyable.

Finally, I wish to acknowledge the financial support provided by the HIRAD project. This work was funded under Subcontract SUB2006-226 with the Von Braun Center for Science and Innovation, Inc., Huntsville, AL, in collaboration with NASA/Marshall Space Flight Center and NOAA in the development of the HIRAD instrument. Also this work was accomplished with the help of NOAA's through Dr. Peter Black and Dr. Eric Uhlhorn.

TABLE OF CONTENTS

LIST OF FIGURES

LIST OF TABLES

LIST OF ACRONYMS / ABBREVIATIONS

SST	Sea Surface Temperature
CFRSL	Central Florida Remote Sensing Lab
RTM	Radiative Transfer Model
EIA	Earth Incidence Angles
NOAA	National Oceanic and Atmospheric Administration
NESDIS	National Environmental Satellite Data and Information Service
SFMR	Stepped Frequency Microwave Radiometer
TPC	NOAA Tropical Prediction Center
NHC	NOAA National Hurricane Center
HRD	NOAA Hurricane Research Division
WCC	White Caps Coverage
HIRAD	Hurricane Imaging Radiometer
IFOV	Instantaneous Field of View
NASA	National Aeronautics and Space Administration
ESMR	Electronically Scanned Microwave Radiometer
SMMR	Scanning Multichannel Microwave Radiometer

CHAPTER 1 : INTRODUCTION

Passive microwave remote sensing is a major source of environmental observations for scientific and operational applications. This technology is especially useful for surface remote sensing because of the ability of microwave radiation to have high atmospheric transmissivity even through clouds and in severe weather and during day or night. Therefore, passive microwave sensors play an important role in providing measurements of important atmospheric, oceanic, terrestrial, and ice environmental parameters for scientific research and operational utilization by a number of civilian and federal governmental users.

1.1 Objective

With today's spaceborne and airborne microwave radiometer technologies, it is possible to obtain a variety of geophysical parameters from the measured microwave blackbody emissions over the ocean. This emission comes primarily from the ocean surface with a significant component from a slightly opaque atmosphere. Microwave radiative transfer models (RTM) need to have a robust ocean surface emissivity model that relates the measured emission to geophysical parameters. Geophysical parameters like sea surface temperature (*SST*), salinity, and wind vector (wind speed and wind direction) have significant effect on the ocean emission.

For ocean remote sensing applications, radiative transfer models are used to retrieve geophysical parameters, such as sea surface temperature (*SST*), salinity and surface wind vector, and RTM's are also used to simulate brightness temperatures for radiometric calibration and

instrument design and development. It is important to have RTM's that can accurately simulate measurements over a wide range of environmental parameters, measurement geometry and operating frequencies. Surface emissivity models represent the most important part in any RTM since the majority of the emission comes from the surface.

Ocean emissivity can be partitioned into two parts, namely; smooth and wind induced rough ocean surface emissions. Smooth emission is well defined by the Fresnel power reflection coefficient, which depends on the electromagnetic polarization, the viewing angle of the radiometer and the dielectric constant of sea water. Further the dielectric constant of sea water is calculated by the Debye equation as a function of frequency and geophysical parameters such as salinity and sea surface temperature. Also the roughening of the surface causes increased emissivity, which is analytically complex and mostly empirically based.

Well calibrated ocean emissivity models like Wentz [1], Weilheit [2, 3], Stogryn [4], and Uhlhorn [5] have been used in RTM's to retrieve ocean geophysical parameters. Unfortunately most surface emissivity models are specialized in their applicable regions, whether it is frequency, incidence angle, or wind speed, and they cannot be easily extrapolated to other regimes where empirical data are not available. For the development of future microwave remote sensing systems with expanded ranges of applicability, these limitations define the advantage for a unified ocean surface emissivity model, which is the goal of this dissertation.

This dissertation provides a physics-based microwave ocean surface emissivity model that characterizes the sea surface microwave blackbody emissions independent of microwave instrument and measurement geometry. It was derived from analysis of radiometer measurements of surface emission at various incidence angles, frequencies, polarizations, and

surface wind speeds and directions. We believe that this model will have applicability to a variety of airborne or satellite radiometer systems (e.g., conical scanning imagers, cross-track searching sounders and push brooms) that are presently available or planned for the future.

Our goal is the development of an ocean surface emissivity model, which provides an accurate prediction of linearly polarized microwave brightness temperature over a wide range of ocean wind speeds from calm to hurricane force winds, frequencies from 1 GHz to 200 GHz, and earth incidence angles (*EIA*) from nadir to > 70°. The model will be useful in engineering design studies of passive microwave remote sensing instruments, for radiometric calibration over oceans, and for developing geophysical retrieval algorithms.

This dissertation is organized into five chapters. Following this introduction, chapter two presents the sea surface emissivity model that was adopted in this work along with a description to its parameters. Chapter three describes the multi-variant regression procedure used in the development of the total ocean emissivity model as a function of wind speed, wind direction, earth incidence angle, and radiometer frequency. Chapter four gives results of model comparisons with current and previous surface emissivity models and radiometer measurements. The dissertation concludes with a brief summary and conclusion in chapter five.

CHAPTER 2 : MICROWAVE RADIATION TRANSFER THEORY FOR AN OCEAN SCENE

According to microwave radiative transfer theory [6], greybody radiation or apparent brightness temperature (T_{app}) received by an airborne or satellite microwave radiometer is the sum of three emission (brightness temperature) components as shown in Fig. 2.1:

1. Emission from the surface (T_{sur}),
2. Additive down-welling atmospheric and galactic radiation (T_{sky}) that is reflected upward at the surface (T_{refl}), and
3. Upwelling atmospheric radiation (T_{up}).

T_{app} is the equivalent blackbody physical temperature that produced the observed noise flux density (W/m^2/steradian). For emissive media, each component of brightness temperature (T_b) is,

$$T_b = \varepsilon * T_{phy} \tag{2.1}$$

Where,

T_{phy} is the physical temperature of its medium,

ε is the medium emissivity.

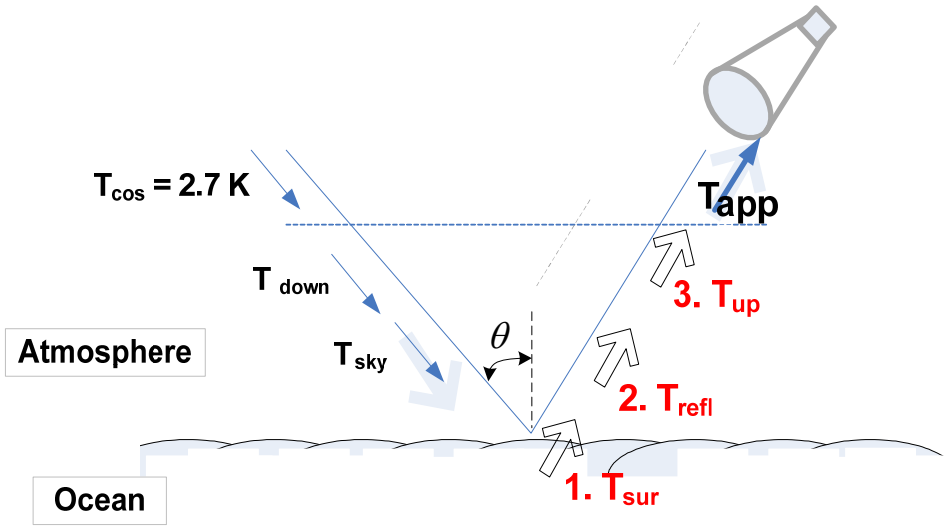

Figure 2.1 Simplified microwave radiative transfer over the ocean at incidence angle θ.

As illustrated in Fig. 2.1, brightness components T_{refl} and T_{sur} are also attenuated by the intervening atmosphere between the surface and the observer, therefore, the total apparent brightness temperature, T_{app}, at the radiometer antenna aperture is modeled as follows:

$$T_{app} = T_{up} + e^{-\tau}\left(T_{sur} + T_{refl}\right) \tag{2.2}$$

where,

$$T_{refl} = \left(T_{\cos}\, e^{-\tau} + T_{down}\right) * \Gamma \tag{2.3}$$

Where T_{up} and T_{down} are the integrated upwelling (downwelling) atmospheric emission component along the antenna line of sight, T_{sur} is the surface emission, T_{cos} is the cosmic microwave brightness background, which is equal to 2.73 K, T_{ref} is the specular reflected sky atmospheric emission component, and $e^{-\tau}$ is the atmospheric transmissivity. Therefore, the ocean surface is characterized by the brightness temperature (T_{sur}) and the atmosphere is characterized by the optical opacity, τ, as shown in Eq. (2.4).

$$\tau = \int_0^H \tau(z) sec\theta dz \tag{2.4}$$

where,

H is the height,

$$\tau(z_{i-1}, z_i) = \int_{z_{i-1}}^{z_i} k(z) dz$$

$k(Z_i)$ is the total atmospheric absorption coefficient from oxygen (O_2), cloud liquid water (CLW), nitrogen (N_2), water vapor (WV) and precipitation (liquid and frozen) at layer i combined in units of Nepers/unit-length.

2.1 Sea Surface Emissivity

Surface emissivity is the ratio of radiation, which is defined as power flux density per solid angle, emitted by a surface to the theoretical blackbody radiation predicted by Planck's law, and this radiation transfer is illustrated in Fig. 2.2. Within the ocean media, the radiation

emission is isotropic blackbody; but because of differences in the characteristic impedances of air and sea water, there is internal reflection that blocks a portion of this blackbody radiation from crossing the air/sea interface. Based upon the conservation of energy at the interface, the surface emissivity may be expressed as,

$$\varepsilon = 1 - \Gamma \tag{2.5}$$

where,

Γ = power reflection coefficient = $|\rho|^2$, and

ρ = Fresnel voltage reflection coefficient.

This specular emissivity is applicable to the intersection of two semi-infinite media, where the surface is "flat" with root-mean-square height variations very much smaller than the wavelength of the EM wave. The emissivity is equal to the power transmission coefficient for the refracted wave (blackbody microwave emission within the air). The specular emissivity depends on incidence angle, EM polarization and the complex relative dielectric constants for both media (air/sea water).

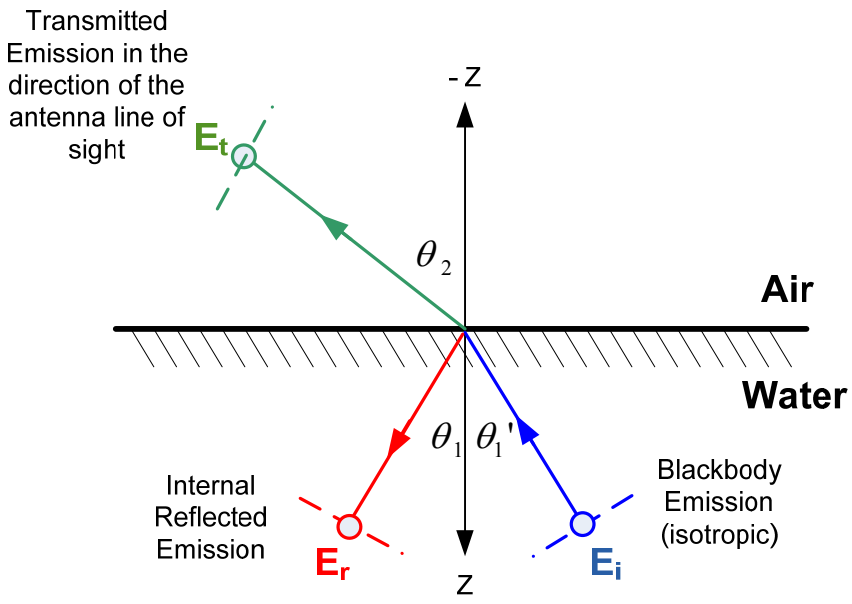

Figure 2.2 Plane wave electric field reflection and transmission at the ocean/ air interface.

Because of the large changes in the dielectric properties of materials in the microwave region of the electromagnetic (EM) spectrum, microwave remote sensing uses this to its advantage to infer geophysical properties of media and to distinguish between different media types (e.g., ocean, land and ice). This is in contrast with the infrared portion of the EM spectrum, where most media are blackbodies (emissivity is nearly unity), which enables IR to measure physical temperature but not to distinguish different media.

Typically, knowledge of emissivity to an accuracy of order 10^{-3} - 10^{-4} is required to retrieve physical parameters from T_b measurements. The importance of this for ocean remote sensing is that surface emissivity affects the magnitude of two T_b components of the radiative transfer model, namely, the calculation of the reflected down-welling atmospheric emission and the emission from the ocean surface.

2.2 Sea Surface Emissivity

Traditionally, the sea surface emissivity (ε_{ocean}) has been modeled as the sum of a specular emissivity (ε_{smooth}) (based upon the Fresnel power reflection coefficient) plus an additive rough surface emissivity (ε_{rough}) that has been empirically determined such as in Stogryn [4],

$$\varepsilon_{ocean} = \varepsilon_{smooth} + \varepsilon_{rough} \tag{2.6}$$

Furthermore the emission for a rough ocean surface is subdivided into two parts:

a. Emission due to small-scale ocean wave generated by the action of the wind frictional velocity, and

b. Emission due to sea foam on the surface.

The contribution of each in the total surface emission will be described in the following sections.

2.2.1 Fresnel Voltage Reflection Coefficient

For a microwave radiometer viewing a smooth ocean surface through a non-attenuating atmosphere, the emission reduces to only the direct surface emission component. The EM propagation across the air/sea interface depends upon the difference in the characteristic impedances of the two media.

Fresnel's equations describe the electric field (voltage) reflection and transmission for transverse EM waves at the interface of two semi-infinite dielectric media [7]. Consider Fig. 2.3

that illustrates the behavior of an incident plane wave in the atmosphere propagating towards the sea surface. A fraction of the signal crosses the interface and is refracted at an angle θ_2, and the other part is reflected at an angle θ_1`. In remote sensing, we are interested in the intensity (energy) of both the reflected downwelling T_b (Fig. 2.3) and the sea surface T_b (Fig. 2.2) that are collected by the radiometer, because they are directly affected by the surface emission.

The following voltage reflection coefficient equations apply to both Fig. 2.2 and Fig. 2.3. The electric field components both parallel and perpendicular to the plane of incidence are governed by Eqs. (2.7) & (2.8), respectively (vertical and horizontal polarization respectively). Snell's Law is used to calculate the directions (angles) of the incident, reflected and transmitted rays according to Eq. (2.9) [8].

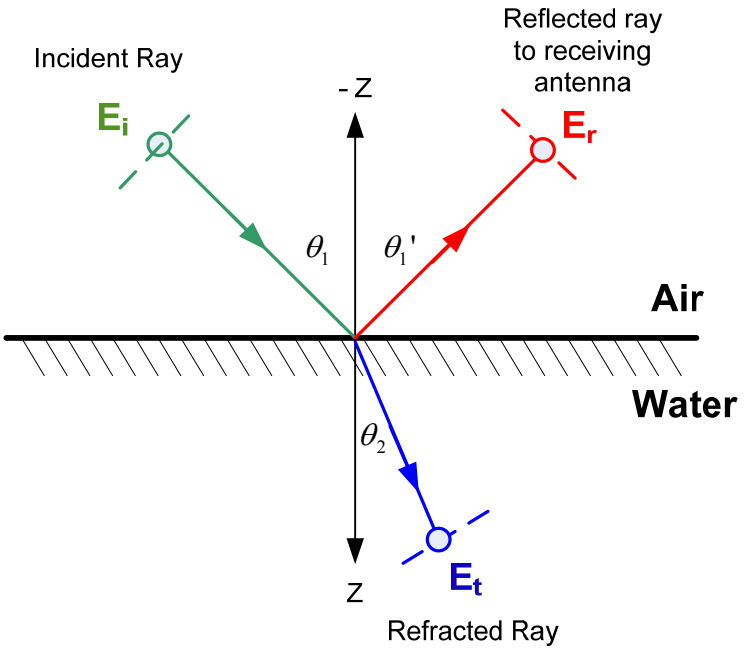

Figure 2.3 Specular reflected atmospheric component of microwave emission at the air/ocean interface.

$$\rho_{V-pol} = -\left[\frac{e_{r2}\cos\theta - \sqrt{e_{r2} - \sin^2\theta}}{e_{r2}\cos\theta + \sqrt{e_{r2} - \sin^2\theta}}\right] \tag{2.7}$$

$$\rho_{H-pol} = \left[\frac{\cos\theta - \sqrt{e_{r2} - \sin^2\theta}}{\cos\theta + \sqrt{e_{r2} - \sin^2\theta}}\right] \tag{2.8}$$

where e_{r2} is the sea water relative complex dielectric constant (e_{r1} = 1.0 for air) and $\theta = \theta_1 = \theta_1'$ is the earth incidence (reflected) angle in degrees.

$$n_1 \sin(\theta_1) = n_2 \sin(\theta_2) \tag{2.9}$$

where n_i = index of refraction and i = media 1 or media 2.

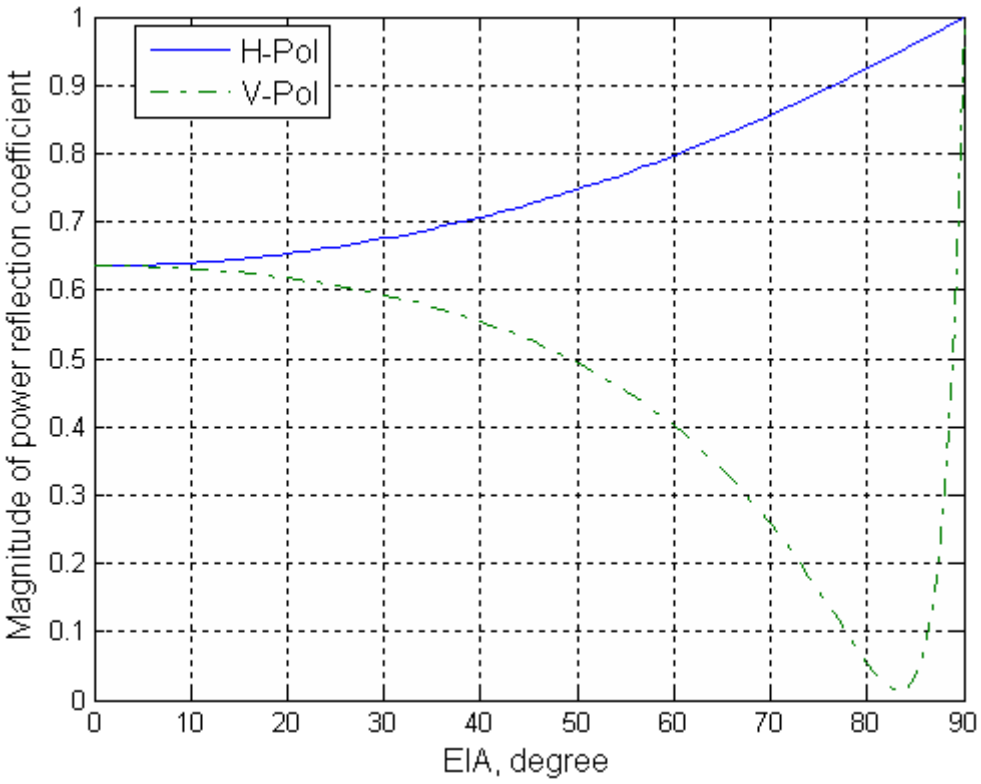

Figure 2.4 Typical ocean power reflection coefficient for 4.55 GHz, 25 °C *SST* and 36 ppt salinity.

In Fig. 2.4, the H-pol power reflection coefficient increases monotonically to unity reflection at an incidence angle of 90 deg, and the V-pol curve decreases and reaches zero reflection at an angle ~ 83 deg; this phenomenon is known as the Brewster angle. At this incidence angle, there is no reflection and the wave passes through the interface without refraction. Beyond the Brewster angle, the reflection rapidly increases to 100% at 90 deg.

Precise knowledge of the complex dielectric constant (permittivity) ε_{r2} of water is essential for calculating the radiative transfer coefficient of microwave radiation that is emitted

by the ocean surface. The dielectric constant is a function of frequency (*freq*), sea surface water temperature *(SST)* and salinity *(S)*, as shown in the Debye equation [8].

$$\varepsilon_r = \varepsilon_\infty + \frac{\varepsilon_s - \varepsilon_\infty}{1 + \left(\frac{j\lambda_R}{\lambda}\right)^{1-\eta}} - j\left(\frac{2\sigma\lambda}{c}\right) \tag{2.10}$$

where the parameters are determined by laboratory measurements,

$j = \sqrt{-1}$,

λ = radiation wavelength (*c/freq*),

ε_∞ = dielectric constant at infinite frequency,

ε_S = static dielectric constant at zero frequency,

λ_R = relaxation wavelength a parameter of sea water,

η = spreading factor, a parameter of sea water,

σ = is the ionic conductivity, which is *f(salinity, SST, freq)*,

Salinity is the mass ratio of dissolved salt to water per unit volume, parts-per-thousand (ppt)

c = is the speed of light.

Over the past four decades, several Debye models have been developed using experimental microwave measurements of pure and saline water [9-11], but the latest and the one that is used in this dissertation was developed by Meissner and Wentz [12] , which is based on

the results from Stogryn [10] and Klein and Swift [9] except that the functional dependence on salinity (S) and ε_∞ have been changed to match satellite radiometer measurements over a wide range of frequencies. For illustration purposes, Fig. 2.5 shows the real and imaginary parts of the dielectric constant versus frequency for fresh (salinity = 0 ppt) and salt water (salinity = 10, 20 and 36 ppt) at a sea surface temperature of 25 °C.

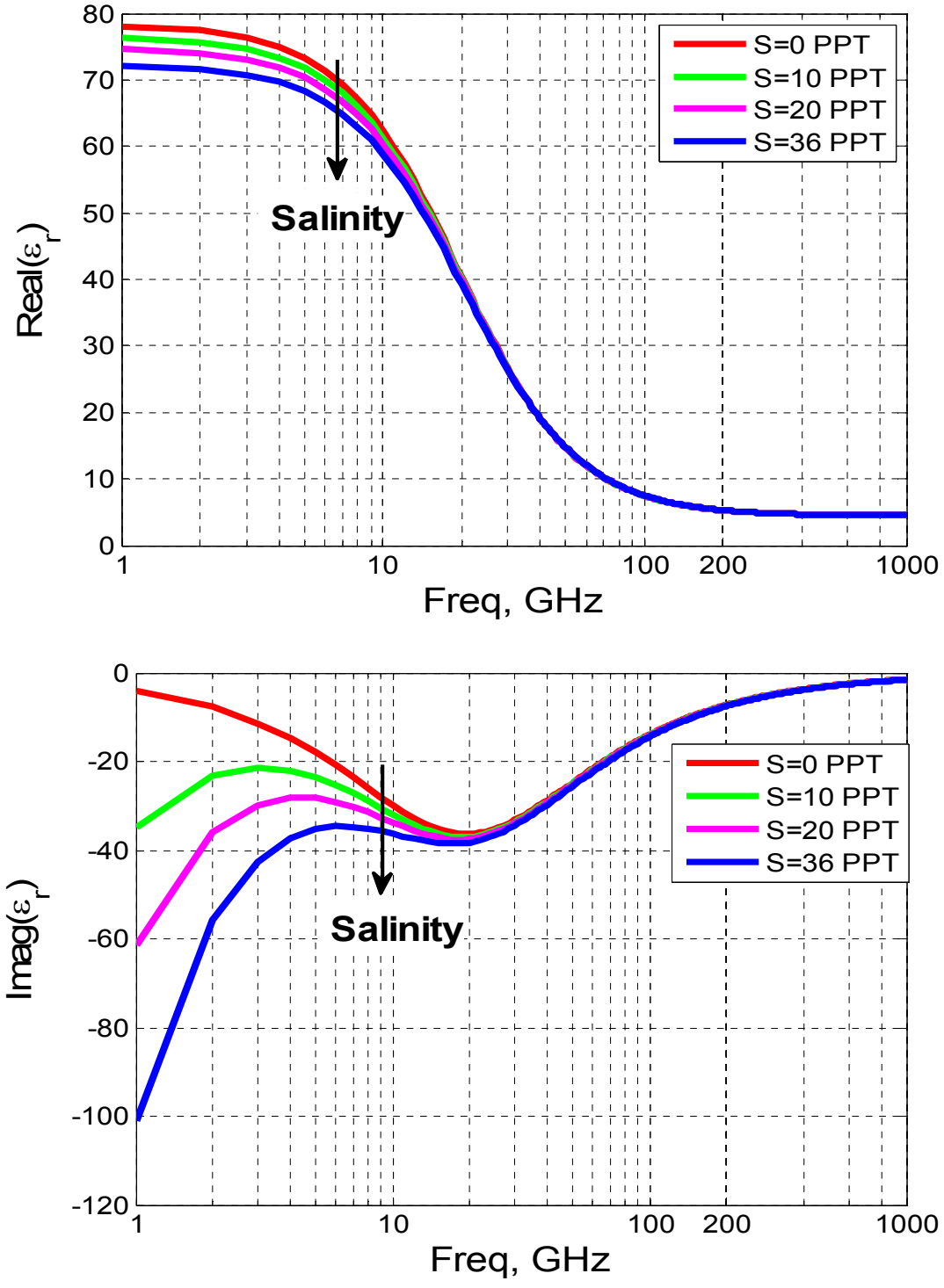

Figure 2.5 Real part (upper panel) and imaginary part (lower panel) of dielectric constant for saline (10, 20 and 36 ppt) and pure water at sea surface temperature of (25°C).

2.2.2 Smooth Sea Water Emissivity

The smooth water (specular) emissivity is determined using the principal of the conservation of energy at the air/sea interface, as discussed earlier in section 2.2.1. Emissivity depends on Fresnel power reflection coefficient, which is a function of the polarization of the EM wave, the direction of propagation (incidence angle), and the complex dielectric constant of sea water. Also the sea water complex dielectric constant varies with the geophysical parameters; sea surface temperature, salinity, and the EM frequency. A typical example of the smooth water emissivity is given in Fig. 2.6, where the emissivity response with incidence angle is the reciprocal of the power reflection coefficient, where V-pol increases and H-pol decreases versus incidence angle.

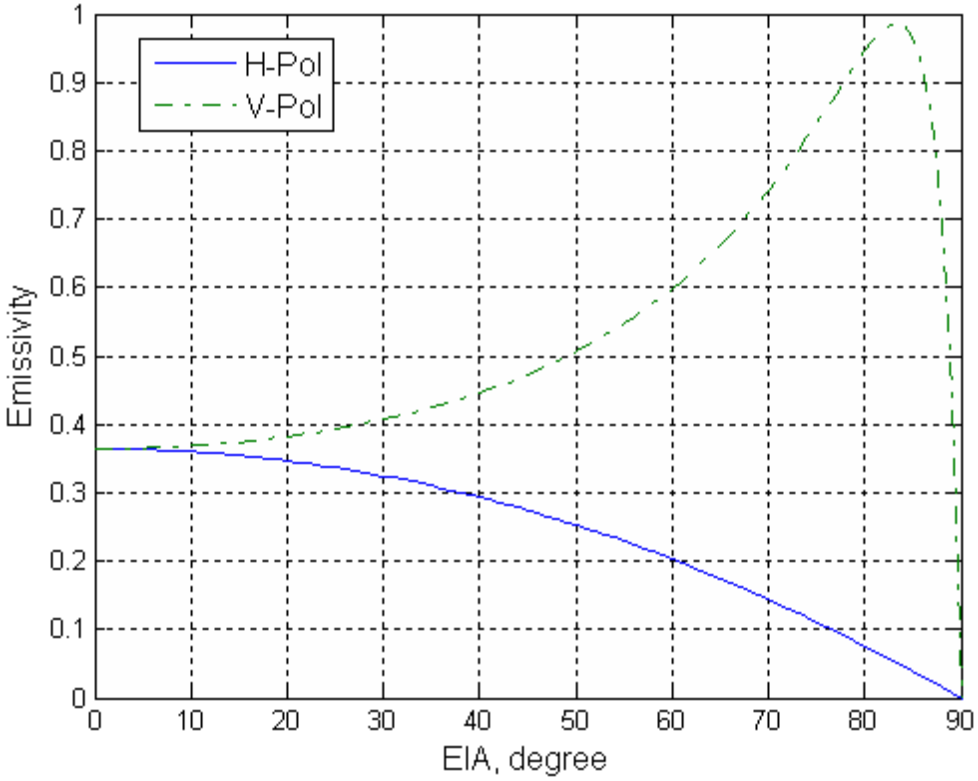

Figure 2.6 Typical smooth sea water emissivity for 4.55 GHz, 25°C SST, and 36 ppt salinity.

2.2.3 Rough Sea Surface Emissivity

Since the ocean surface is a boundary interface, a calm ocean with negligible wind speed results in specular reflection where the Fresnel formulas describe the reflection and emission as previously explained. As wind blows over the ocean surface, small-scale capillary waves form and the surface roughness increases, which leads to dramatic change in the reflection and emission characteristics as a function of the surface wind speed. Historically, these have been modeled as an additive emissivity term [2, 4, 13, 14], which depend upon the drag force of the surface wind. We can relate the variation of the surface emissivity to three mechanisms:

1. Geometry changes due to short ocean waves,
2. Geometry changes due to long ocean waves, and
3. Sea foam.

The first has to do with diffraction of microwaves by short ocean (capillary and short gravity) waves whose lengths are comparable to the radiation wavelength. The second mechanism occurs with long ocean (gravity) waves whose lengths are very long compared to the radiation wavelength, which tilt the surface, and thereby mix the H- and V- polarizations and change the incidence angle of the incident wave. Both mechanisms can be treated using a two-scale EM model of ocean facets that have their own reflection coefficient [2, 4]. The third mechanism deals with the generation of sea foam caused by breaking gravity ocean waves. This has a large effect at high wind speeds due to the high emission of foam for both polarizations. All three mechanisms can be parameterized in terms of the surface wind speed (at a height of 10m) and relative wind direction (defined as the differential azimuth viewing direction of the radiometer antenna relative to the wind direction).

Optical experiments conducted by Cox and Munk [15] measured the slope spectrum of the ocean surface caused by surface winds. They based their findings on sun light scattering from the rough ocean surface. Microwave radiative transfer modelers such as Stogryn [4] have used these results of Cox and Munk to model the microwave ocean emission as a function of the 10m surface wind speed, microwave frequency and polarization. These models have been empirically verified over a range of wind speeds and *EIA*'s, in numerous field measurements using ocean

platforms, aircraft and satellite measurements [2, 13, 14]. An example of the Stogryn model calculated smooth and rough emissivity for 4.55 GHz radiometer frequency is given in Fig. 2.7. Three curves of ocean emissivity are plotted for zero, 5 and 10 m/s wind speeds, which have no significant foam cover.

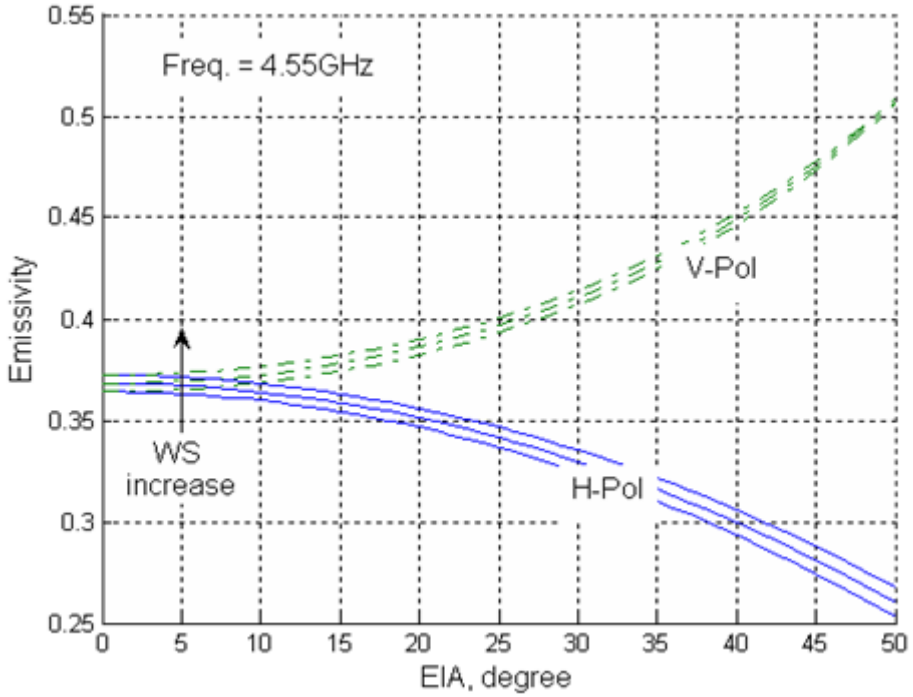

Figure 2.7 Ocean emissivity for 4.55 GHz and wind speeds of zero, 5 and 10 m/s.

2.3 Sea Foam

The nonlinear transformation of ocean wave energy from short to long wavelengths causes the gravity ocean wave heights and slopes to grow until they break and produce "white caps" and foam. Most microwave ocean emissivity models treat sea foam as an approximate blackbody with low reflectivity and near-unity emissivity. Foam is responsible for increasing the emission from the foam-covered sea surface. The generally accepted hypothesis is that, sea foam is a medium comprising many small air bubbles that float on the ocean surface and produce an impedance matching layer for the propagating EM waves (blackbody radiation in the sea water medium). This reduces the internal blackbody radiation reflection at the air/sea interface, which increases the ocean surface emissivity. Since the emissivity of foam is approximately twice that of sea water, understanding the EM characteristics of foam and how it is produced and distributed over the ocean surface is crucial to calculating the rough surface emissivity.

2.3.1 Effect of Foam on Oceanic Emission

Many laboratory studies and field experiments have been conducted to determine foam emission as a function of microwave frequency, polarization and incidence angle [16, 17]. Based upon these experimental results, there are two major assumptions in modeling foam for a spaceborne or airborne radiometer. The first assumption is that there is a statistical randomness in area-coverage distribution over the antenna foot print (instantaneous field of view, IFOV) but that each radiometer measurement contains the same mean area coverage of foam. The second, and most important, is that there exists a statistically stationary relationship between foam area

coverage and surface wind speed. Most ocean emissivity modelers treat foam emissivity as a function of frequency and incidence angle [17, 18], but others combine the emission due to foam with other factors [1, 2].

Also, in this dissertation, it was found that foam emissivity is related to wind speed at certain microwave frequencies, as will be discussed later in this dissertation.

2.3.2 Emissivity of Foam

In 1970, an interesting attempt at a theoretical description of the emissivity of foam was made by Droppleman [16], where he concluded that the complexity of the EM boundary value problem precluded the construction of a physically and mathematically convincing theoretical model. Thus, at least for the present, complete reliance must be placed on experimental data in studies relating to the radiometric effects of foam and its relationship with frequency and incidence angle.

In 1972, Stogryn [17] developed an empirical expression for sea foam emissivity as a function of sea surface temperature, frequency, and incidence angle based on a review of previously published measurements of foam-covered sea surface. Recently, Rose et. al. [18] performed experiments at frequencies of 10 and 37 GHz for the range of incidence angle from 30° to 60°. Further, Padmanabhan et. al. [19] performed foam emissivity experiments at three frequencies (10, 19 and 37 GHz) for 53° incidence. Camps et. al. [20] has also performed studies of foam emissivity at L-band (1.4 GHz). Many theoretical studies have been conducted develop a

physical based model for the emissivity of foam [18, 20, 21], yet these studies have yet to converge to a realistic model because the foam bubble size, diameter and distribution are difficult to relate to open ocean conditions.

2.3.3 Foam Fraction - Wind Speed Dependence

Based upon empirical results, the formation of foam is highly correlated with surface wind speed and the breaking of gravity ocean waves. Foam fraction or area percentage of foam coverage increases with wind speed and is randomly distributed over the ocean surface on a spatial scale of 10's of meters. Because radiometer antennas have footprints on the ocean surface of that range from 100's meters diameters (airborne) to 10's of kilometers (satellites), the foam fraction (% area cover) will appear uniformly distributed in an average sense. A recent study, to characterize the increase of foam fraction, used aerial photography taken at low-altitudes in hurricanes to study the white caps coverage (WCC) and foam area coverage with wind speed [22].

It is likely that other physical parameters such as significant wave height, air/sea temperature difference may also affect the foam fraction. Further, foam fraction is, obviously, independent of the radiometer parameters; frequency, polarization and incidence angle; and therefore for our model, it is modeled as a function of wind speed only. Foam first appears on the ocean surface at wind speeds of approximately 6 m/s, where breaking waves start to form; and it increases approximately exponentially with wind speed. For example, from this

dissertation analysis at wind speed of 40 and 70 m/s, the foam coverage is estimated to be about 4% and 73 % respectively. At higher wind speeds, we assume that the percentage foam cover asymptotically approaches 100 %.

The detailed formation of the adapted total emissivity model will be presented in chapter 3 and results of comparisons with other surface emissivity models will be presented in chapter 4 that follows.

2.4 Wind Direction

Another important factor in the ocean rough emissivity is the wind direction. According to EM theory by Yueh [23] it follows that both V and H -pol radiation emitted from the ocean surface are anisotropic periodic functions of the relative wind direction. A common model is given by,

$$\varepsilon_i = \varepsilon_{i0} + E_{i1} * cos\,(x) + E_{i2} * cos\,(2x) \tag{2.11}$$

where,

ε_{i0} is the total isotropic ocean emissivity (smooth & rough),

ε_i is the total ocean emissivity,

i is the V and H polarization, and

x is the relative wind direction.

The second and third terms in Eq. (2.11) represent the 1st and 2nd harmonics, which are zero mean additive terms to the isotropic ocean surface emissivity represented by the first term in Eq. (2.11).

Coefficients E_{i1} and E_{i2} have been found to be sensitive to radiometer look angle (*EIA*), frequency and ocean surface wind speed. It was found that the 1st harmonic (E_{i1}) is sensitive to the upwind/ downwind T_b ratio and the 2nd harmonic (E_{i2}) is sensitive to the upwind/ crosswind T_b ratio. Many researchers have empirically derived these coefficients [23-25], but they limited their modeling to bounded regions, in terms of limited ranges of wind speeds, *EIA*'s, and frequencies. A new approach that combines these results is presented in this dissertation.

CHAPTER 3 : WIND SPEED EMISSIVITY MODEL DEVELOPMENT

Experimentally, it has been observed that the surface wind over the ocean exhibits a strong modulation of the brightness temperature because changes in the ocean surface emissivity affect both the direct radiometric emission from the sea surface as well as the reflected downwelling brightness temperature from the atmosphere. Unfortunately, theoretical radiometric modeling of this rough surface emissivity has been challenging and of only limited success. One reason for this is that the small-scale ocean wave characteristics and their dependence on frictional wind drag at the ocean's surface are not well understood mostly due to the difficulty of obtaining the simultaneous wind and short ocean wave spectrum measurements in the open ocean environment. As a result, radiometric modelers have developed empirical relationships between the near surface wind speed (measured at 10 m height) and the observed change in brightness temperature.

In this dissertation, the total ocean surface emissivity model will be expressed as shown in Eq. 3.1, which is consistent with Eq. (2.11)

$$\varepsilon_{total} = \varepsilon_{ocean} + \Delta\varepsilon_{wind\ direction} \tag{3.1}$$

where,

ε_{ocean} is the isotropic ocean surface emissivity, and

$\Delta\varepsilon_{wind\ \ direction}$ is the zero mean anisotropic wind direction component of the total emissivity.

In this chapter, selected models will be described as they relate to this dissertation development of an ocean surface emissivity model.

3.1 Historical Perspective

Over nearly three decades between the mid-1960 to mid-1990, there were many researchers investigating the effect of wind speed on the ocean brightness temperature. For example:

(1) Stogryn [4] developed a theory to account for the wind speed induced roughness. He analyzed T_b measurements at 19.4 GHz and noticed that the dependence of the rms slope of the sea on wind speed for horizontal polarization at 50 degrees is larger than the vertical polarization where it is almost independent of the sea state.

(2) Hollinger [13] at the Naval Research Laboratory performed experiments using radiometers operating at 1.41, 8.36, and 19.34 GHz from the Argus Island tower to investigate this phenomenon. During these experiments, there were a number of environmental parameters measured including *SST*, wind speed and direction, ocean gravity-wave spectrum and video photography, which allowed breaking waves and foam to be simultaneously recorded. After careful editing of the microwave data to eliminate measurements associated with foam, Hollinger cross-correlated the increase on microwave T_b with wind speed effect, and concluded that the roughness effect was less than that predicted by Stogryn by a frequency dependent factor.

(3) Nordberg et. al. [26] at the NASA Goddard Space Flight Center conducted airborne radiometric experiments using a 19.35 GHz Electronically Scanned Microwave Radiometer

(ESMR) prototype of the Nimbus-5 instrument. Based upon their observations in ocean storms, they characterized the combined foam and roughness effect at 19.35 GHz, where foam was showed to be the dominant factor.

(4) Wu and Fung [27] and later Wentz [14] extended Stogryn geometric optics theory to include diffraction effects, multiple scattering, and two-scale partitioning.

(5) Wilheit and Fowler [28] were the first to perform a simultaneous retrieval of wind speed, water vapor, and cloud liquid water based on airborne data from the 1973 joint US-USSR Bering Sea Experiment (BESEX).

(6) Chang and Wilheit [29] combined two NIMBUS-5 instruments, the ESMR and the NEMS for wind speed, water vapor, and cloud liquid water retrieval.

(7) Wilheit [30] also used the 37 GHz dual polarized data from the Electrically Scanned Microwave Radiometer (ESMR) to explore the wind speed induced roughness of the ocean surface. This was later combined with other data to generate a semi-empirical model for the ocean surface emissivity [2] in preparation for the 1978 launch of the Scanning Multichannel Microwave Radiometer (SMMR) on the Nimbus-7 and SeaSat-A satellites.

(8) Wentz et. al. [31] made a major improvement in the wind retrieval by combining the SeaSat SMMR T_b's and the SeaSat scatterometer (SASS) wind retrievals to develop an accurate, semi-empirical relationship for the wind-induced emissivity.

(9) Goodberlet et. al. [32], following the launch of the Special Sensor Microwave Imager (SSM/I) in 1987, developed a statistical regression wind speed algorithm, which performed reasonably well but provided no information on the relevant physics.

(10) Schluessel and Luthardt [33] and Wentz [34, 35] developed a more physical approach to algorithm development for SSM/I, which yielded improved oceanic (wind speed) and atmospheric geophysical parameter retrievals.

These researchers have contributed to the development of a number of ocean emissivity models that perform well over specific ranges of wind speed, frequency & incidence angle. Unfortunately, the narrow range of applicability for the current emissivity models makes them difficult to be extrapolated to other regimes that are important for the development of future remote sensing systems. The motivation of this dissertation is to develop a unified surface emissivity model that has a physical-basis with empirical coefficients, which are derived from currently available radiometric measurements and surface emissivity models. The goal is to integrate these into a single ocean emissivity model with a wide range of applicability.

3.2 Existing Wind Speed Emissivity Models

For smooth ocean surfaces, Fresnel power reflection coefficients are used to model the emissivity with respect to frequency, polarization and incidence angle as given in Eq. (2.5), (2.7) and (2.8). For slightly rough surfaces (wind speeds < 7 m/s), there are both quasi-theoretical and strictly empirical approaches that are reasonably successful in predicting the observed ocean brightness temperature.

Beyond 7 m/s, the breaking of ocean gravity waves creates localized regions (patches) of sea foam and entrained air bubbles near the surface, which exhibits high emissivity. The foam percentage area coverage (also known as foam fraction) varies with the significant wave height

and fetch, which is highly correlated to the time integral of the surface wind speed. Thus, to accurately model the ocean emissivity, the foam fraction must be precisely known, and empirical foam fraction models exist to estimate this parameter as a function of the mean surface wind speed at 10 m height. Radiometrically, the brightness temperature of the ocean is treated as a linear sum of the specular ocean emissivity and the rough ocean emissivity as shown previously in Eq. (2.6).

Existing ocean roughness radiometric models characterize the "excess emissivity" versus surface wind speed up to approximately 20 m/s. Beyond 20 m/s, the ocean emissivity is not well known because of the rarity of radiometric observations of such events.

3.2.1 Near-Nadir Models

The wind friction at the air/sea interface generates short ocean (capillary) waves, which increases the emissivity over that predicted by the Fresnel power reflection coefficient.

One example of a surface emissivity model is Wilheit [2, 3], which uses the Lane and Saxton complex dielectric constant for saline water [11] and Fresnel power reflection coefficient to calculate emissivity as a function of *EIA*. For the wind speed dependence, Wilheit combines the effects due to rough surfaces and foam formation in one term and calculates the surface emissivity, which is divided into three different wind speed regions: $ws \leq 7$ m/s, $7 < ws < 17$ m/s

and $ws \geq 17$ m/s. In these three regions, he models the wind speed as linear, quadratic and then linear dependence for each region, respectively.

$$Emissivity_{Total} = F_n + (1 - F_n)E_{rough} \tag{3.2}$$

where,

F_n is a function of n =1, 2, 3 wind speed regions, and

E_{rough} is the rough water emissivity.

This model has been validated using satellite measurements and ocean buoy wind speed measurements [11].

Another popular surface emissivity model was developed by Stogryn [4], which is also a function of *EIA*. This model treated total emissivity as the sum of two parts as shown in Eq. (3.3).

$$\text{Emissivity}_{\text{total}} = \alpha * \text{foam emissivity} + (1- \alpha)*\text{foam free emissivity} \tag{3.3}$$

where,

α is the percentage of foam coverage.

Stogryn based his model on measurements collected from research journal papers and laboratory experiments of foam coverage at high winds. In Eq. (3.3), it should be noted that the foam has a major contribution on the total emissivity as wind speed increases > 20 m/s.

The NOAA/SFMR emissivity algorithm is an empirical algorithm, which regresses the nadir observations of the airborne SFMR brightness temperature in hurricanes against independent measurements of surface wind speed. Since it is an empirical algorithm, it only has applicability over the narrow frequency range between about 4 – 8 GHz and for nadir *EIA*, but it has been validated over a wide range of wind speeds from 10 m/s to > 70m/s [5]. This algorithm yields the excess emissivity, which is the delta emissivity above a specular surface as a function of frequency and wind speed, given as,

$$Excess_{\ Emis.} = \left(a_2 WS^2 + a_1 WS + a_0\right)\left(1 + b_1 Freq\right) \qquad WS < 33.2\, m/s \qquad (3.4.a)$$

$$Excess_{\ Emis.} = \left(c_1 WS + c_0\right)\left(1 + b_1 Freq\right) \qquad WS > 33.2\, m/s \qquad (3.4.b)$$

where,

WS: wind speed in m/s at 10 m height,

Freq: frequency in GHz,

a_n: wind speed coefficients, where n = 0, 1, 2,

b_1: frequency coefficient, and

c_n: wind speed coefficients, where n = 0, 1.

Figure 3.1 shows the SFMR excess emissivity curves for six frequencies versus wind speed. The excess emissivity increases monotonically with wind speed and also, the emissivity increases weakly with frequency as seen by the spread of curves at high wind speeds. As the wind speed increases, the dispersion in the frequency will be related to foam as it will be discussed later in section 3.2.2.

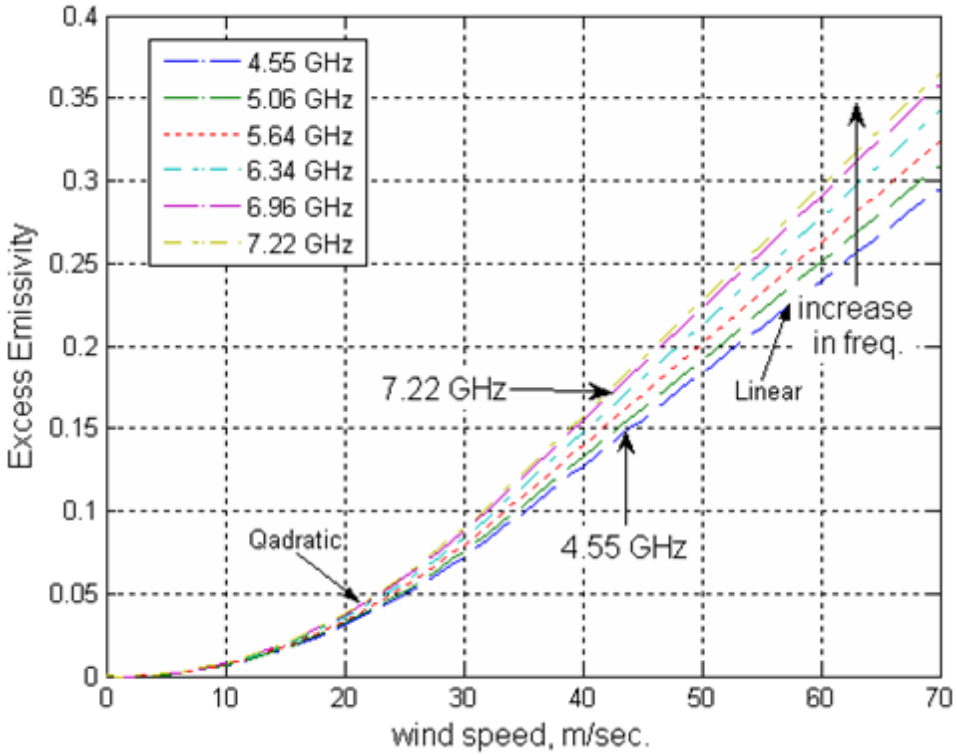

Figure 3.1 SFMR excess emissivity wind model from Uhlhorn et al. [5].

Figure 3.2 shows a comparison between these three emissivity models (at nadir) with respect to wind speed. The SFMR model is considered to be the most trusted and is the standard for comparison because of its thorough validation over a wide dynamic range of wind speeds. All

three perform well for low to moderate wind speeds; however as wind speed increases > 10 m/s, the Wilheit and Stogryn models both have deficiencies as shown in Fig. 3.2. Wilheit has two different relationships for V and H polarizations and they are not equal at nadir for wind speeds greater than approximately 10 m/s, which is physically unrealistic. Also, compared to SFMR, the V-pol over estimates emissivity for wind speeds less than ~35 m/s and under estimates for wind speeds greater than ~ 35 m/s.

On the other hand, Stogryn's model compares even less well with the SFMR. In his model, the emissivity is dominated by the percentage of foam coverage, which reaches a maximum of 100% at approximately 35 m/s. This foam fraction model was developed during the 1980's and contradicts the SFMR performance where wind speeds greater than 70 m/s have been observed with no saturation effects.

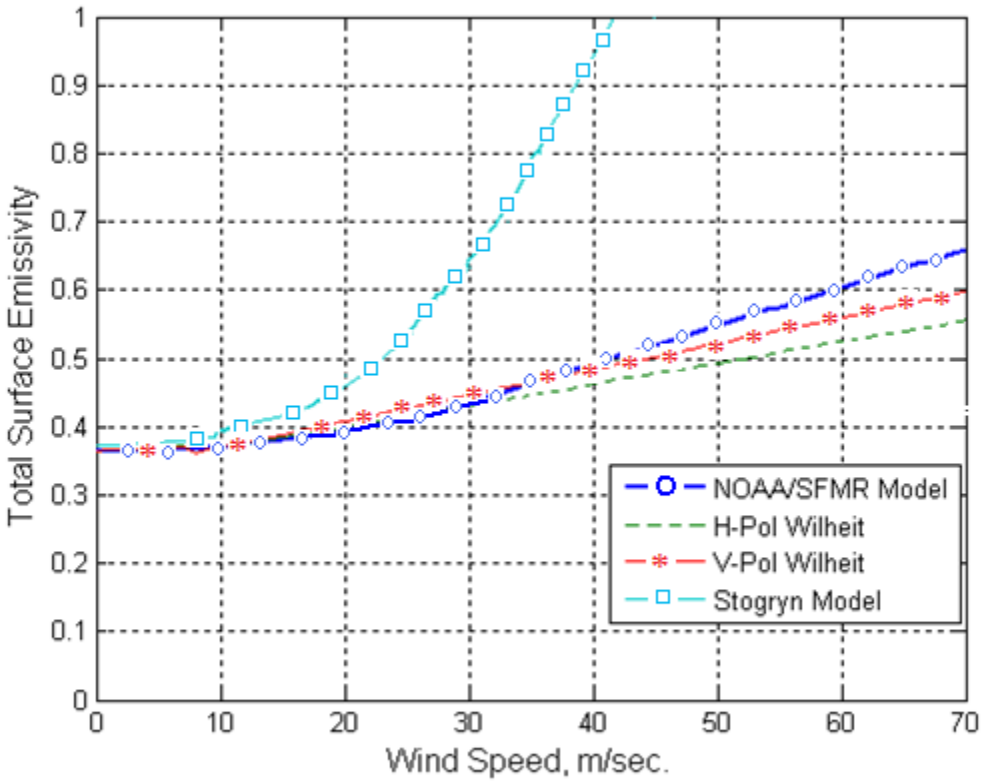

Figure 3.2 Surface emissivity comparison at nadir for SFMR, Wilheit and Stogryn wind speed models.

The previous discussed models had covered the wind speed induced surface emissivity which represents the first part (ε_{ocean}) of Eq. (3.1) at nadir.

3.2.2 Off-Nadir Models

As discussed in Section 3.2.1, the Wilheit and Stogryn emissivity models have an incidence angle dependent term that can be used at incidence angles off-nadir. Also, another well validated surface emissivity model is available from Wentz [1], which is restricted to a limited

range of incidence angles (49 - 57) degrees that are common for conical scanning satellite microwave imagers. This model also combines the effect of foam percentage and other roughness effects in one term as,

$$Emissivity_{total} = \left(1 - F_{pn}\right) R_{geo} \tag{3.5}$$

where,

F_{pn} is a function of wind speed, p = polarization, n =1, 2, 3 wind speed regions, and

R_{geo} is the sea surface reflectivity.

F_{pn} is a function of wind speed that is divided into three different regions depending on wind speed and polarization, and there is a correction term to the vertical polarization Fresnel reflection coefficient in Eq. (2.7) that is a function of sea surface temperature. For V-pol, there are three wind speed dependence regions; linear for $ws < 3$, quadratic for $3 \leq ws \leq 12$, and linear for $ws > 12$. Also, for H-pol there are two linear wind speed dependence regions; one for $ws < 7$, $ws > 12$, and a quadratic wind speed dependence for $7 \leq ws \leq 12$. The Wentz model has been validated using ocean buoys for wind speeds < 20 m/s [24].

Figure 3.3 shows the three different models for specular surface emissivity (zero wind speed) for 6.93 GHz that exhibit small but significant differences. Even though the differences are small, of the order of 0.01, this corresponds to a difference in brightness temperature of 3

Kelvin (assuming 300° Kelvin sea surface temperature), which is considered to be large for model differences.

Since these models all use Fresnel power reflection calculation, these differences are due to the dielectric constant models assumed. Wentz has developed his own complex dielectric constant model [12] based on measurements from SSMI satellites and published empirical dielectric data for sea water. Wilheit used the model of Lane and Saxton [11] which has been improved by Stogryn [10] and Klien and Swift [9]. Stogryn based his complex dielectric constant model in part using studies taken by Lane and Saxton [11].

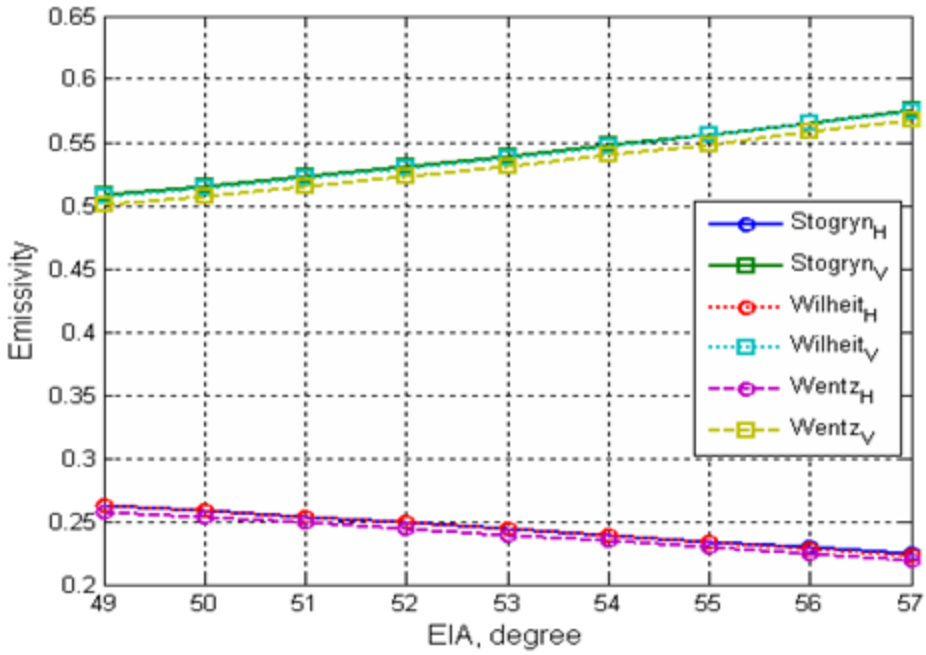

Figure 3.3 Stogryn, Wilheit and Wentz specular ocean emissivity model comparisons for a wind speed of zero m/s and Freq = 6.93GHz.

Figure 3.4 shows the rough emissivity models of the three modelers (Wilheit, Stogryn and Wentz) for 6.93 GHz and wind speed of 10 m/s. Again there are significant differences between models.

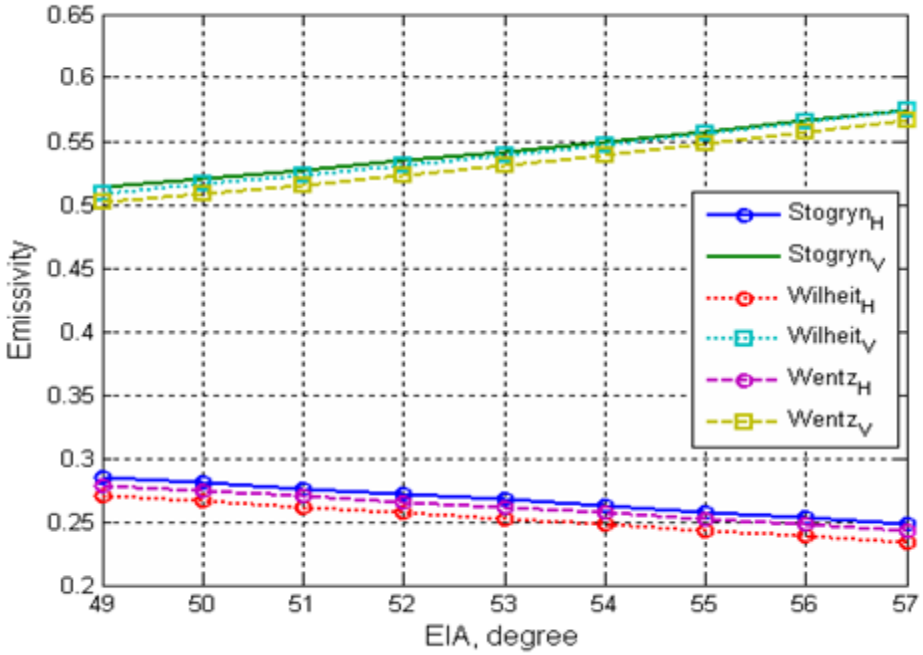

Figure 3.4 Stogryn, Wilheit and Wentz wind speed model comparison for a wind speed of 10 m/s and Freq = 6.93GHz.

Of the three, we consider Wentz to have the best surface emissivity model for higher incidence angles because it has been validated against ocean buoys using over a decade of multiple SSMI satellite measurements, and it performs well with other geophysical retrievals.

3.3 CFRSL Ocean Emissivity Model

Modeling the surface emissivity in the presence of high wind speeds is difficult, and the formation of the high emissivity of foam and its indirect relationship to wind speed complicates the model. Some researchers combine the effect of foam and other roughness effects, like the Wilheit and Wentz models discussed above; but others prefer to separate it, like Stogryn.

The CFRSL ocean emissivity model has been developed based upon a collection of published ocean emissivity data sets, which came from measurements of ocean surface emissivity using a variety of radiometer systems, operating over a wide range of frequencies and incidence angles and from different platforms such as satellites, aircraft, experimental field observations using tower based radiometers, and laboratory measurements. The CFRSL model adopted a physically based model with empirical coefficients tuned to fit these empirical data sets. Table 3.1 shows a summary of the data sets used in the modeling.

Table 3.1 Data sets used in the CFRSL Ocean Emissivity Model

	Field/Laboratory Experiments			Radiometer Observations		
		Freq, GHz	EIA, deg		Freq, GHz	EIA, deg
Foam	Foam, Fain, Oil Slicks and GPS Reflectrometry (FROG), [20]	L-Band	Nadir ~ 90	Jason Microwave Radiometer (JMR)	18.7, 23.8, 34	Nadir
	Wave tank experiments, [18]	10.8, 18.7, 37	53	Stepped Frequency Microwave Radiometer (SFMR)	C-Band (4-7)	Nadir ~ 35
	Chesapeake Bay field experiments, [36]	10.8 & 36.5	30 – 60			
	Other, [19]					
Ocean - foam free	Alex Stogryn [4] Hollinger [13] Other [25]			Special Sensor Microwave/Imager (SSM/I)		
				Stepped Frequency Microwave Radiometer (SFMR)		
				Topex poseidon Microwave Radiometer (TMR)	18, 21, 37	Nadir
Wind Direction				Topex poseidon Microwave Radiometer (TMR)	18, 21, 37	Nadir
				WindSat	10.7, 18.7, 37	53
				Aircraft S-band measurements in Pacific ocean and Barents sea	S-band	Nadir
				Wentz Observations for five collected data sets – SSM/I, TMI, QUIKSCAT, BOUYS, REYNOLDS	11, 19, 37	53

The main emphasis for the development of the CFRSL ocean emissivity model is the desire for a unified analytical model that may be used as a subroutine for ocean radiative transfer models. Our model characterizes the emissivity and power reflection coefficient of the sea surface for a wide range of frequencies, incidence angles, and large dynamic range of wind speed and all wind directions. Thus, the CFRSL ocean emissivity model removes these shortcomings presented by other models and provides the basis for an improved "general purpose" microwave radiative transfer model. The derivation of this CFRSL model is discussed in this section. The goal is to provide an emissivity model that matches current emissivity models in their region of applicability and smoothly extrapolates their capabilities for other regimes.

The CFRSL model is constrained to be monotonic with frequency, *EIA* and wind speed and the first derivative with respect to the parameter does not change sign (i.e. no slope inflections). The CFRSL emissivity model presented below follows the formulation of Stogryn and accounts for the effects of foam on a physical basis. We choose to model the individual terms as follows,

$$\varepsilon = T_{sur} / SST \tag{3.6}$$

where *SST* is sea surface temperature (Kelvin). It follows that,

$$\varepsilon_{ocean} = FF \times f(freq) \times f(EIA, ws) + (1 - FF) \times \left(\varepsilon_{smooth} + \varepsilon_{rough}\right) \tag{3.7}$$

where,

ε_{ocean} is total ocean surface emissivity,

f(freq) is the frequency dependent emissivity of foam,

f (EIA,ws) is the earth incidence angle (*EIA*), and wind speed dependence of foam, and

ε_{rough} is the rough sea surface emissivity, which has the form

$$\varepsilon_{rough} = \frac{g(EIA,ws,freq)}{SST} \tag{3.8}$$

The term *f (EIA,ws)* will have a different form and will be discussed later in this dissertation. The modeling of the CFRSL was performed iteratively by estimating all model coefficients simultaneously as will be discussed in the next section.

3.3.1 CFRSL C-Band Wind Speed Modeling

The CFRSL ocean emissivity model for C-band (4 – 8 GHz) relies predominantly on three sources of data: (1) the NOAA SFMR algorithm [5], (2) actual SFMR T_b measurements in hurricanes at high bank angles and (3) WindSat hurricane observations [37]. The detailed derivation is discussed in the following sections.

3.3.1.1 Near Nadir Low Wind Speed Modeling

For the rough emissivity part (ε_{rough}) a model similar to Stogryn was adapted in which ε_{rough} is a function of wind speed, earth incidence angle, frequency, and sea surface temperature. A collection of SFMR aircraft low to moderate wind speed (5 – 20 m/s) measurements had been collected from different SFMR flights, these data were used to tune the coefficients of the rough emissivity part. As mentioned earlier, the process was iterative, it started with Stogryn coefficients as an initial guess and then the coefficients were changed iteratively to minimize the weighted difference between SFMR T_b observations at nadir, Stogryn and Wilheit models and the CFRSL model. Later, off-nadir SFMR T_b observations and other emissivity data were used to estimate the *EIA* dependent coefficients and to iteratively "fine tune" the nadir-derived coefficients. Therefore, the final formation of the rough emissivity will be provided later in this chapter when we discuss off-nadir modeling and SFMR brightness temperature treatments.

3.3.1.2 Foam Fraction and Emissivity

At hurricane force wind speeds, foam emission is the dominant component of the ocean brightness temperature. As discussed in section 2.3, sea foam is produced when ocean gravity waves break, which occurs at wind speeds > 6-7 m/s, and the fractional area foam-coverage increases almost exponentially with wind speed. At nadir, the CFRSL model coefficients for foam emissivity and foam fraction were derived using an iterative procedure to maximize agreement with the NOAA SFMR ocean emissivity model (Eq. 3.4). We justify using the NOAA SFMR excess emissivity as "truth" because this algorithm has demonstrated excellent wind

speed retrieval accuracy as compared with independent wind measurements from global positioning system (GPS) dropwindsondes over the range of 10 m/s to > 70 m/s [5]. It follows that the correct characterization of emissivity versus wind speed is a necessary condition to achieve accurate wind speed retrievals.

Based on experimental evidence [16] it is recognized that the emissivity of foam varies with frequency and incidence angle but not with wind speed; and it ranges between 0.85 – 0.90 in emissivity, which is considerably higher than the emissivity of sea water. To solve Eq. (3.7) for ε_{foam_freq} ; first, the emissivity of foam is assumed to be only a function of frequency, *f(freq)*, so the *f(ws,EIA=0)* term in Eq. (3.7) was set equal to unity for all wind speeds. From the NOAA SFMR model, the total ocean emissivity at 70 m/s was determined and the foam-free (ε_{rough}) contribution was subtracted according to Eq. (3.9).

$$f(freq) = \frac{\varepsilon_{SFMR} - (1-ff)\varepsilon_{rough}}{ff * f(EIA,WS)} \tag{3.9}$$

This yields the foam emissivity, taking the derivative with respect to frequency yielded the estimate of *f(freq)*. It should be noted that according to Eq. (3.7) there is also a frequency dependence of the foam-free ε_{rough} that is small. Using a least-squares regression of the foam emissivity at the six SFMR frequencies yields,

$$f(freq) = 0.036659 * \text{freq} + 0.57767 \tag{3.10}$$

where *freq* has units of GHz.

Next, the dependence of foam fraction on wind speed was derived using the Uhlhorn emissivity model over the dynamic range of zero to 70 m/s. In this calculation, Stogryn's ε_{rough} was used; however, since the function ε_{rough} in Eq. (3.7) was allowed to change, the *FF* was also calculated iteratively as shown in Eq. (3.11).

$$FF = \frac{\left\langle \varepsilon_{SFMR} \right\rangle_{freq} - \left\langle \varepsilon_{rough} \right\rangle_{freq}}{\left\langle \varepsilon_{foam} \right\rangle_{freq} - \left\langle \varepsilon_{rough} \right\rangle_{freq}} \tag{3.11}$$

where, $< >_{freq}$ is denoted for the average over all SFMR frequencies.

By examining the data, we modeled foam fraction as rational Chebychive function of wind speeds, which yields minimum residuals and asymptotically approach a 100% for wind speeds > 100 m/s as shown in Eq. (3.12),

$$FF = \frac{\sum_{i=0}^{6} a_i ws^i}{b_o + \sum_{j=1}^{8} b_j * ws^{j-1}} \tag{3.12}$$

where,

ws is the ocean surface wind speed measured at 10 m height above the surface,

FF is foam fraction,

a_i are coefficients that are shown in Table 3.2 below , i= 0-6, and

b_j are coefficients that are shown in Table 3.2 below , j= 0-8.

Table 3.2 Foam fraction wind speed coefficients values for WS > 6 m/s

Coefficient	Value	Coefficient	Value
Coef	Value	Coef.	Value
a_0	7.9142×10^{-5}	b_0	1.0
a_1	-12.0190×10^{-5}	b_1	-12040.3641×10^{-5}
a_2	3.9988×10^{-5}	b_2	703.1839×10^{-5}
a_3	-6.1957×10^{-6}	b_3	-19.2999×10^{-5}
a_4	4.2190×10^{-7}	b_4	3.0128×10^{-6}
a_5	-7.7814×10^{-9}	b_5	-2.7323×10^{-8}
a_6	4.4360×10^{-11}	b_6	1.2071×10^{-10}
N/A	N/A	b_7	-1.2096×10^{-13}

For wind speed < 6 m/s. *FF* is set equal to zero.

A Comparison of this FF with current foam fraction measurements will be shown in Chapter 4 of this dissertation.

3.3.1.3 Off-Nadir High Wind Speed Modeling

To support the estimation of foam emissivity, *f(EIA,ws)*, a collection of off-nadir SFMR T_b data obtained during NOAA aircraft high-banked turns were assembled and sorted according to wind speed and radial distance from the eye of the hurricane as shown in Table 3.3. First, these data were quality controlled (QC) edited [38] to remove the effect of rainy pixels and other T_b errors e.g., radio frequency interference (RFI), land contamination, etc. Next, atmospheric

corrections for *WV*, *CLW*, O_2 and *Rain* were applied to estimate the surface emission alone, a detailed explanation will be provided below for each of these QC's.

Table 3.3 Hurricanes data used in CFRSL Model Development

Hurricane	Year	max 1-min sustained wind speed	Number of flights
Fabian	2003	120 kt (60 m/s)	3
Frances	2004	115 kt (58 m/s)	6
Katrina	2005	150 kt (75 m/s)	4
Ophelia	2005	65 kt (34 m/s)	4
Rita	2005	155 kt (78 m/s)	5

3.3.1.3.1 Radio Frequency Interference (RFI) Treatment

The tedious process of sorting and clearing the SFMR measurements from all sources of errors started by removing the radio frequency interference (RFI) noise from the measurements. The process was straight forward and was implemented by calculating the T_b difference between adjacent pairs of the 6 SFMR frequencies and removing any value that exceeded a selected threshold (based on consideration that brightness temperature increases with frequency). It is worth noting that (on average) RFI contaminated approximately 18% of SFMR measurements and on some other flights reached 28%. This RFI noise has been frequently observed on the NOAA P-3 aircraft because the SFMR is mounted in relatively close proximity to on-board C-band radars. An example of an RFI contaminated SFMR measurement is shown in Fig. 3.5, for

contaminated and cleared data, respectively. Care was taken to remove RFI but to leave the dispersive T_b measurements in rain (identified on the figure).

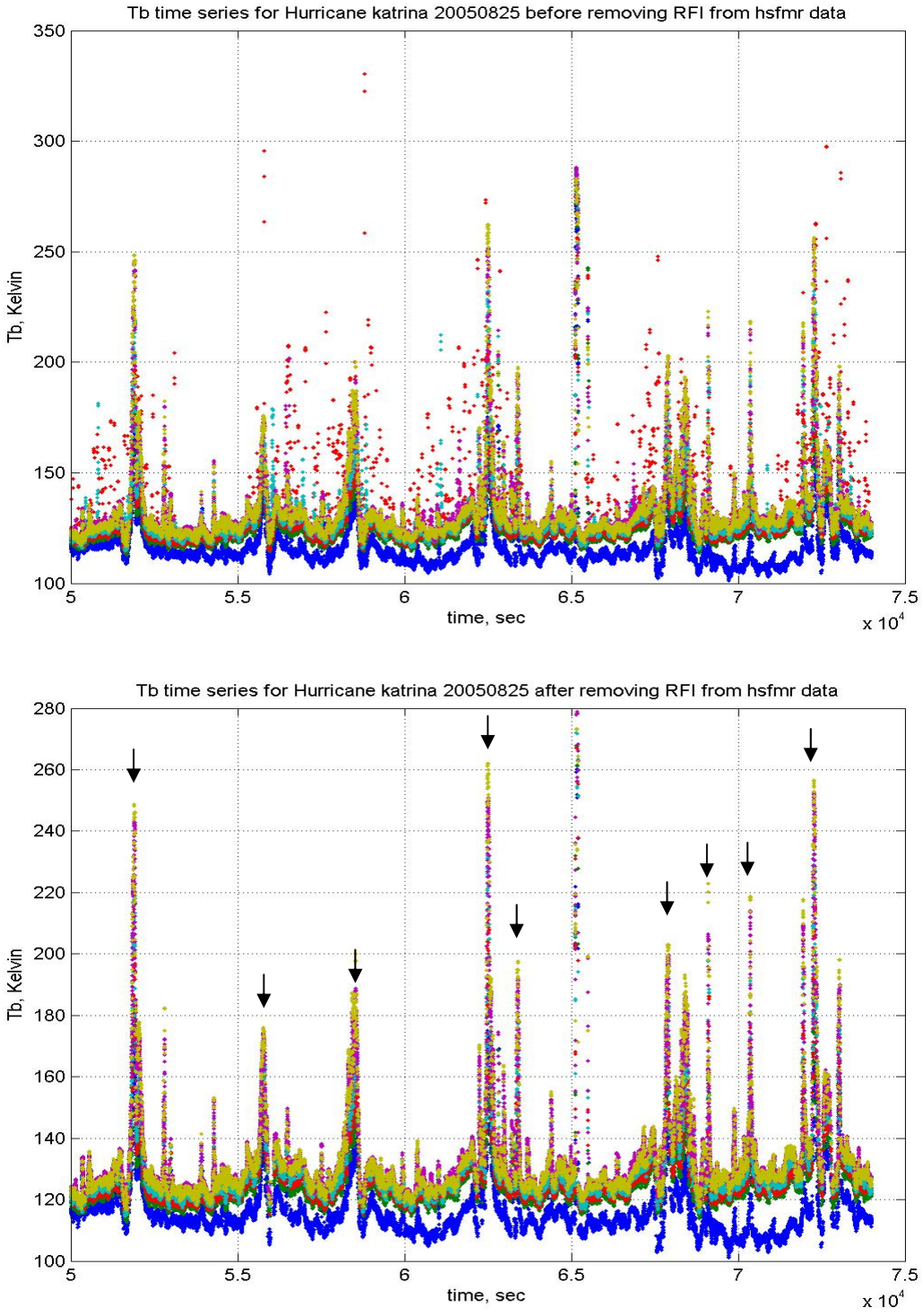

Figure 3.5 SFMR data record (a) data with RFI (b) data after RFI clearing, where "↓" denotes heavy rain bands.

3.3.1.3.2 Data Record Cross-Correlation

SFMR measurements during aircraft turns have been sorted from multiple flight records. During data reduction, it was observed that there is a time-shift between the recorded aircraft bank angle and the measured brightness temperature [38]. Since these data (T_b and roll angle) were recorded in two different asynchronous data streams, an algorithm was developed to cross-correlate these time series and thereby align the two data records. An example of shifted brightness temperature versus roll angle is shown in Fig. 3.6 for both vertical and horizontal polarizations, respectively.

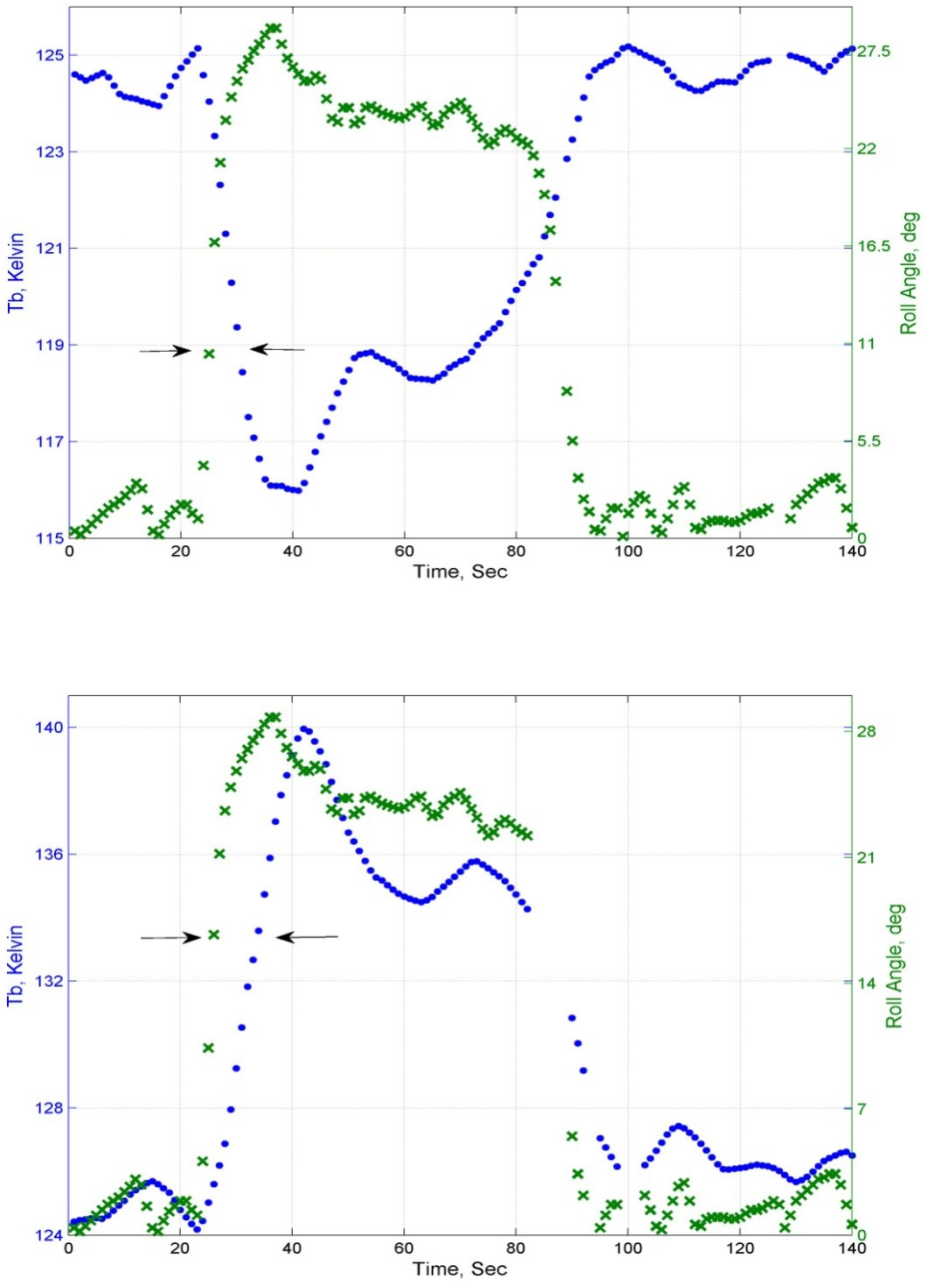

Figure 3.6 Example of SFMR brightness temperature during an aircraft turn for horizontal (Upper panel) and vertical (lower panel).

3.3.1.3.3 Antenna Pattern Bias Removal

The SFMR horn antenna has a half-power beamwidth of ~ 16° for all the six frequencies, which affects the T_b's for both nadir and off-nadir measurements. To correct this measurement distortion, an antenna pattern bias removal procedure was applied in which the SFMR antenna pattern was modeled as a Gaussian function as shown in Fig. 3.7. This wide beam leads to averaging T_b's from nearby incidence angles as shown in Fig. 3.8, in which the reflected and surface emissions will be weighted and summed by the antenna power-gain pattern.

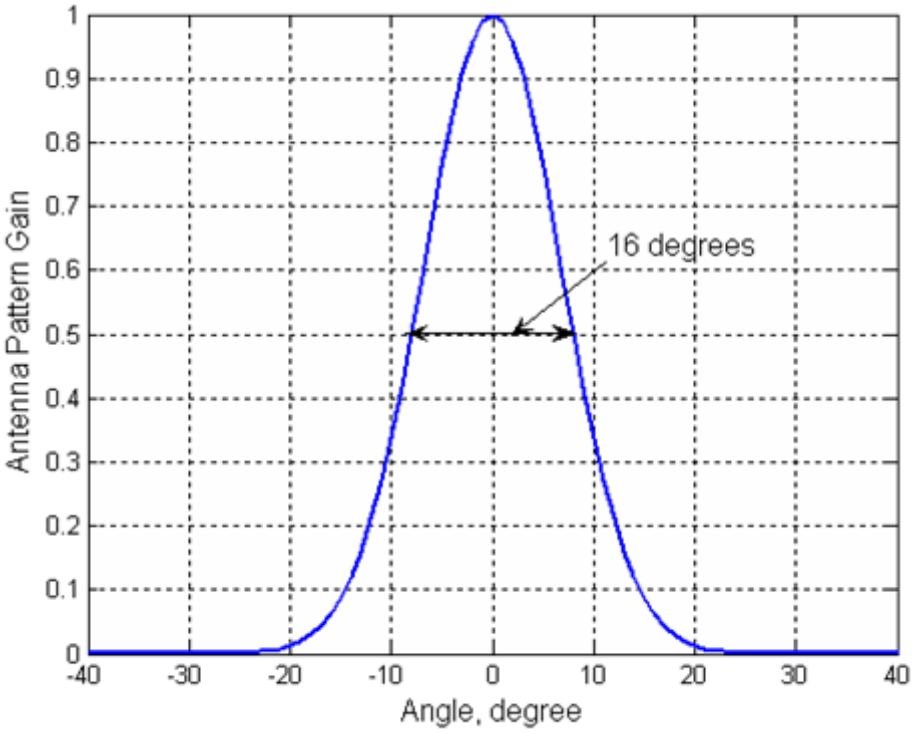

Figure 3.7 SFMR normalized gain antenna pattern approximation.

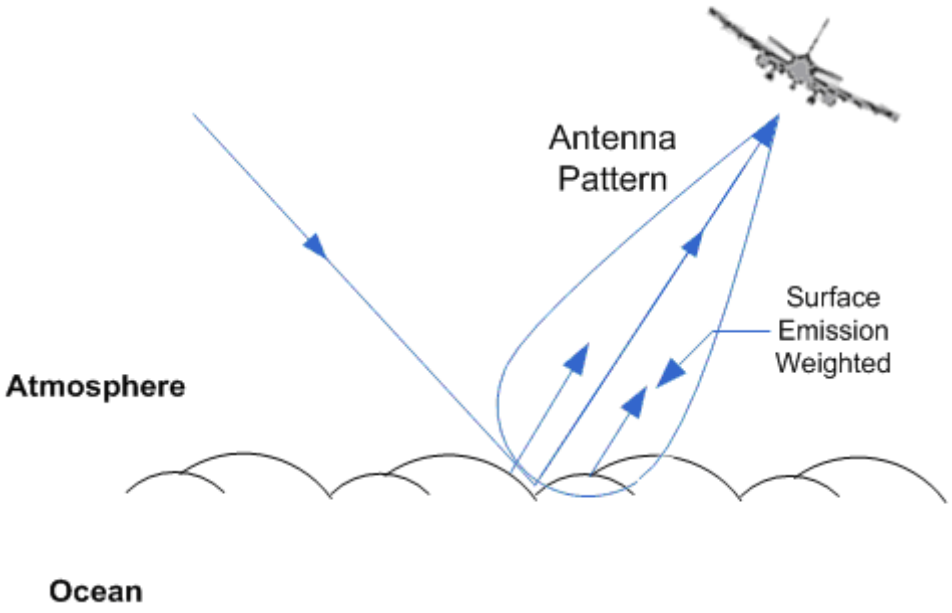

Figure 3.8 SFMR antenna viewing ocean surface.

On the NOAA aircraft, there are two types of SFMR antennas, one that is mounted on the bottom of the aircraft fuselage and the other under the aircraft in a wing pod for nadir viewing along the ground track as shown in Fig. 3.9.

Figure 3.9 AOC SFMR instrument electronics.

The antennas are mounted with either perpendicular (horizontal) polarization in the plane of incidence or with parallel (vertical) polarization in the plane of incidence. The plane of incidence is defined as the plane that contains the antenna line-of-sight and the normal to the sea surface, as shown in Fig. 3.10. As the aircraft enters into a bank and the SFMR antenna line-of-sight points off-nadir, the polarization becomes parallel (vertical for the nadir viewing perpendicular mounted SFMR) and perpendicular (horizontal for the nadir viewing parallel mounted SFMR) to the plane of incidence. The result is that the brightness temperature will increase with incidence (roll) angle (*EIA*) for V-pol, and decrease for H-pol, as shown previously in Fig. 3.6.

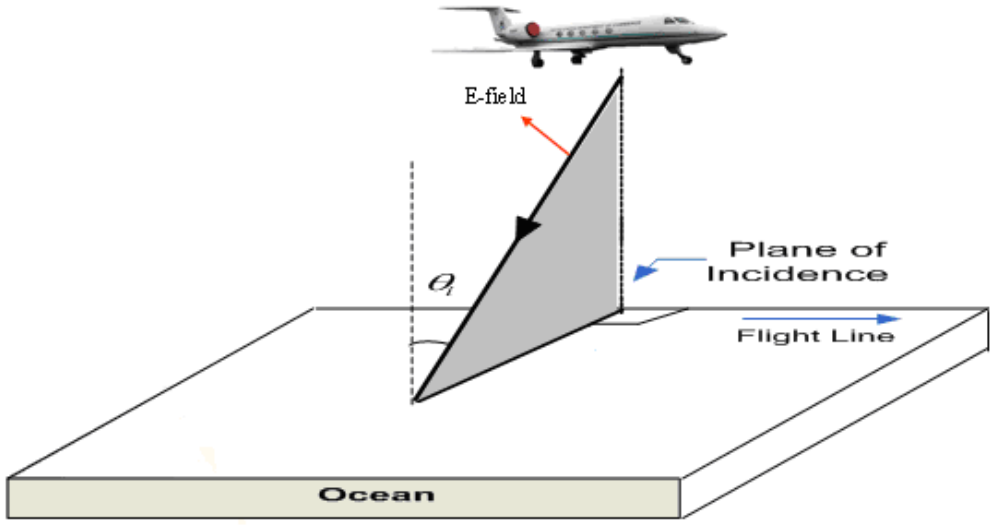

Figure 3.10 Plane of incidence for off-nadir T_b measurements.

For nadir looking horizontally polarization mounted SFMR, the effect of antenna pattern averaging combines both the horizontal and vertical surface emission equally. Above 20° incidence angle only T_b contribution from the V-pol will be averaged; and in between, there will be a variable ratio (with *EIA*) between the H- and V-polarizations. To develop the T_b antenna pattern bias removal, we calculate a sliding weighted average (convolution) of the antenna gain pattern with the surface smooth emissivity versus EIA, which is illustrated in Fig. 3.11 and Fig. 3.12.

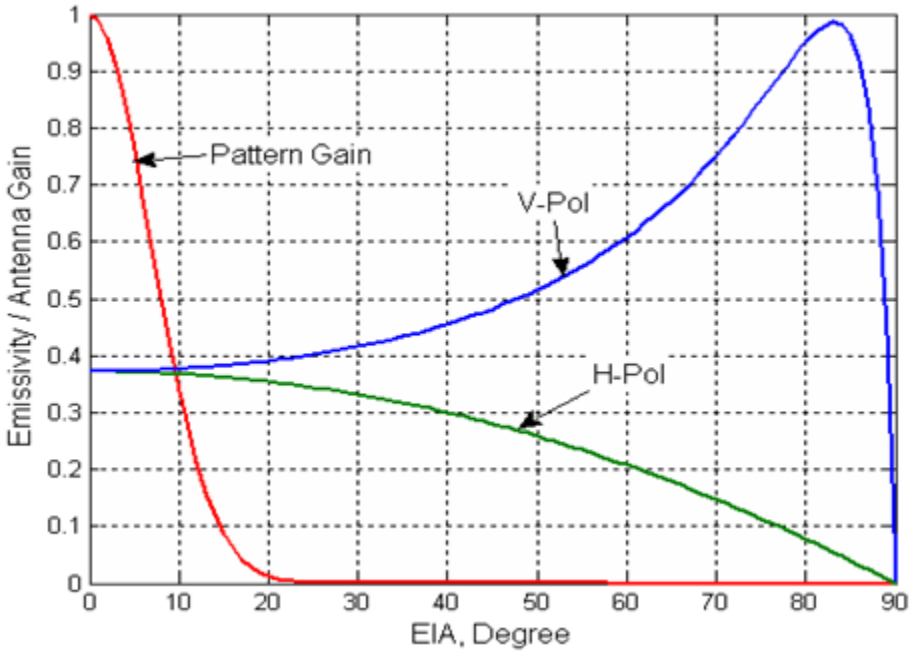

Figure 3.11 Antenna pattern weighting of surface emissivity at nadir.

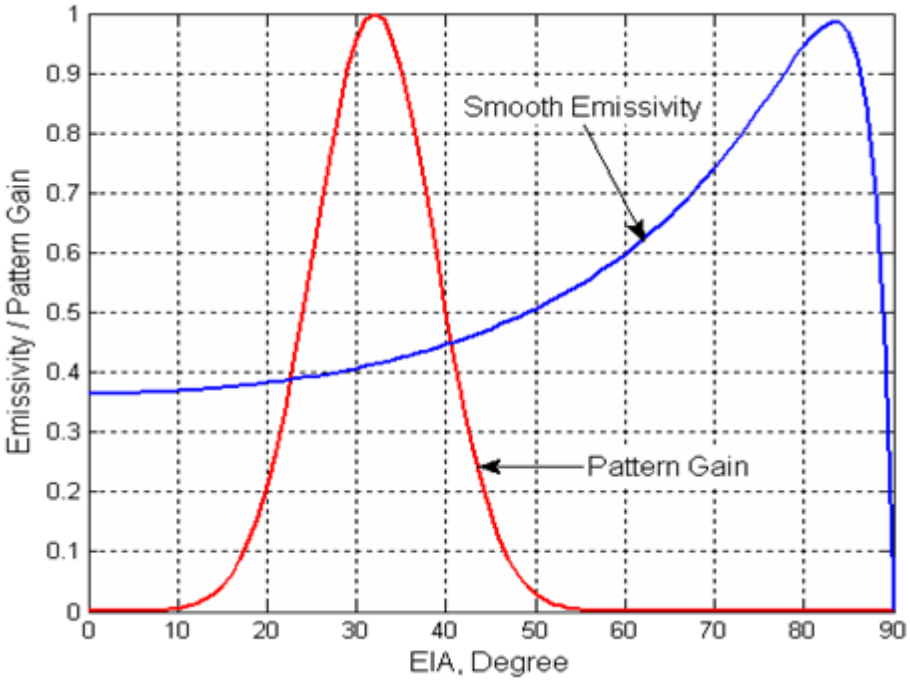

Figure 3.12 Antenna pattern weighting of V-pol surface emissivity off-nadir.

The simulated SFMR measured emissivity is a 4th order polynomial (red curve) shown in Fig 3.13, which depends on *EIA* and frequency. The antenna pattern averaging is an additive term to the smooth emissivity (blue curve) from the CFRSL surface emissivity model; and the antenna pattern correction ($\Delta\varepsilon_{pat}$) is the difference between the simulated measured (red) and modeled (blue) curves versus *EIA*.

$$\Delta\varepsilon_{pat} = a_4 EIA^4 + a_3 EIA^3 + a_2 EIA^2 + a_1 EIA + a_0 \tag{3.13}$$

where,

a_n are the coefficients listed in Table 3.4, and

EIA is the earth incidence angle in degrees.

Table 3.4 Antenna pattern correction coefficients for V-Pol

Coefficients / Frequency	$\mathbf{a_0}$	$\mathbf{a_1}$	$\mathbf{a_2}$	$\mathbf{a_3}$	$\mathbf{a_4}$
4.55	1.20×10^{-8}	-4.57×10^{-7}	5.08×10^{-5}	9.07×10^{-5}	0.364711
5.06	1.19×10^{-8}	-4.49×10^{-7}	5.07×10^{-5}	9.38×10^{-5}	0.366709
5.64	1.18×10^{-8}	-4.42×10^{-7}	5.06×10^{-5}	9.68×10^{-5}	0.368564
6.34	1.17×10^{-8}	-4.33×10^{-7}	5.05×10^{-5}	1.00×10^{-4}	0.370435
6.96	1.16×10^{-8}	-4.26×10^{-7}	5.04×10^{-5}	0.000103	0.371887
7.22	1.16×10^{-8}	-4.23×10^{-7}	5.04×10^{-5}	0.000104	0.372458

$$\varepsilon_{measured} = \varepsilon_{smooth} + \Delta\varepsilon_{pat} \tag{3.14}$$

where,

ε_{smooth} is the smooth surface emissivity computed using Eq. (2.5).

Figure 3.13, shows the antenna pattern correction applied to the specular emissivity with respect to *EIA* for the 4.55 GHz vertical polarization. The antenna pattern correction at 45 degree *EIA* is ~2 Kelvin, and this value varies along the *EIA* region (0° – 45°) by about (0.6 - 2) Kelvin difference.

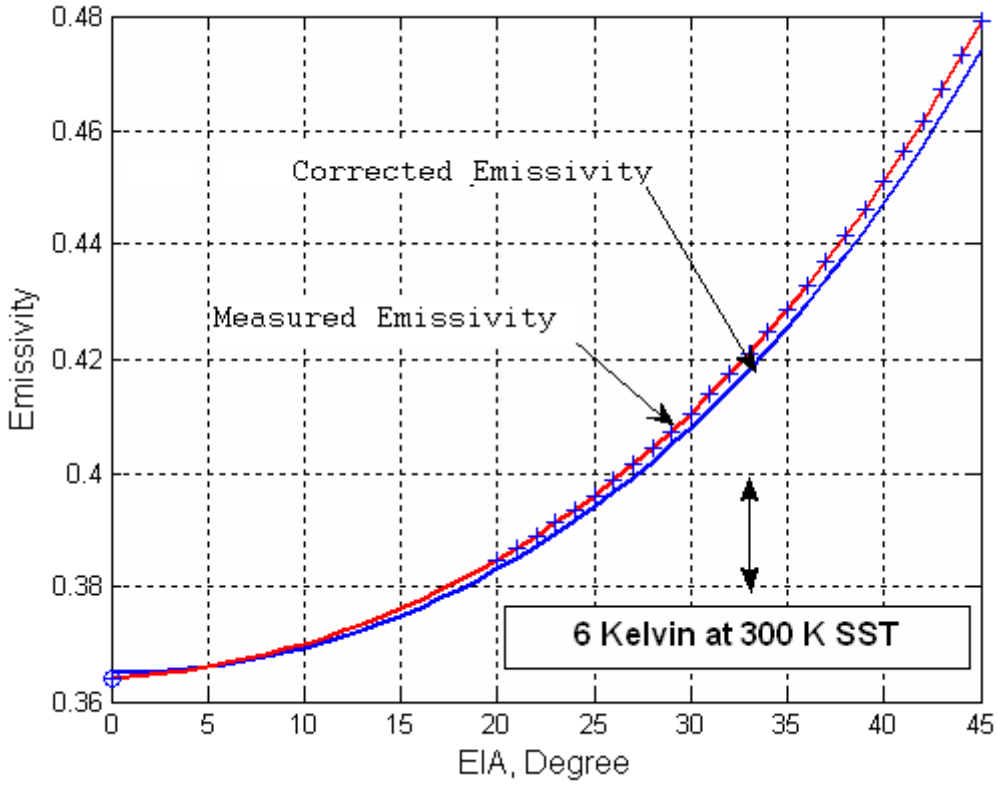

Figure 3.13 V-Pol surface emissivity before and after antenna pattern correction.

The same procedure was also applied for the nadir looking vertically polarization mounted SFMR, and the coefficients are shown in Table 3.5.

Table 3.5 Antenna pattern correction coefficients for H-Pol

Coefficients / Frequency	a_0	a_1	a_2	a_3	a_4
4.74	6.05×10^{-9}	-8.59×10^{-7}	-2.25×10^{-6}	-8.59×10^{-4}	0.364927
5.31	4.87×10^{-9}	-7.11×10^{-7}	-9.19×10^{-6}	-7.27×10^{-4}	0.36695
5.57	3.98×10^{-9}	-5.96×10^{-7}	-1.46×10^{-5}	-6.19×10^{-4}	0.367743
6.02	3.18×10^{-9}	-4.89×10^{-7}	-2.00×10^{-5}	-5.11×10^{-4}	0.369003
6.69	2.60×10^{-9}	-4.09×10^{-7}	-2.41×10^{-5}	-0.00043	0.370668
7.09	2.07×10^{-9}	-3.32×10^{-7}	-2.81×10^{-5}	-0.00034	0.371586

3.3.1.3.4 Atmospheric Correction

To solve for the incidence angle dependence of foam emissivity *f(EIA,ws)* in Eq. (3.7), we extracted the measurements taken during the aircraft banks and then binned them into different wind speeds and *EIA* regions and finally applied the antenna pattern bias removal to the binned SFMR measurements. This process removed the unwanted bias from the measured brightness temperature.

The next step involved "atmospheric clearing" to remove the atmospheric component of SFMR T_b before estimation of the ocean surface emissivity. For this purpose, radiative transfer calculations were performed using a typical hurricane atmosphere by Frank [39]. Further, the effect of rain was removed using the approach of Uhlhorn et. al. [40]. Datasets were carefully selected to minimize regions with heavy rain, but typically rain atmospheric clearing was required. This involved estimating the rain rate along the propagation path using SFMR rain retrievals during level flight before and after the turns. For atmospheric clearing, the rain was assumed to be homogeneous with a 100% antenna beam-fill. This is considered to be valid because the SFMR operated at low altitudes (< 2.5 km) and at low bank angles (< 35°), which

resulted in the line-of-sight being displaced by < 1.75 km from nadir. Atmospheric clearing typically yielded T_b adjustments of < 5 K [38].

After correcting the measured SFMR brightness temperature for atmospheric effects, this resulted in brightness temperature values referenced to the surface. The data were then binned based on wind speed (5 m/s) and *EIA* (2 degrees). This process covered the measurement of C-band emissivity over wind speed for an *EIA* range up to 35 degrees.

3.3.1.3.5 Satellite C-Band Observations

For wind speeds < 20 m/s and high *EIA* (49° - 57°), the surface emissivity model by Wentz [1] was used to estimate the total ocean emissivity versus wind speed. Wentz results were based upon over one decade of Special Sensor Microwave/Imager (SSM/I) T_b comparisons with in-situ wind speed measurements on buoys. The buoy dataset only extended to ~ 20 m/s; so hurricane observations from the WindSat polarimetric radiometer were used for higher wind speeds.

An analysis of WindSat C-band (6.8 GHz) V- and H-pol T_b in hurricanes by Ruf [37] was used to estimate the total ocean emissivity at high wind speeds and *EIA*'s (49° - 55°). This study involved satellite radiometer measurements obtained during 2005 hurricanes (Dennis, Rita and Katrina) and associated high quality surface wind fields derived from NOAA HRD aircraft underflights with SFMR. Results showed a well-behaved and monotonic increase in the C-band ocean emissivity with surface wind speed provided using NOAA's H*Wind analysis procedure (see Table (1) and Fig. 5 in [37]). These data were extrapolated to HIRAD's C-band frequencies

(4 - 7) GHz and then were used as points of reference at higher *EIA* (> 45 °) in a weighted least-mean-squares sense to derive the foam emissivity dependence *f(EIA,ws)* in Eq. (3.7).

The resulting *f(EIA,ws)* and *g(EIA,ws,freq)*, from this analysis are modeled using Eq. (3.15) and (3.16) for both V-pol and H-pol, along with their coefficients in Table 3.6 and Table 3.7 , respectively.

$$Z_1 = \frac{1}{1 + e^{\frac{-(x-a)}{-b}}}$$

$$Z_2 = \frac{1}{1 + e^{\frac{-(y-c)}{-d}}}$$

$$f(EIA,\ ws)_{H-pol} = e + f \times Z_1 - g \times Z_2 + h \times Z_1 \times Z_2 \qquad (3.15.a)$$

$$Z_1 = \frac{1}{1 + \left(\frac{x-a}{b}\right)^2}$$

$$Z_2 = \frac{1}{1 + \left(\frac{y-c}{d}\right)^2}$$

$$f(EIA,\ ws)_{V-pol} = e + f \times Z_1 - g \times Z_2 + h \times Z_1 \times Z_2 \qquad (3.15.b)$$

Table 3.6 *f(EIA,ws)* coefficients for both vertical and horizontal polarization

	a	**b**	**c**	**d**	**e**	**f**	**g**	**h**
H-pol	49.977	13.394	16.404	6.178	0.539	0.471	1.754	1.891
V-pol	123.603	50.676	27.180	0.00197	0.9688	0.2633	0.1311	0.3894

$$g(EIA, ws, freq)_{H-pol} = Cheby\_Bivar\_Pol10(ws, EIA)\sqrt{freq} \quad (3.16.a)$$

$$g(EIA, ws, freq)_{V-pol} = ws * (0.117 - 2.09\ 10^{-3} \sum_{i=0}^{5} a_i * EIA^i)\sqrt{freq} \quad (3.16.b)$$

where,

Cheby_Bivar_Pol10(ws,EIA) is the Chebyshev *ws*, *EIA* Bivariate Polynomial of the Order 10. The detailed equation and its coefficients are available in Appendix A. Comparisons with real time data are provided in Chapter 4.

Table 3.7 *g(EIA,ws,freq)* coefficients for vertical polarization

	a_0	a_1	a_2	a_3	a_4	a_5
V-pol	123.603	50.676	27.180	0.00197	0.9688	0.2633

3.3.2 Emissivity model Frequency Dependence

As discussed earlier, most of the CFRSL emissivity model development was based on C-band SFMR data. To be able to use this model for higher and lower frequencies, we required other reputable sources of ocean emissivity measurements at different frequencies.

The physical formation of the model, meaning separating the foam effect of emissivity from the rough emissivity makes it easier for frequency extrapolation. Since *FF* is dependent on wind speed only, it is valid to be used at different frequency ranges, what remains from Eq. (3.7) are the foam emissivity and the foam roughness parts.

3.3.2.1 Foam Emissivity Frequency Dependence

Fortunately, there were several sources of foam emissivity data at different frequencies for nadir and off-nadir pointing radiometers. For example, Camps et. al. [20] conducted research on modeling foam emissivity at L-Band. In his results, he developed a physical functional form for foam emissivity and its dependence on several parameters like bubble size distribution, wind speed, sea surface temperature, polarization, and earth incidence angle. Villarino [41] has also showed similar results to Camps for the emissivity of foam at nadir and L-Band. As for nadir foam emissivities at higher frequencies, Yang [42] and Zhou [43] have published foam emissivity measurements at different frequencies (18.7, 23.8, and 37 GHz). For off-nadir foam emissivities at higher frequencies Rose et. al. [18], Zheng et. al. [44], and Padmanabhan et. al. [19] have all shown foam emissivity measurements at different frequencies between (10.8 – 36.5 GHz) and for a wide range of incidence angles between 20 - 60 degrees for both vertical and horizontal polarizations.

Results from these researchers were combined with the foam emissivity model extracted from SFMR measurements at C-band to derive the foam emissivity frequency dependence over a wide range of frequencies. Further, we have extrapolated these results to asymptotically approach unity at frequencies higher than 180 GHz.

It is worth mentioning that the emissivity of foam for higher and lower frequencies was not dependent on wind speed as it was for C-Band, and this has to do with the relationship between the thickness of foam and frequency. Researchers like Reul [21], and Zhou [43], have shown that the relationship between foam thickness (due to increasing wind speed) and frequency (EM wavelength) is not sensitive and saturates after foam reaches a thickness of ~2 cm. The final

formation of the foam emissivity for frequencies < 2 GHz are provided in Camps et. al. [20] for both horizontal and vertical polarizations while for frequencies > 7 GHz, refer to Eq. (3.17) for both vertical and horizontal polarizations along with the H-pol coefficients shown in Table 3.8.

$$f(EIA,\ freq)_{H-pol} = a + b \times EIA + c \times EIA^2 + \frac{d}{freq} + \frac{e}{freq^2} + \frac{f}{freq^3} + \frac{g}{freq^4} \quad (3.17.a)$$

$$f(EIA, freq)_{V-pol} = Cheby\_Bivar_{Pol10(freq,EIA)} \quad (3.17.b)$$

where,

Cheby_Bivar$_{Pol10}$(freq,EIA) is the Chebyshev *freq*, *EIA* Bivariate Polynomial of the Order 10. The detailed equation and its coefficients are available in Appendix B. Comparisons with real time data are provided in chapter 4.

Table 3.8 *f(EIA,freq)* coefficients for horizontal polarization

	a	**b**	**c**	**d**	**e**	**f**	**g**
H-pol	0.971	-0.00035	-3.746	0.5711	-14.455	39.648	-31.246

3.3.2.2 Rough Ocean Emissivity Frequency Dependence

After deriving the foam emissivity relationship to frequency, wind speed, polarization, and *EIA*, it was possible to solve for the unknown rough emissivity *g(EIA,ws,freq)* in Eq. (3.8).

A collection of emissivity measurements for wind speeds < 20 m/s and at different frequencies and *EIA*'s have been collected from the literature to assist the modeling.

Tran et. al. [25] had provided emissivity measurements collected from TOPEX/Poseiden microwave radiometer (TMR) at nadir for the frequencies of 18, 21, and 37 GHz. It was noticed that these emissivity measurements had a DC bias of the order of 0.6-1.2 Kelvin. This DC bias was removed from these observations before it was used in the CFRSL *g(EIA,ws,freq)* modeling. On the other hand Meissner and Wentz [24] had provided an emissivity model for the Advanced Microwave Scanning Radiometer (AMSR). This model has been discussed earlier in chapter 2 of this dissertation. The CFRSL model had relied on these two measurement sources and the resulted foam emissivity and foam fraction extracted earlier to solve for *g(EIA,ws,freq)*. The results are shown in Eq. (3.18) for various regions of frequency and both vertical and horizontal polarizations, and the coefficients are provided in Appendix C.

g(EIA,ws,freq) for frequencies < 2 GHz and >7GHz for H-pol,

$$g(EIA, ws,\ freq) = (a_1 * LOREIA(a_2, a_3) + a_4 * LORWS(a_5, a_6) + a_7 * LOREIA(a_2, a_3) * LORWS(a_5, a_6))\sqrt[4]{freq} \quad (3.18.a)$$

where,

$$LOREIA(y, z) = 0.5 + \tan^{-1}\left(\frac{EIA - y}{z * \pi}\right)$$

$$LORWS(y, z) = 0.5 + \tan^{-1}\left(\frac{ws - y}{z * \pi}\right)$$

g(EIA,ws,freq) for frequencies < 2 GHz and >7GHz for V-pol,

$$g(EIA, ws, freq) = (a_0 + a_1 * EXEIA(a_2, a_3) + a_4 * EXWS(a_5, a_6) + a_7 * EXEIA(a_2, a_3) + EXWS(a_5, a_6))\sqrt[4]{freq} \quad (3.18.b)$$

where,

$$EXEIA(y, z) = \exp\left(-1 * exp\left(\frac{y - EIA}{z}\right)\right)$$

$$EXWS(y, z) = \exp\left(-1 * exp\left(\frac{y - WS}{z}\right)\right)$$

The C-band results had been presented earlier in this chapter. Between the ranges assigned for each equation, a simple linear interpolation was applied. Comparisons with real time data are provided in chapter 4.

3.4 Wind Direction

For the emissivity model to be complete, the effect of wind direction ($\Delta\varepsilon_{wind\ direction}$) must be included as previously specified in Eq. (3.1). The effect of wind direction on the total emissivity has been previously addressed by many researchers in the literature [23-25].

It was shown that the emissivity is anisotropic with relative wind direction and has a direct effect on the total emissivity, and the relationship between the emissivity and wind direction is well defined by Maxwell equation shown in Eq. (2.11). The coefficients of the Fourier series depend on wind speed, frequency, incidence angle, and polarization.

3.4.1 Near Nadir Wind Directional Modeling

Also at nadir it has been demonstrated that there is a small change in brightness temperature due to wind direction. This sensitivity comes from the fact that the thermal emission from anisotropic sea waves depends upon azimuthal polarization at nadir observation angles. Several experimental studies have addressed this sensitivity to wind vector by means of circle flights [45]. These aircraft measurements indicate a direction detection capability for nadir-looking systems.

Tran et. al. [25], analyzed global brightness temperature observations of the TOPEX/Poseidon microwave radiometer (TMR) at 18, 21, and 37 GHz, and he concluded that there is an effect on the total emissivity due to wind direction even at nadir. His results showed that the dependence is weak and linear for wind speeds below 7 m/s with an increase in sensitivity over the range of wind speed from 0 – 20 m/s. These results were used in this dissertation as points of reference for the wind direction emissivity model at nadir. For low frequencies, Trokhimovski et. al. [46] showed similar results for S-band sea surface brightness temperature at nadir from aircraft measurements. In his experiment, he collected data from 65 circular flights, which demonstrated the ability to measure wind direction at nadir.

The results from these researchers were combined to converge to wind directional emissivity model which is shown in Eq. (3.19).

$$E_{i1} = a_0 + a_1 WS^{b1} + a_2 freq^{b2} + a_3 WS^{b1} freq^{b2} \tag{3.19}$$

where,

E_{i1} is the first harmonic coefficient in Eq. (2.11), i = V, H- pol,

b_i is power coefficient where , i = 1, 2 which are shown in Table 3.9, and

a_i is coefficients where , i = 0-3 , which are shown in Table 3.10.

Table 3.9 b_i coefficient

Coefficient	Value
b_1	1.3655
b_2	3.5923

Table 3.10 a_i coefficients

Coefficient	Value
a_0	-2.075×10^{-4}
a_1	4.429×10^{-5}
a_2	3.292×10^{-11}
a_3	2.472×10^{-11}

As it can be noticed in Eq. (3.19), we only have the first harmonic, implying that $E_{i2} = 0$. These results were consistent with the literature and researchers observations which showed a very weak and negligible dependence on E_{i2}.

3.4.2 Off-Nadir Wind Directional Modeling

As mentioned earlier, the effect of wind direction on ocean emissivity is dependent on both *EIA* and polarization. There are several off-nadir wind direction emissivity models

published in the research journals like Yueh and Wilson [47] and Germain and Poe [48]; but we have picked the Meissner and Wentz [24] model as our point of reference as it showed good correlation with five different T_b data sets collected from satellites, aircraft, which have been compared with buoys.

Meissner and Wentz derived the wind directional effect on emissivity from 5 different data sources that included observations from SSM/I, TMI, QuikSCAT, Buoys, and Reynolds weekly *SST* maps. In their analysis, they provided the relationship for three different frequencies (11, 19 and 37 GHz) at 53 degrees and their results were comparable to other observations like recent JPL aircraft radiometer (WINDRAD) measurements [23] and the two-scale surface emission model [27]. In their observations, it was noted that the anisotropy for vertical polarization is essentially 1st harmonic and the horizontal polarization is 2nd harmonic, which is consistent with other researchers.

In this dissertation we adopted this work from Meissner and Wentz and extrapolated their results to different regions of frequencies. The results from these extrapolations are shown in Eq. (3.20) and the coefficients for vertical and horizontal polarizations are provided in Appendix D.

$$\mathrm{E_{ip}} = \frac{\sum_{n=0}^{3} a_n * ws^n + a_4 * \ln(freq) + a_5 * (\ln(freq))^2}{\sum_{d=0}^{2} b_d * ws^d + b_3 * \ln(freq) + b_4 * (\ln(freq))^2} \tag{3.20}$$

where,

ln(x) is the natural logarithmic of *x*.

Between nadir and 53 degrees a simple linear interpolation was applied to compute the wind directional effect.

CHAPTER 4 : EMISSIVITY MODEL COMPARISONS

The CFRSL ocean emissivity model, given in Eq. (3.7), has been experimentally validated over a limited range of frequency, wind speed and incidence angle using independent SFMR measurements from NOAA aircraft flights in hurricanes Gustav and Dolly in 2008. Also comparisons of the CFRSL model results to previously published emissivity models used in the development process are provided in this chapter.

4.1 Emissivity Comparisons over Wind Speed

This section focuses on the evaluation of the CFRSL ocean emissivity model over wind speed. Comparisons are presented with other emissivity data sources over the applicable ranges of *EIA* (nadir - 60 degrees), polarization (vertical and horizontal), frequency (1.4 - 37 GHz), and wind speed (up to Cat. 5 hurricane).

4.1.1 Foam Fraction and Emissivity Comparisons

The derivation of the foam fraction in Eq. (3.7) was based on SFMR nadir measurements. The foam fraction parameterization versus wind speed was derived iteratively to minimize the mean square difference between the CFRSL emissivity model at nadir and the SFMR excess emissivity algorithm. The CFRSL derived foam fraction is shown in Fig. 4.1 along with independent measurements of foam fractional coverage (FFC) from the Coupled Boundary Layers Air-Sea Transfer (CBLAST) experiment [49]. These independent foam coverage data,

that are derived from airborne visible imagery in the North Atlantic from Callaghan [50], Bondur and Skarkov [51], and Monahan and Woolf [22], compare well with our model. Also, the Melville/Kleiss CBLAST and GOTEX Foam Whitecap Coverage (FWC) were added to Fig. 4.1 for completeness and to show the difference between FWC and FFC, where FFC is the main interest because it represents the total foam coverage (whitecaps and streaks), which contributes to microwave emissivity.

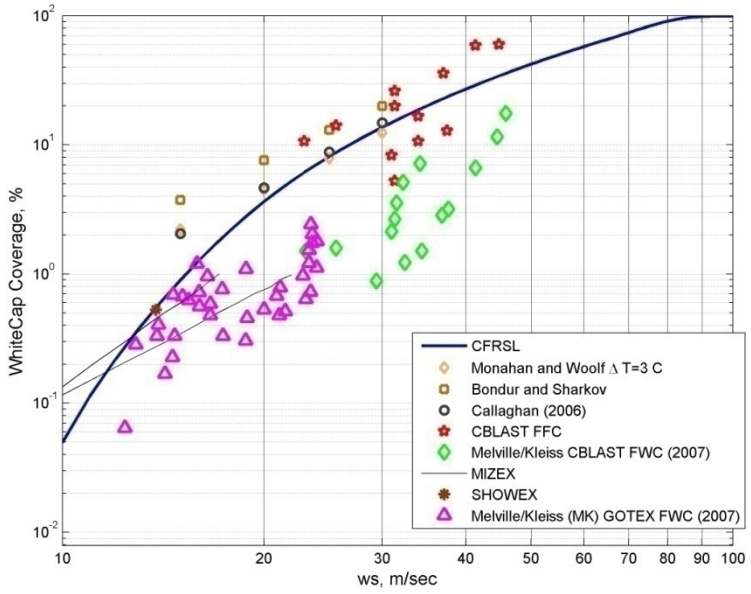

Figure 4.1 Estimates of hurricane foam fraction from Melville (shown as symbols) and CFRSL foam fraction model (shown as solid line).

The extrapolation of the CFRSL emissivity model to higher and lower frequencies at high wind speeds was based on independent foam emissivity measurements that were collected from the literature as explained earlier in chapter 3.

The CFRSL foam emissivity model was tuned to a number of experimental foam emissivity measurements like Camps et. al. [20] measurements of foam using the L-band Automatic radiometer (LAURA) [52], which was made to perform studies for the next SMOS mission, and Zheng et. al. [44] foam emissivity measurements reported in Yang et. al. [42] for correction of Jason1 emissivity measurements from foam are shown in Fig. 4.2. As frequency increases the emissivity of foam increases sharply in the lower frequency range and asymptotically approaches a black body at higher frequencies.

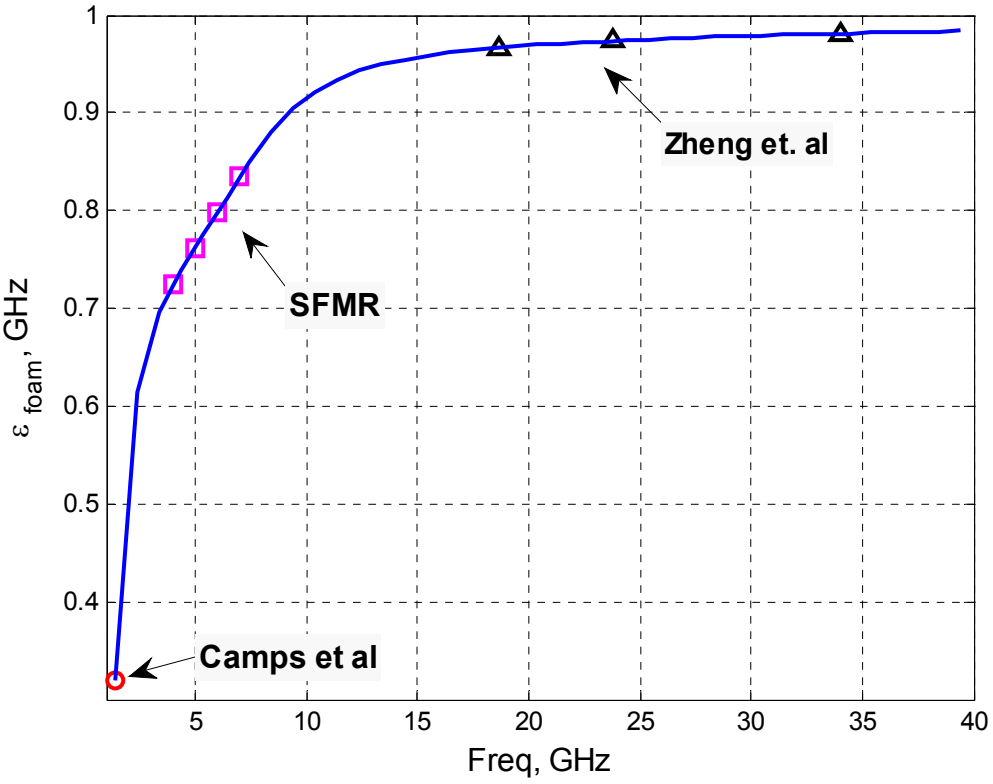

Figure 4.2 CFRSL emissivity of foam at nadir (blue line) in comparisons with measurements of foam from LAURA (red circle) and Jason1 (black triangles).

It was noted earlier in this dissertation that the emissivity of foam is more sensitive at C-band to foam thickness compared to other frequencies. This was noted in the literature by many researches such as Reul [21], and Yang et. al. [42]. Yang et. al. noted that microwave reflectivity of Ku-band is significantly affected by even very thin foam layers, when the foam thickness is more than 0.3 cm, the reflectivity of Ku-band is less than 15%, while the reflectivity of C-band is more than 40% as shown in Fig. 4.3.

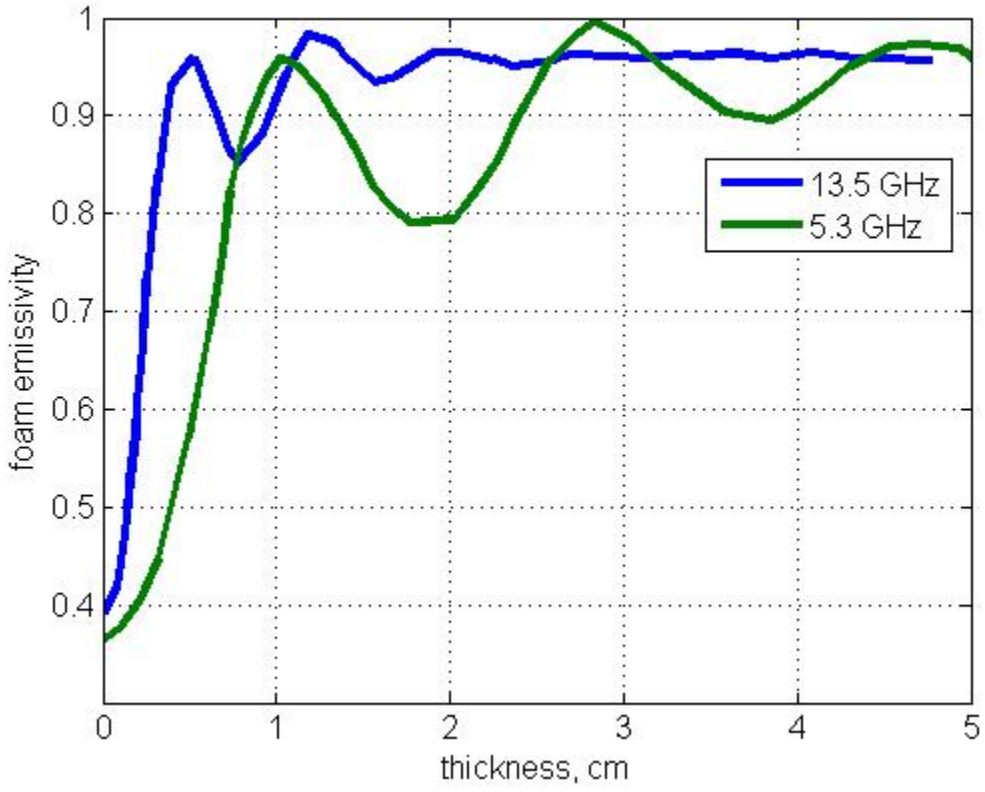

Figure 4.3 Foam thickness with respect to foam emissivity for C and X band.

Results for foam emissivity modeling extrapolation are shown in Fig. 4.4 for both vertical and horizontal polarizations, respectively. In the figures shown, measurements of foam emissivity from Rose et. al. [18] are between 30-60 degrees. The surface represents the CFRSL foam emissivity model. The CFRSL model shows a good comparison with Rose measurements to within one standard deviation. The CFRSL model tends to have more sensitivity for H-pol than V-pol which complies with measurement observations reported by Rose et. al.[18] and Padmanabhan et. al. [19] .

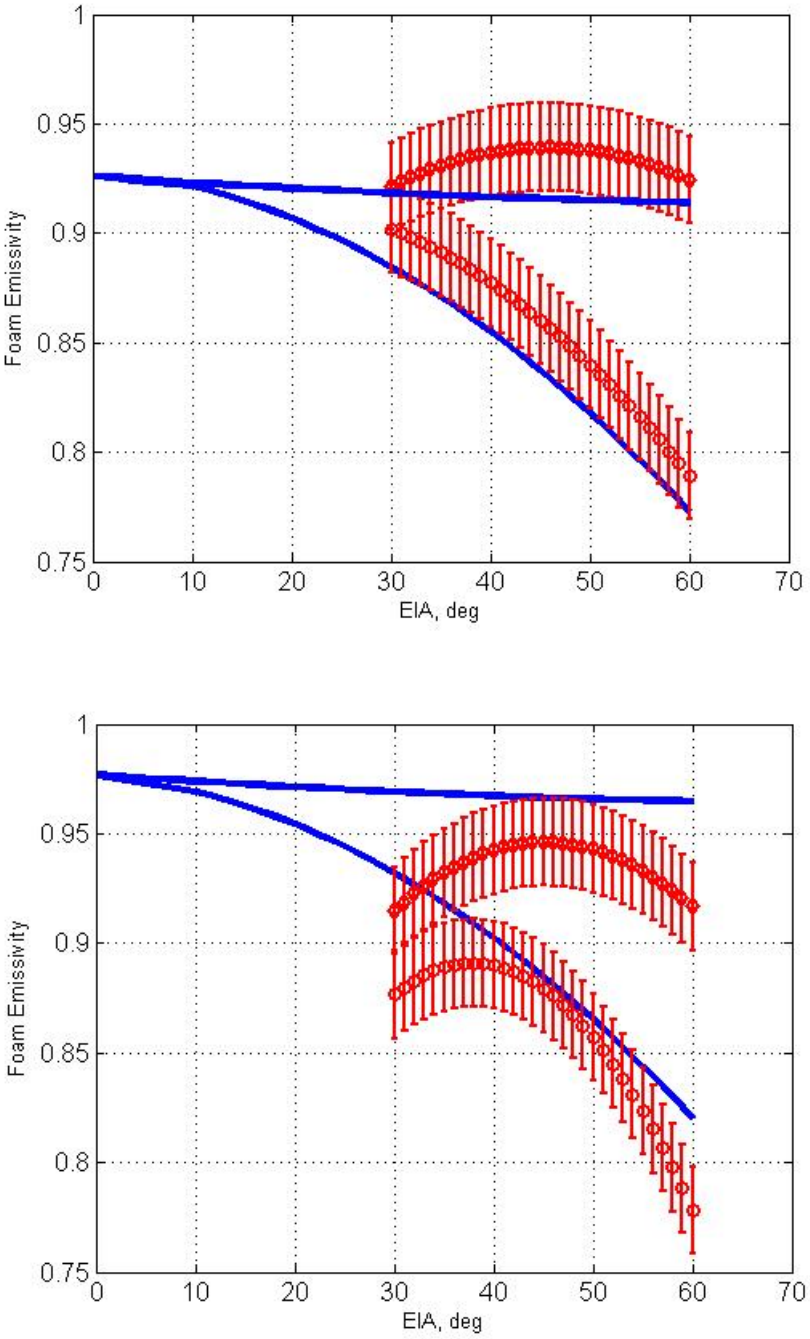

Figure 4.4 The CFRSL emissivity of foam (blue lines) in comparison with Rose et. al. (red circles) for 10.8 GHz (upper panel) and 36.5 GHz (lower panel).

4.1.2 CFRSL Emissivity Model Comparisons

The CFRSL emissivity model at nadir was based on the NOAA/SFMR emissivity model for relatively high wind speeds, *ws* > 10 m/s, and the Stogryn emissivity model for *ws* < 10 m/s. Figure 4.5 shows comparisons between Wilheit, Uhlhorn and CFRSL rough emissivities scaled to 300 Kelvin for wind speeds < 10 m/s at 6.6 GHz.

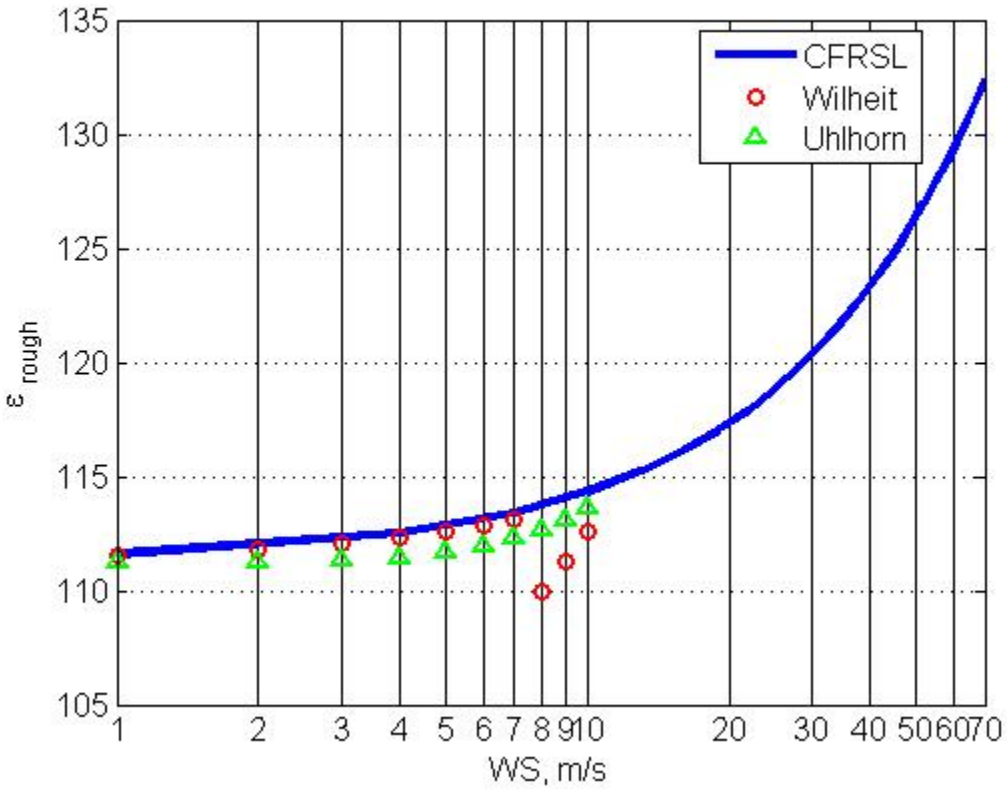

Figure 4.5 CFRSL rough emissivity for SST = 300 Kelvin, in comparison with Uhlhorn and Wilheit at Nadir and 6.6 GHz.

For wind speeds > 10 m/s the CFRSL model was compared to the NOAA/SFMR model in terms of emissivity and the results are shown in Fig. 4.6. The difference between the two models is less than one Kelvin (1 K) over the whole range of wind speeds from (12-70) m/s with

an RMSE of 0.62 Kelvin. As can be seen in Fig. 4.6, there was some oscillation in the difference, this oscillation was due to the change in slope of the CFRSL emissivity model with respect to wind speed as it can be seen from the (green curve). The NOAA/ SFMR emissivity model is linear beyond 30 m/s, which means that it will keep growing with wind speed, and will eventually saturate at an emissivity equals to 1.0 (blackbody). The non-linear nature of the CFRSL emissivity model at high wind speeds, made it possible to asymptotically approach 1 at very high wind speeds (>100 m/s). The validity of this assumption is not known, but it can be easily adjusted as higher wind speed measurements become available.

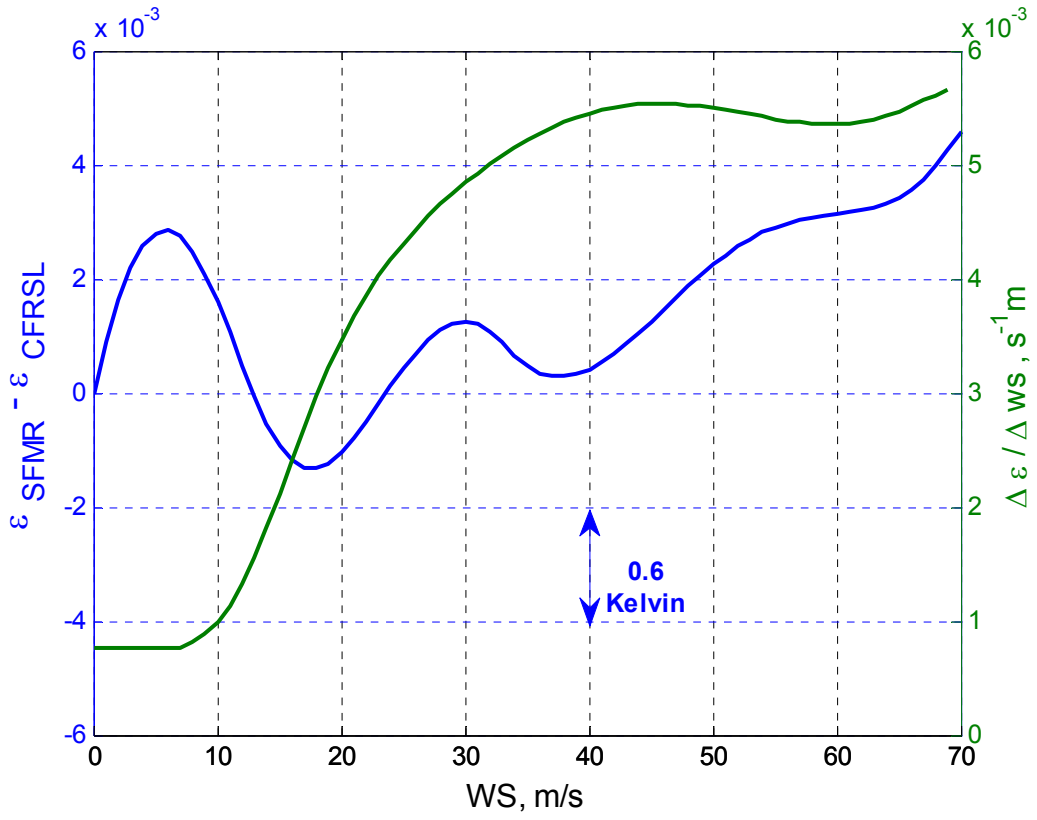

Figure 4.6 Difference between SFMR and CFRSL surface emissivity model comparisons at 4 GHz (blue curve), along with the first derivative of the emissivity with respect to wind speed at 4 GHz (green curve).

Results presented in Fig. 4.7 show the total ocean emissivity measurements in the range 5 ≤ *ws* ≤ 20 m/s averaged over the six SFMR frequencies, where emissivities based upon experimental observations (symbols) were from SFMR (nadir - 35°) and Wentz (49°- 57°). CFRSL model results (solid lines) are in excellent agreement with these total ocean emissivity values for both polarizations. For V-pol, the number of SFMR observations is significantly less, and the resulting regression fit for the CFRSL emissivity model has much higher residuals. This was especially true for SFMR measurements between (20°- 30°), which were believed too low because of bias errors in the atmospheric clearing for rain effects; but we believe that our model's monotonic dependence on *EIA* is more consistent with electromagnetic theory than are the SFMR measurements during aircraft banked turns.

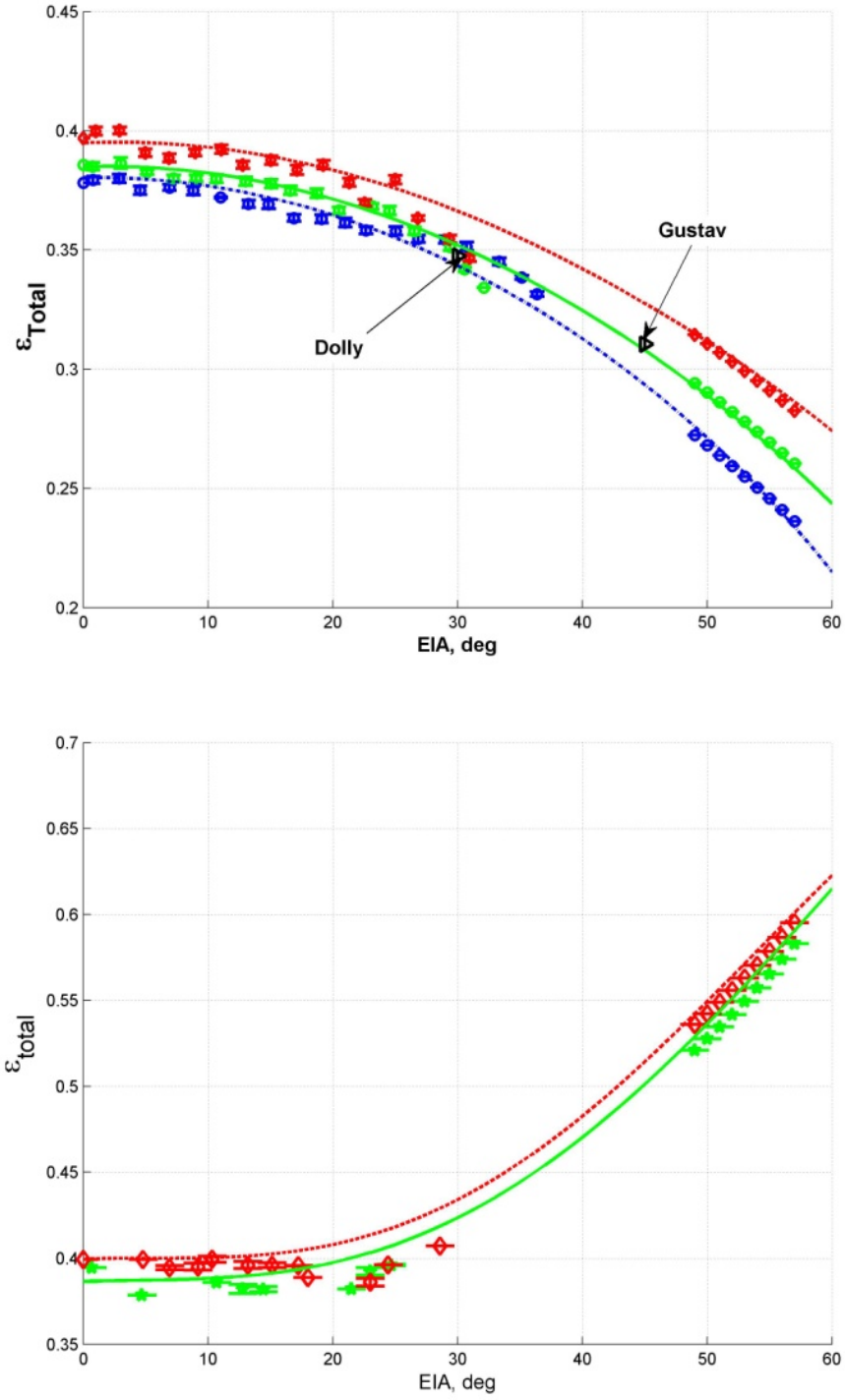

Figure 4.7 Total ocean emissivity for H-pol (upper), and V-pol (lower) for wind speed bins of (5-10 m/s) '○' , (10-15 m/s) '*' & '►', and (15-20 m/s) '◊', where horizontal bars represent one-standard deviation of the binned average over all SFMR 6 frequencies.

For wind speeds (*ws* > 20 m/s), foam becomes the dominant contributor to ocean surface emissivity and SFMR and WindSat hurricane observations were used to estimate the foam emissivity dependence on wind speed and *EIA*. Results for H and V-pol are shown in Fig. 4.8. Because of spatial averaging over the large antenna footprint (40 x 60 km), we believe that the WindSat emissivities [37] for both V-pol and H-pol are progressively underestimated with increasing wind speed.

Results presented in Fig. 4.8 compare the CFRSL model with surface emissivity values, derived from SFMR and WindSat, over the wind speed range of 20 – 45 m/s. For H-pol (upper panel), the model (solid lines) exhibits excellent agreement with the SFMR, but the agreement with WindSat is slightly degraded as the wind speed increases. As discussed above, we believe that the WindSat emissivities are too low because of spatial averaging over the large antenna footprint. On the other hand, the V-pol comparisons of the CFRSL model with the SFMR and WindSat data exhibits relatively larger differences. As discussed above, we attribute this to the lesser quality of the SFMR and WindSat data.

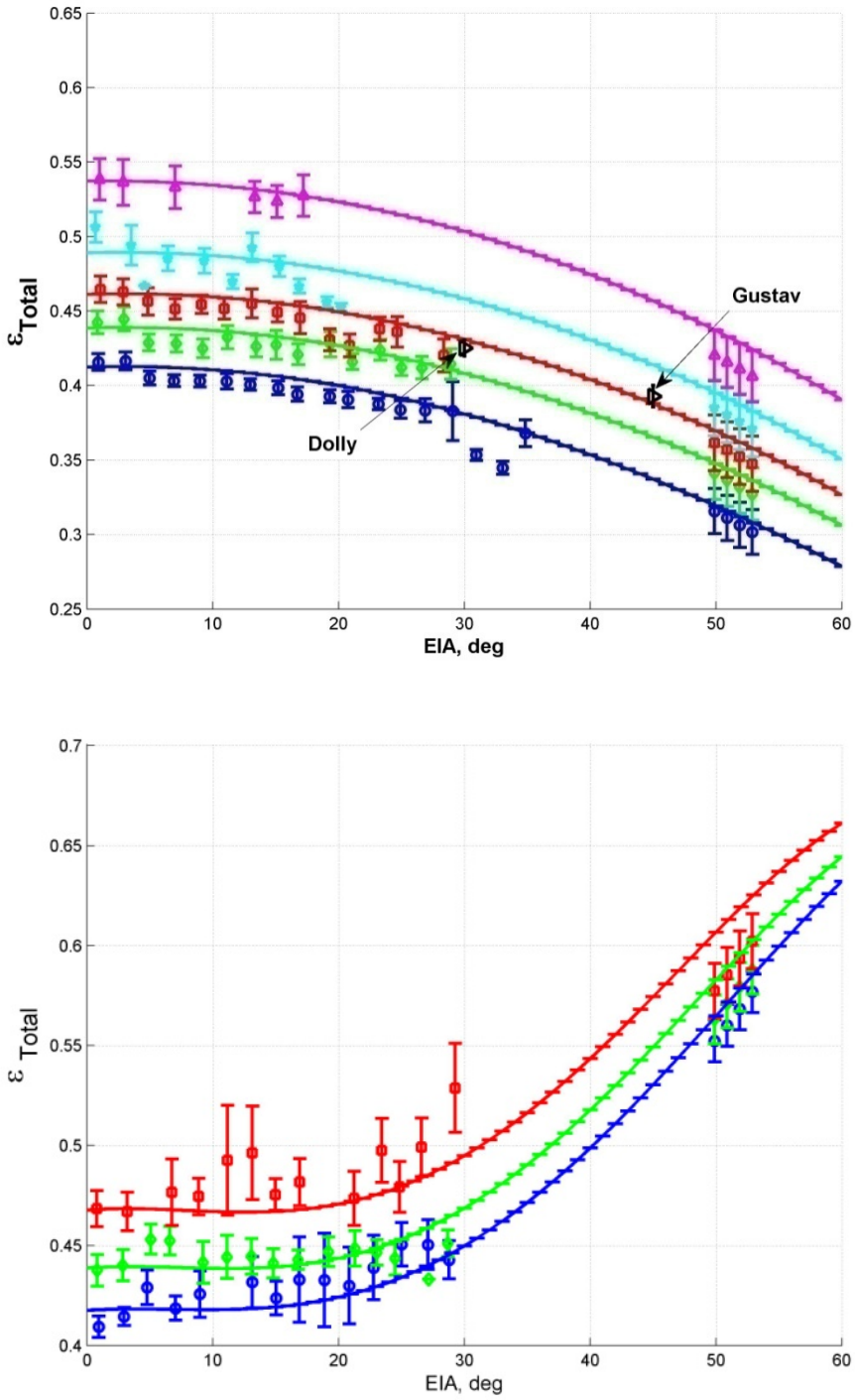

Figure 4.8 Total ocean emissivity H-pol (upper) and V-pol (lower) for wind speed bins (20-25 m/s) '○', (25-30 m/s) '◊', (30-35 m/s) '□' & '►', (35-40 m/s) '*', and (40-45 m/s) '▲', where horizontal bars represent one-standard deviation of the binned average over all SFMR 6 frequencies.

Finally, two independent SFMR measurements of total ocean emissivity are available from NOAA HRD during the 2008 hurricane season (Hurricanes Dolly, and Gustav). In these experiments, the NOAA WP3 aircraft flew consecutive circles at 30° and 45° banks in clear (rain-free) regions with surface wind speeds of 15 m/s (See Fig. 4.8 upper panel) and 35 m/s (See Fig. 4.8 upper panel) [5]. Since these measurements were not used in the CFRSL model development, they were included in Fig. 4.7 and Fig. 4.8 as points of independent comparison. There is excellent agreement with the CFRSL model for these two high-quality, off-nadir emissivity measurements. We compile the RMS differences between the CFRSL model and the other emissivity sources used in this dissertation as presented in Fig. 4.5 and 4.6. Results are provided in Table 4.1 for low, moderate and high wind speeds for both vertical and horizontal polarizations over the whole dynamic range of incidence angles up to 60 degrees (excluding the WindSat measurements).

Table 4.1 RMS difference for C-Band CFRSL fit to SFMR and WindSat measurements

WS, m/s	RMSE	
	H-Pol	V-Pol
5 – 10	1.38	N/A
10 – 15	1.04	5.14
15 – 20	1.70	5.75
20 – 25	3.17	2.81
25 – 30	2.26	2.90
30 – 35	3.27	5.20
35 – 40	4.42	N/A
40 – 45	2.74	N/A

A comparison between the CFRSL model at 18, 21 and 37 GHz and Tran et. al. [25] and Meissner et. al. [24] at 6 m/s vs. incidence angle are shown in Fig. 4.9. The CFRSL exhibits an excellent comparison to both emissivity models.

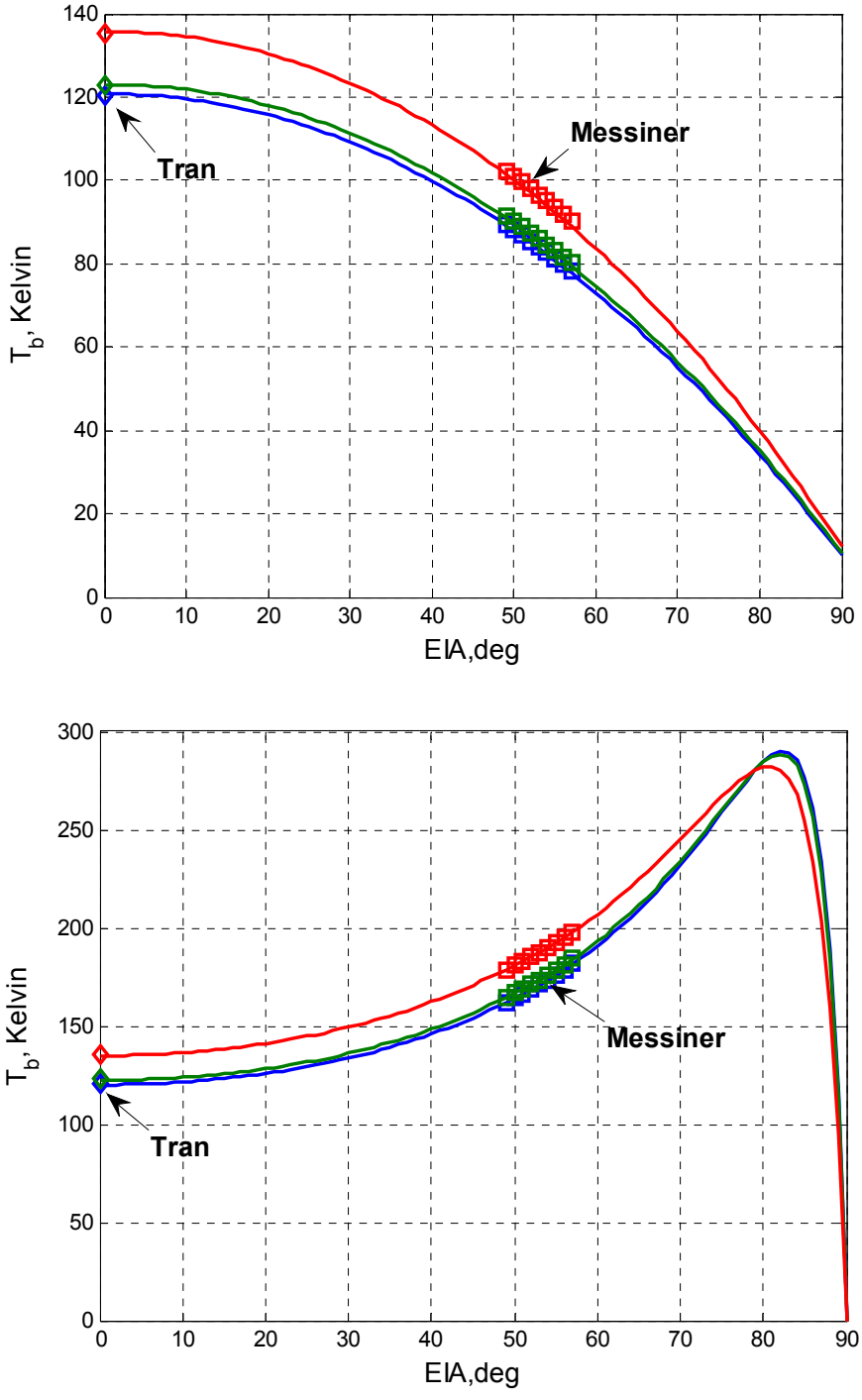

Figure 4.9 CFRSL emissivity for SST = 300 Kelvin, H-pol (upper) and V-pol (lower) for frequencies 18 (blue), 21 (green), and 37 GHz (red) in comparison to Tran et al. (diamond) and Meissner et al. (squares).

4.2 Wind Direction Emissivity Comparisons

The CFRSL wind direction emissivity model was extracted from multiple observations that have been reported in the technical literature as described earlier in this dissertation. Figure 4.10 shows a comparison between the CFRSL induced wind directional emissivity model (1st harmonic amplitude), and the observations of Tran et. al. [25], and Trokhimovski et. al. [46].

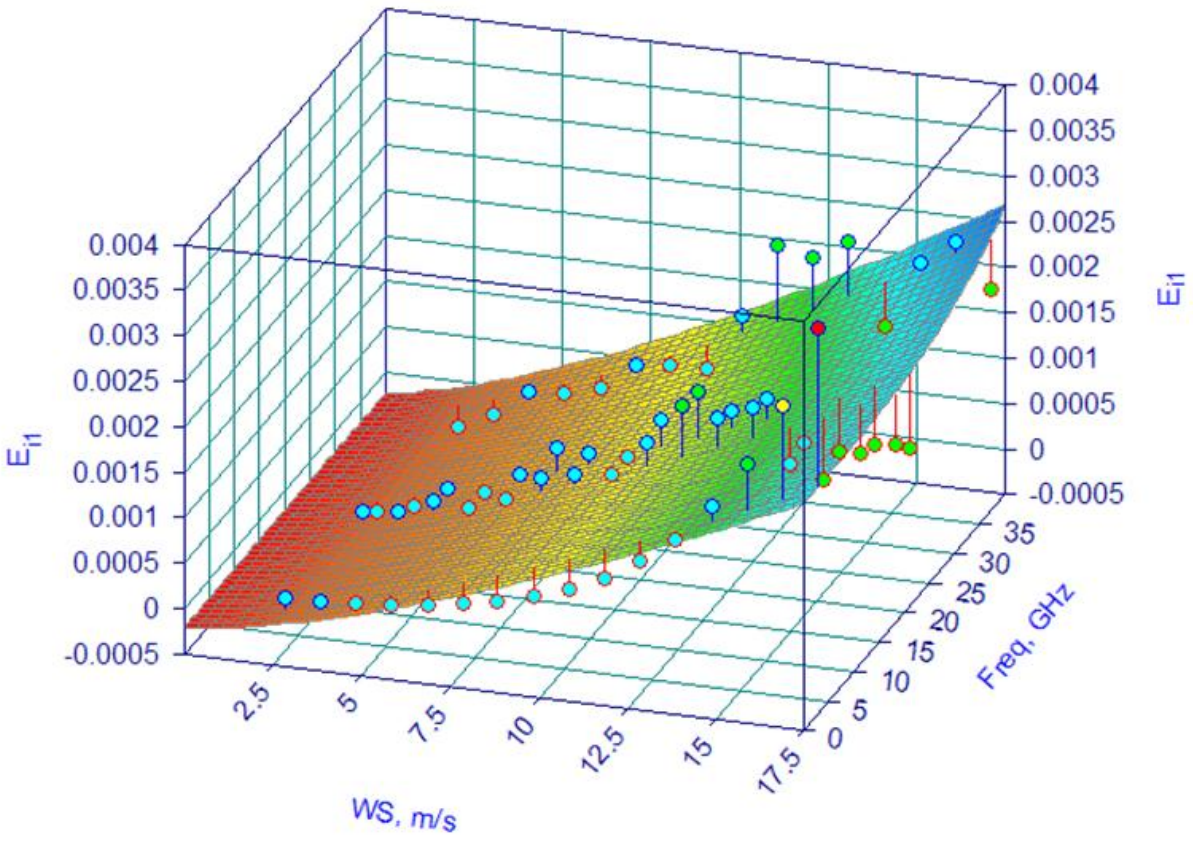

Figure 4.10 CFRSL Nadir wind direction excess emissivity in comparison with Tran (> 3 GHz) and Trokhimovski (S-Band).

The surface fit (CFRSL model) shown in Fig. 4.10 is the best fit to the data points presented in circles within one standard deviation.

Results shown in Fig. 4.11 represent the CFRSL wind direction induced T_b model for vertical and horizontal polarizations (upper and lower panels respectively) in comparison to Meissner and Wentz [24] model. The CFRSL was mainly dependent on their results at 53 degrees and interpolated and extrapolated their results to other regions.

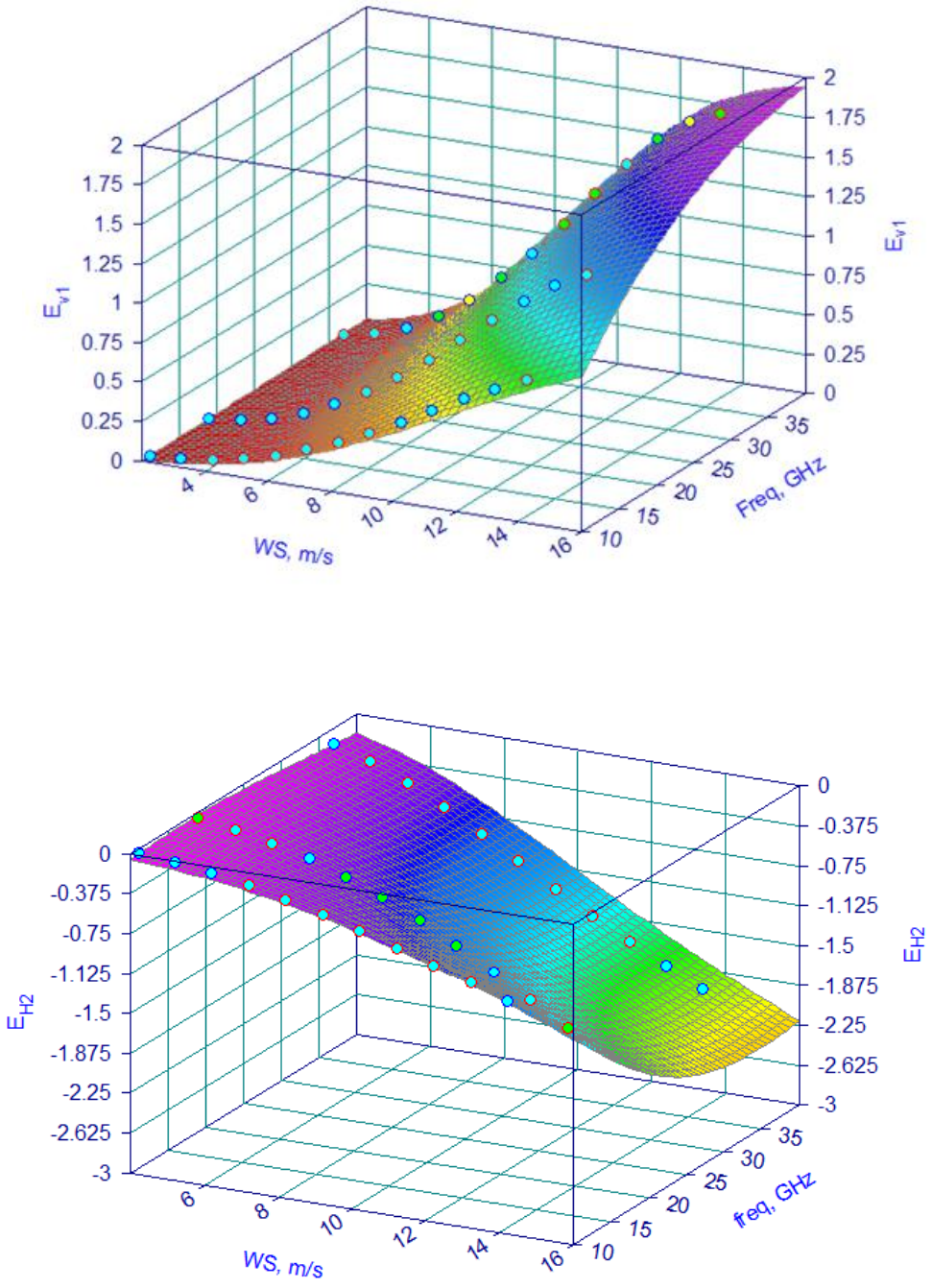

Figure 4.11 CFRSL wind direction excess emissivity in comparison with Meissner and Wentz for Vertical (upper panel, 1st harmonic) and Horizontal (lower panel, 2nd Harmonic) at 53 degrees.

As for the angles between nadir and 53 degrees, the CFRSL model interpolates linearly to get the dependence on wind direction for regions in between. Several parametric plots at different angles and regions are all provided in the next section of this chapter.

4.3 Extrapolated Model Performance

In this section, the CFRSL emissivity model is presented for all regions of wind speeds, incidence angles and frequencies. The main purpose of these parametric plots is to identify the regions of applicability and of limitation of the model.

Even though our model was validated only in the frequency range between 1-37 GHz, we believe that the CFRSL model is probably applicable over the wide frequency range from 1-200 GHz, but it was extrapolated beyond this region, preserving a monotonic increase with respect to frequency, and not showing any saturation. It is although very important to specify the regions of confidence in terms of angles (*EIA*) and wind speeds (*ws*), and the regions were we don't recommend the model to be used. Figure 4.12 shows a summary of the ranges of applicability for the CFRSL foam emissivity model for horizontal and vertical polarizations, where the color of each box represent the level of confidence where green is high confidence (validated against actual measurements), yellow intermediate confidence (we believe it is valid to use), red is low confidence (we do not recommend to use), similar to that are Fig. 4.13 and Fig. 4.14 for CFRSL wind induced emissivity, and ocean surface emissivity respectively.

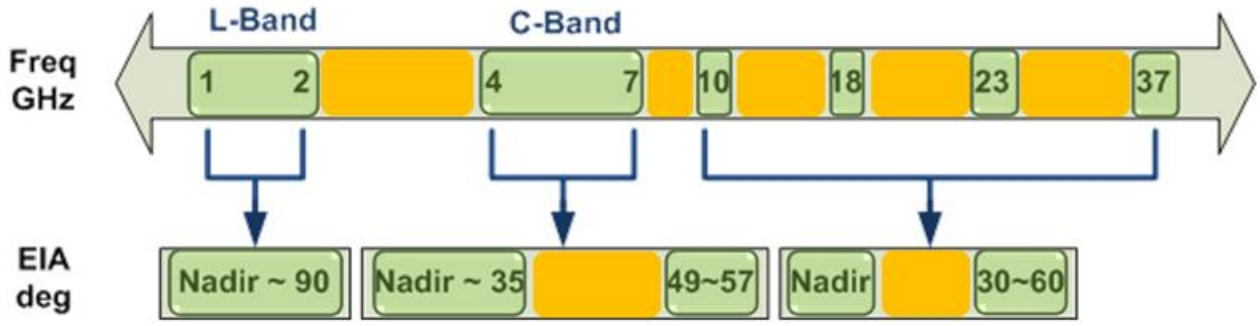

Figure 4.12 CFRSL foam emissivity confidence interval.

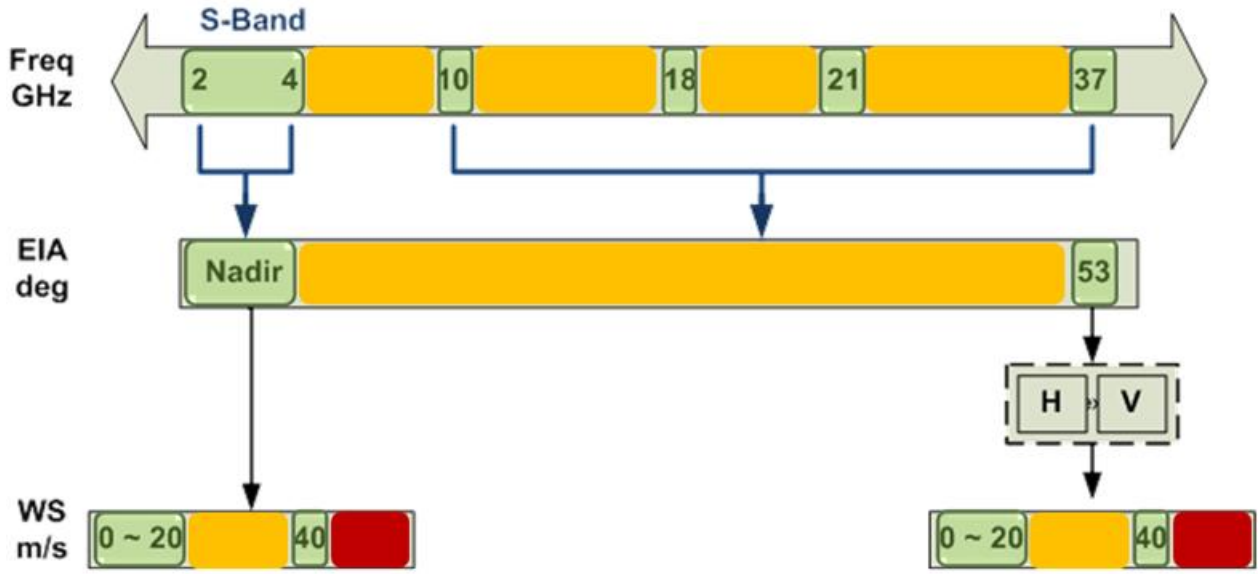

Figure 4.13 CFRSL wind induced emissivity confidence intervals.

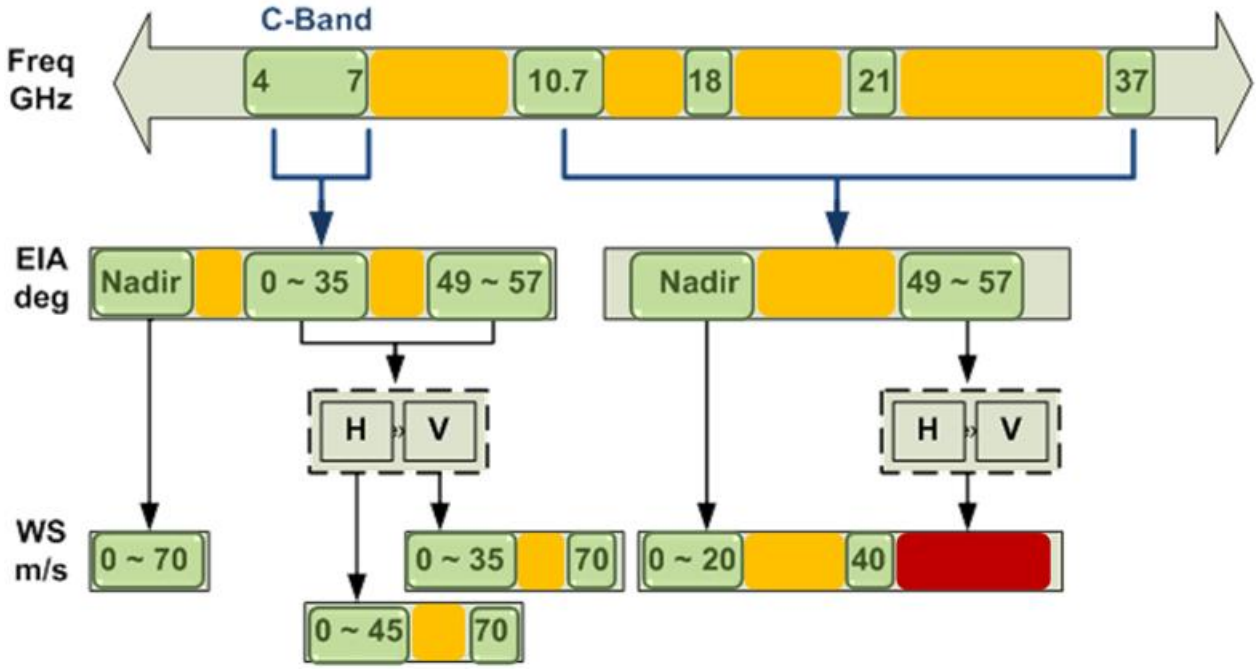

Figure 4.14 CFRSL total ocean surface emissivity confidence interval.

A collection of parametric plots shown next provides another measure of examining the CFRSL model and the manner that it performs as a function of wind speed (Fig. 4.15 and Fig. 4.16), incidence angles (Fig. 4.17 and Fig. 4.18), and frequency (Fig. 4.19) for the horizontal polarization, at C-band .

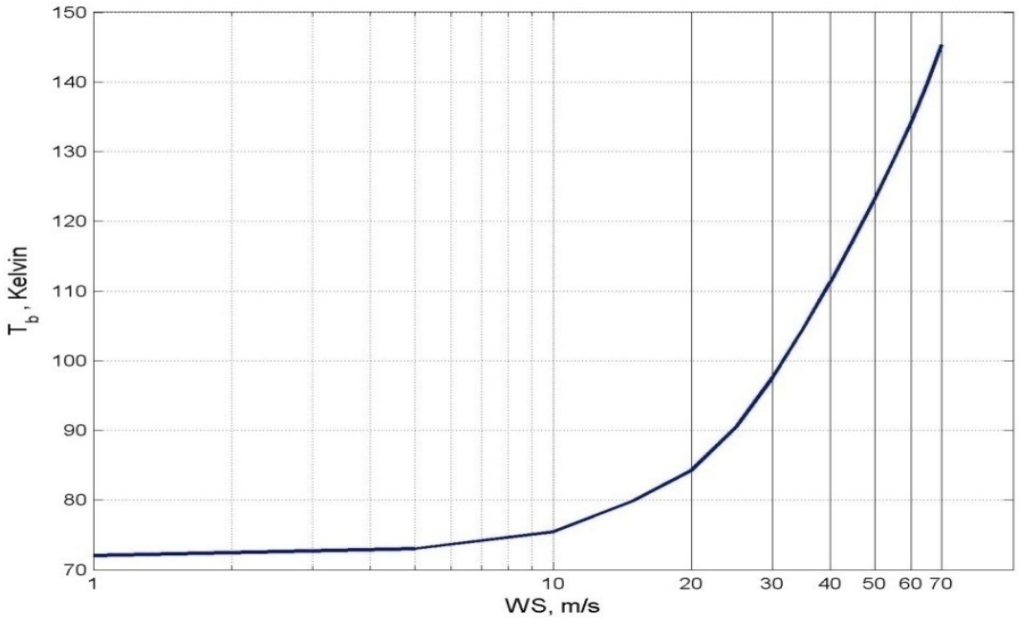

Figure 4.15 CFRSL horizontal emissivity for SST = 300 Kelvin, at 4 GHz and 53 degrees incidence angle.

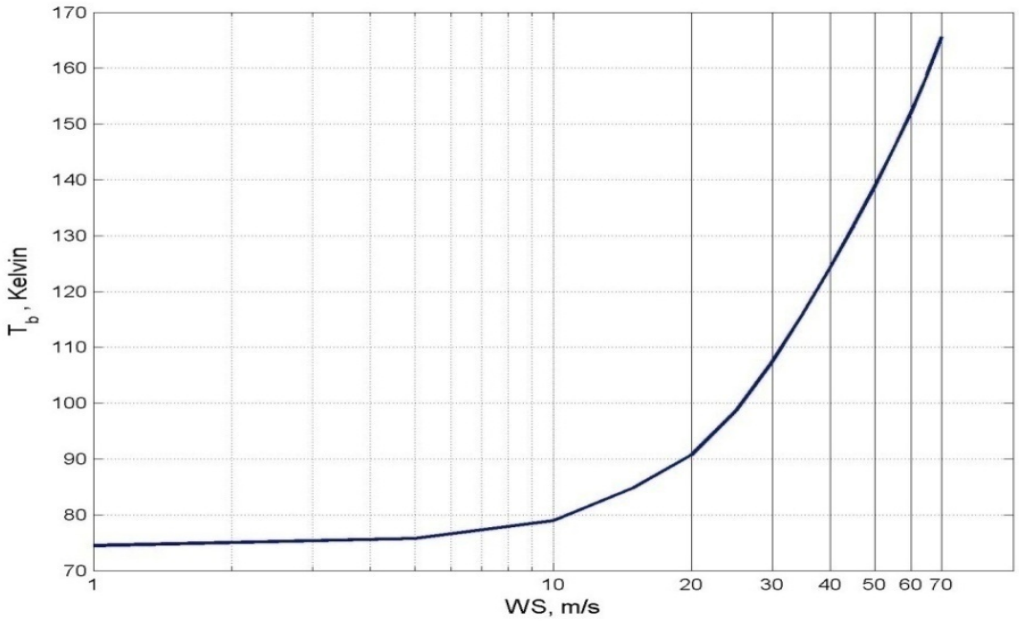

Figure 4.16 CFRSL horizontal emissivity for SST = 300 Kelvin, at 6.9 GHz frequency and 53 degrees incidence angle.

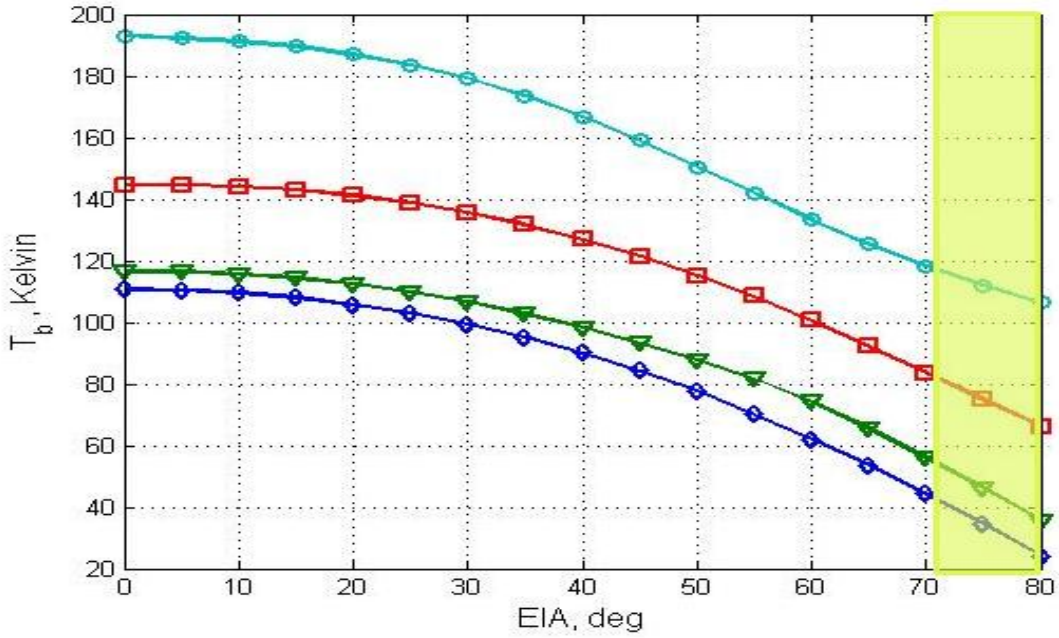

Figure 4.17 CFRSL horizontal emissivity for SST = 300 Kelvin, at 4 GHz and wind speeds of 6, 20, 40 and 70 m/s.

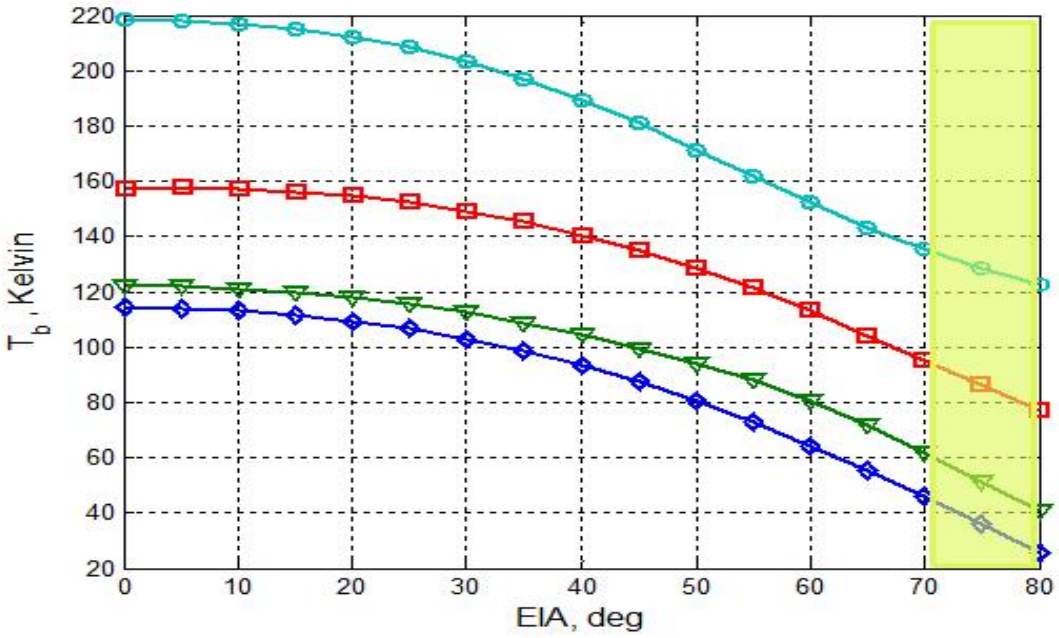

Figure 4.18 CFRSL horizontal emissivity for SST = 300 Kelvin, at 6.9 GHz and wind speeds of 6, 20, 40 and 70 m/s.

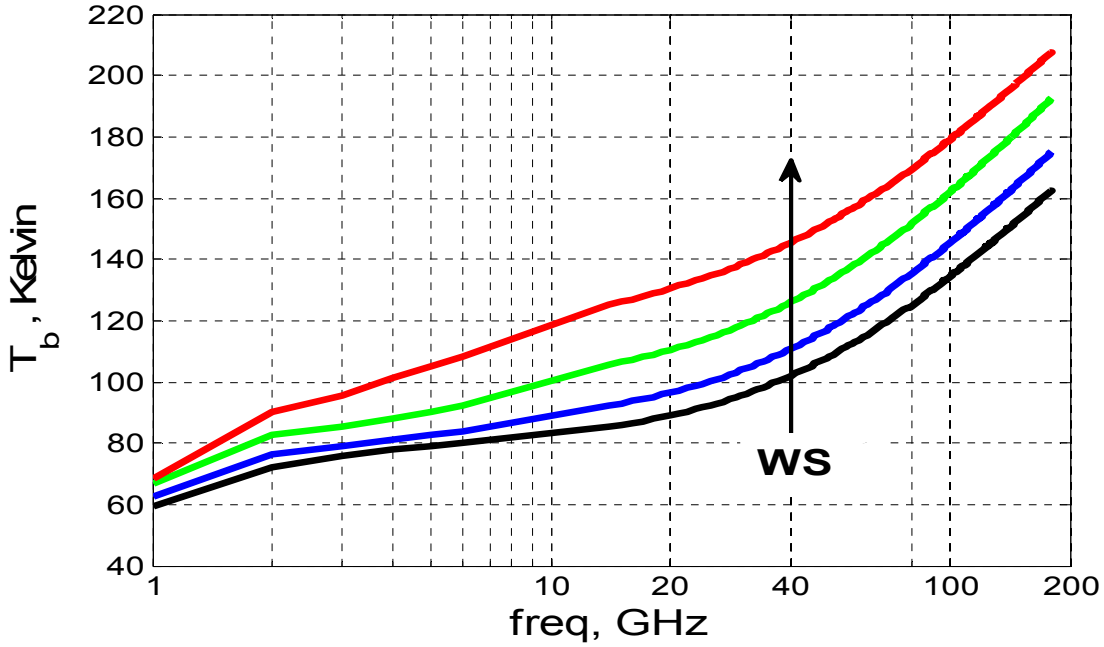

Figure 4.19 CFRSL horizontal emissivity for SST = 300 Kelvin, at 53 degrees and wind speeds of 6, 20, 30 and 40 m/s.

The list of parametric plots shown next represent the vertical polarization of the CFRSL model and its behavior as it is extrapolated with respect to wind speeds (Fig. 4.20 and Fig. 4.21), incidence angles (Fig. 4.22 and Fig. 4.23), and frequencies (Fig. 4.24) at C-band.

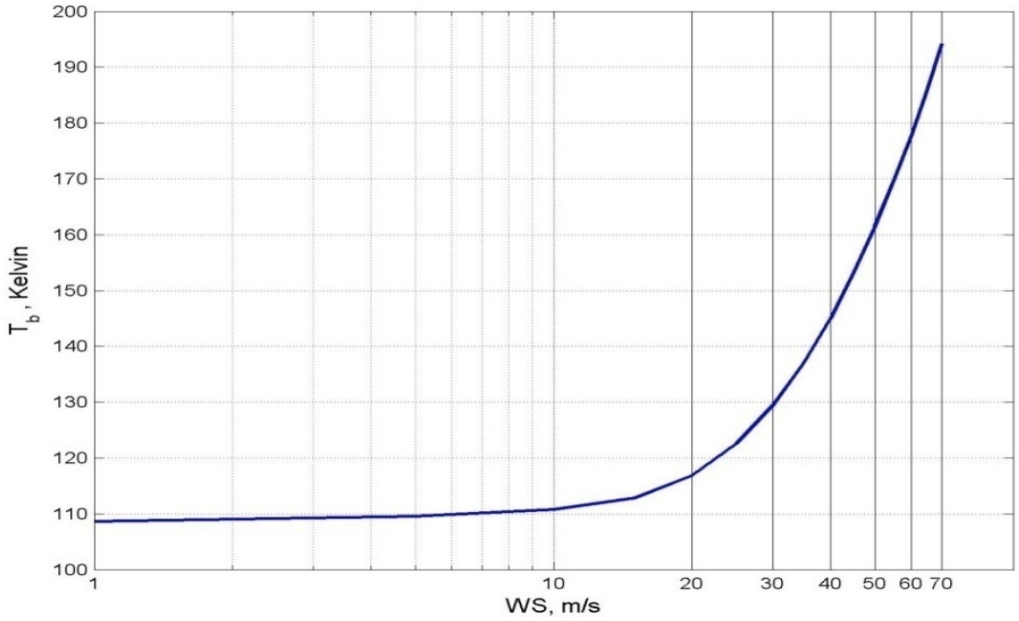

Figure 4.20 CFRSL vertical emissivity for SST = 300 Kelvin, at 4 GHz and 53 degrees incidence angle.

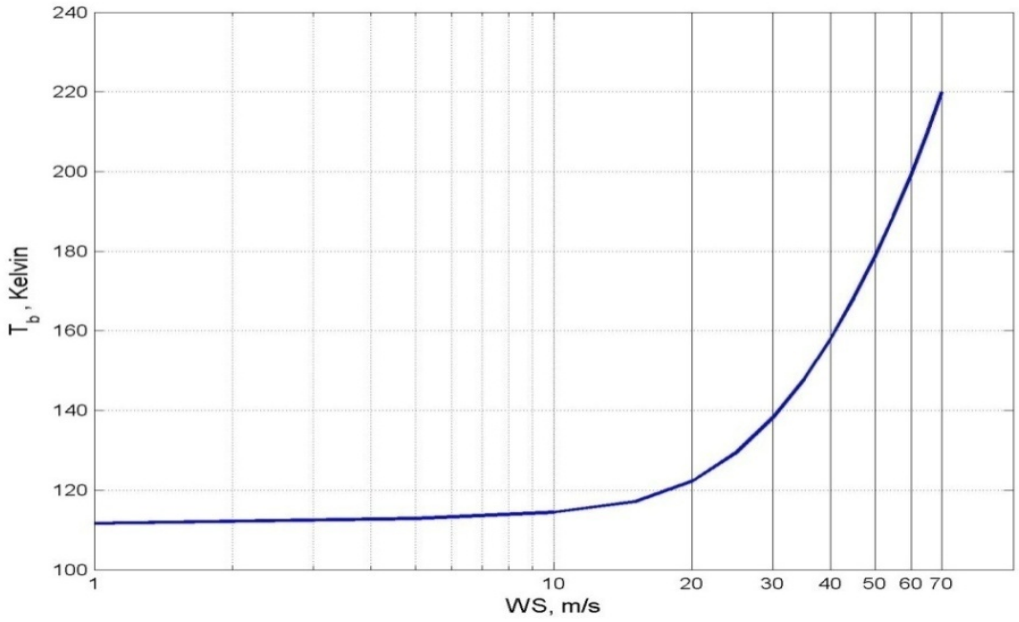

Figure 4.21 CFRSL vertical emissivity for SST = 300 Kelvin, at 6.9 GHz and 53 degrees incidence angle.

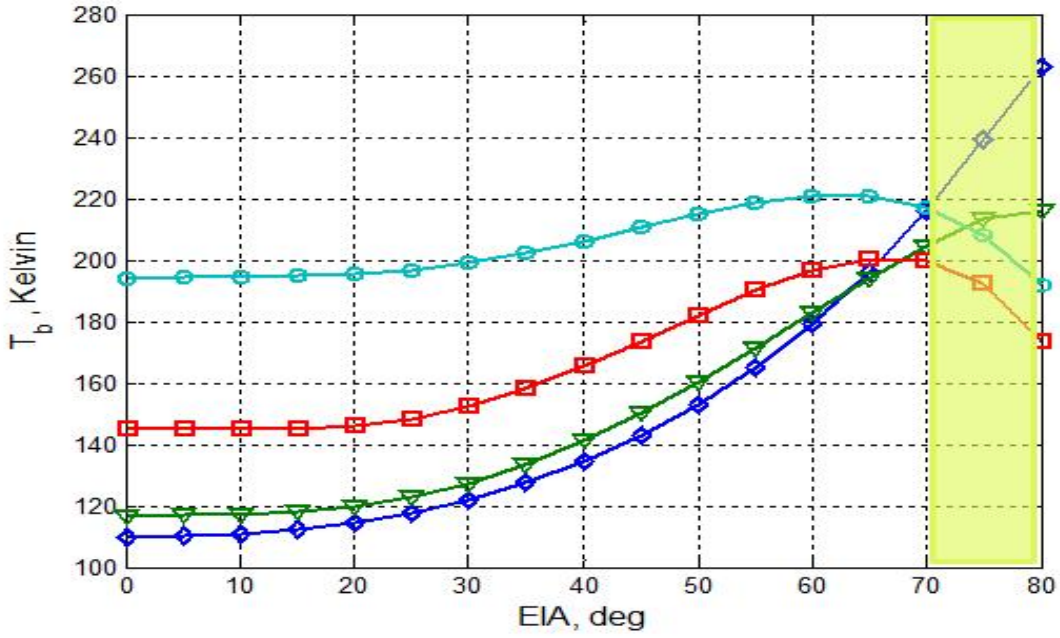

Figure 4.22 CFRSL vertical emissivity for SST = 300 Kelvin, at 4 GHz and wind speeds of 6, 20, 40 and 70 m/s.

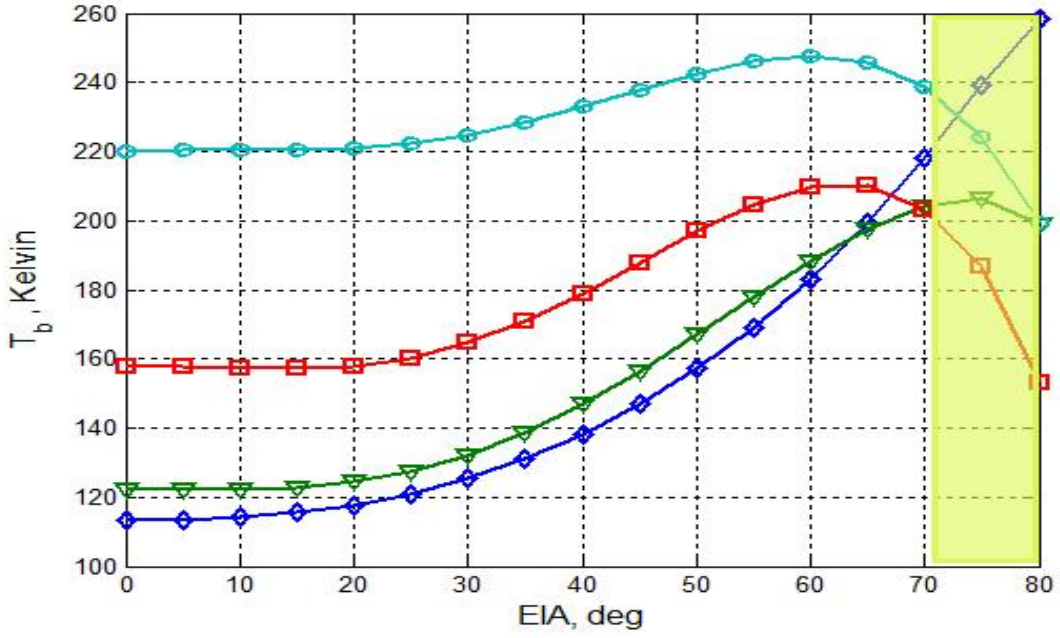

Figure 4.23 CFRSL vertical emissivity for SST = 300 Kelvin, at 6.9 GHz and wind speeds of 6, 20, 40 and 70 m/s.

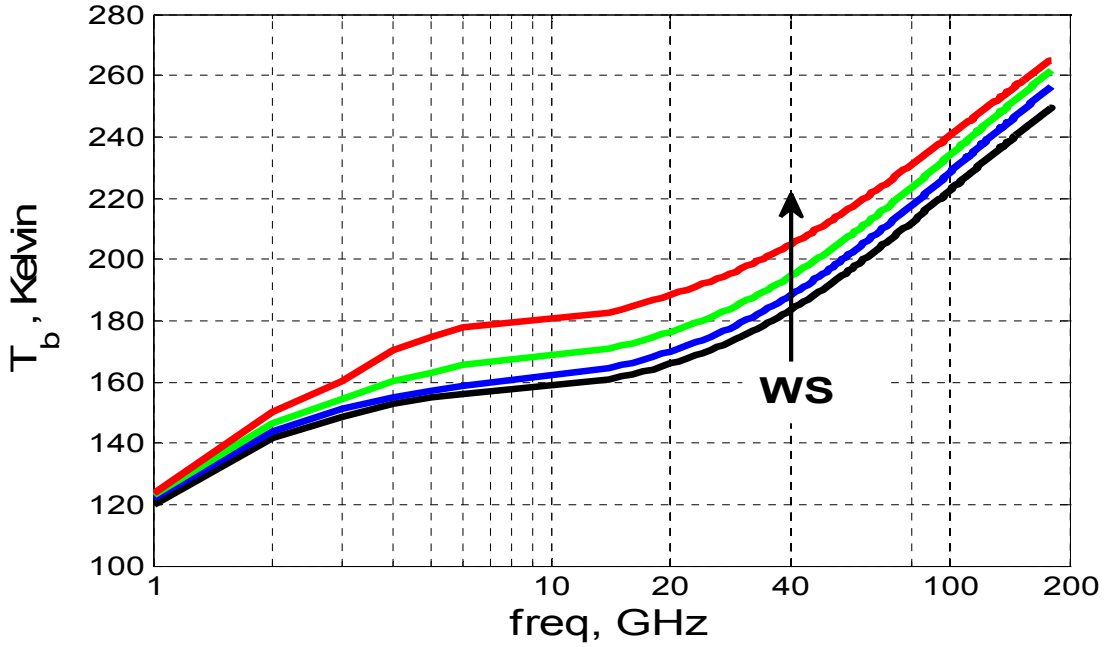

Figure 4.24 CFRSL vertical emissivity for SST = 300 Kelvin, at 53 degrees and wind speeds of 6, 20, 30 and 40 m/s.

Figure 4.25 shows the extrapolation of the CFRSL model at nadir vs. frequency at four different wind speeds (6, 20, 30 and 40) m/s.

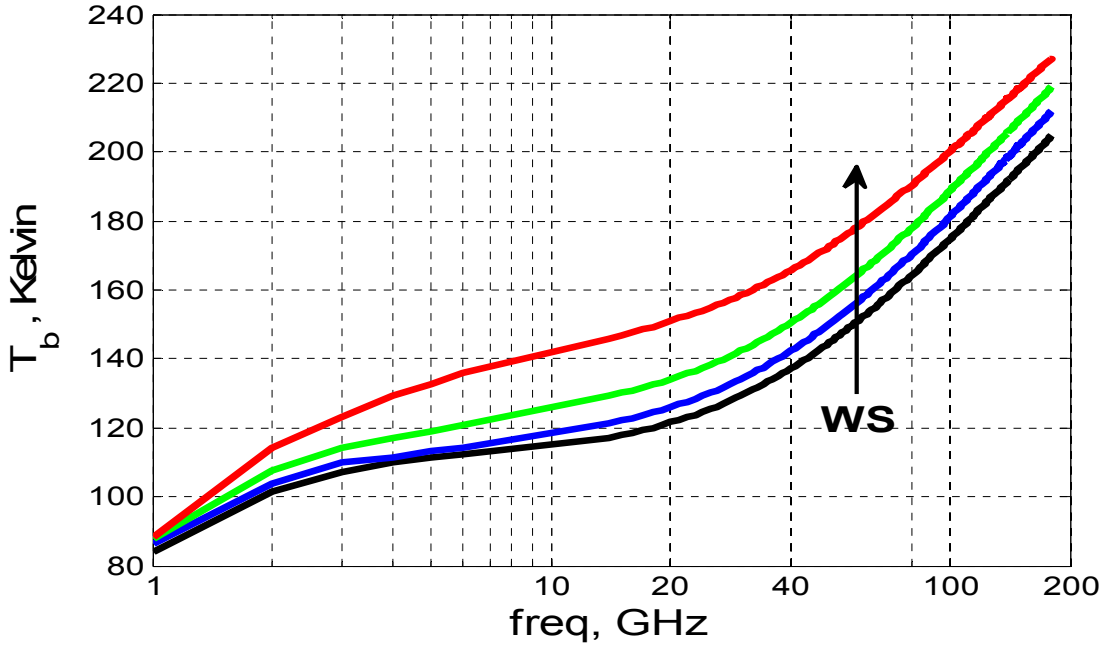

Figure 4.25 CFRSL horizontal emissivity for SST = 300 Kelvin, at 53 degrees and wind speeds of 6, 20, 30 and 40 m/s.

The following set of figures show the wind directional induced brightness temperature at (6, 20, and 40) m/s for nadir and off-nadir for both horizontal and vertical polarizations, respectively, at C-band. It is worth mentioning that beyond 40 m/s the model extrapolates to asymptotically approach a saturation point for wind speeds in excess of 100 m/s, the rate of change in magnitude of the wind direction for wind speeds > 40 m/s is very small and < 0.1 Kelvin. Further research is required to incorporate wind directional measurements for wind speeds > 40 m/s.

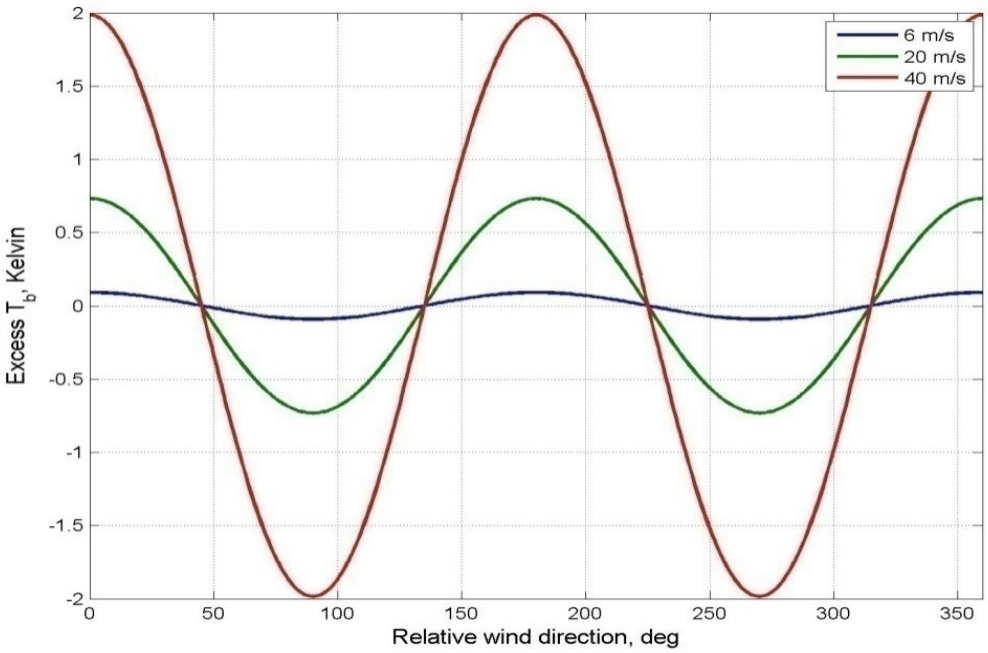

Figure 4.26 CFRSL excess emissivity for SST = 300 Kelvin, wind speeds of (6, 20 and 40) m/s at 4 GHz.

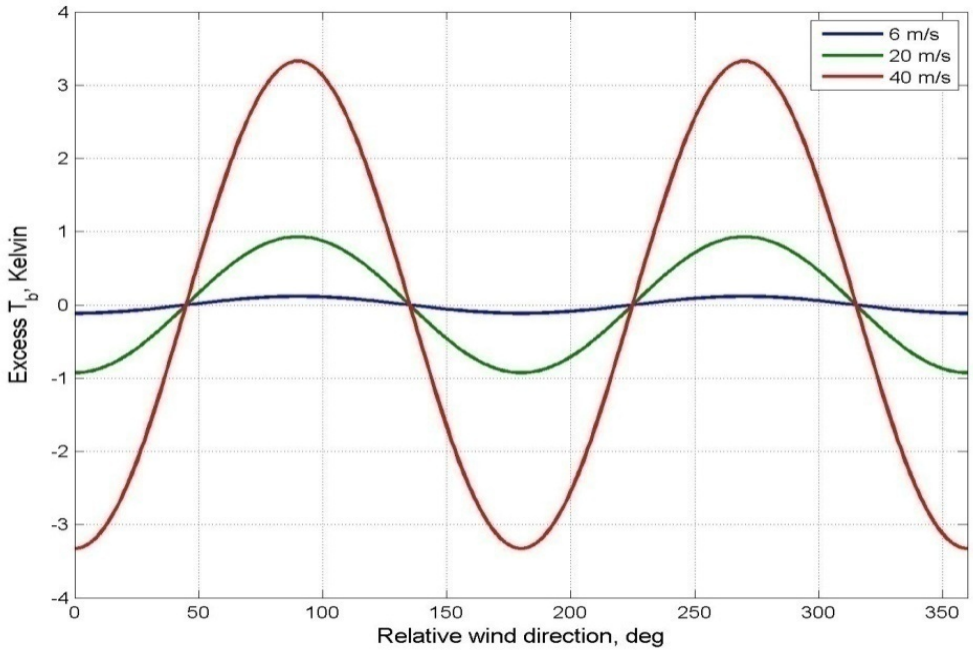

Figure 4.27 CFRSL excess emissivity for SST = 300 Kelvin, for wind speeds of (6, 20 and 40) m/s at 4 GHz.

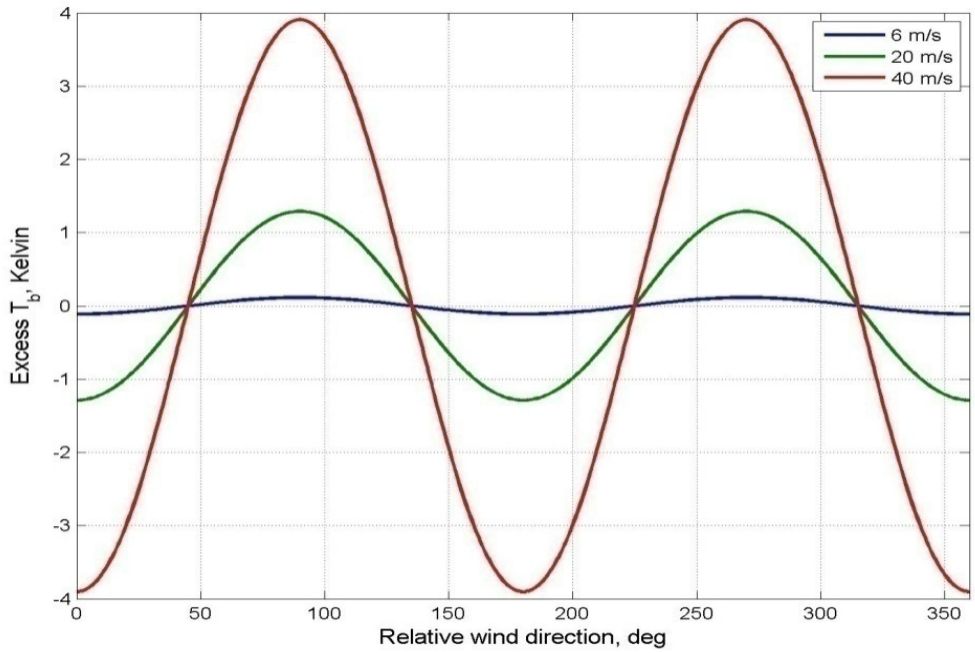

Figure 4.28 CFRSL excess emissivity for SST = 300 Kelvin, for wind speeds of (6, 20 and 40) m/s at 6.9 GHz.

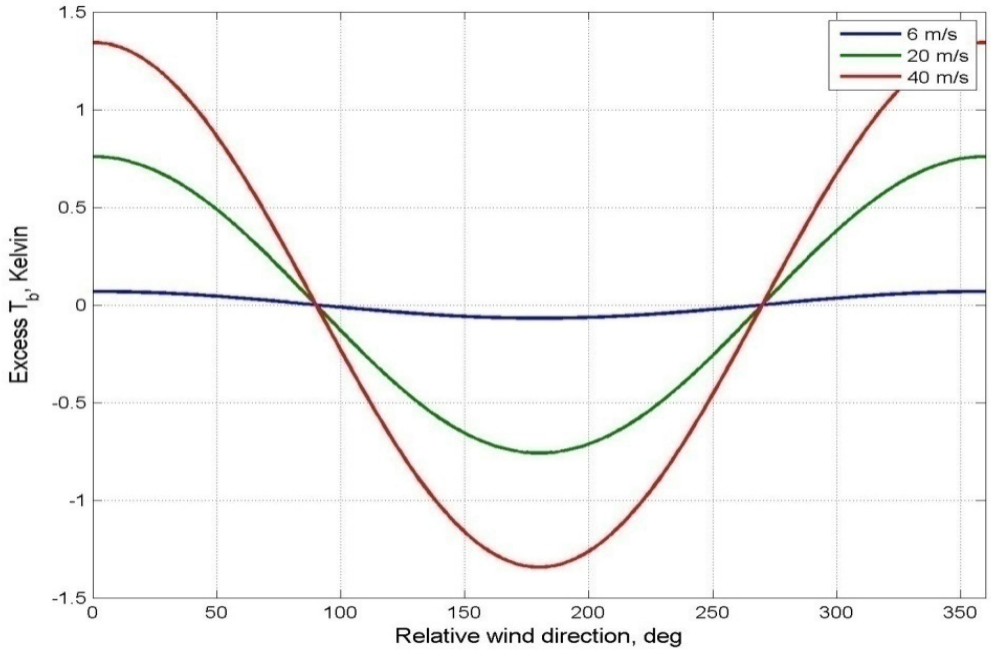

Figure 4.29 CFRSL excess emissivity for SST = 300 Kelvin, for wind speeds of (6, 20 and 40) m/s at 4 GHz.

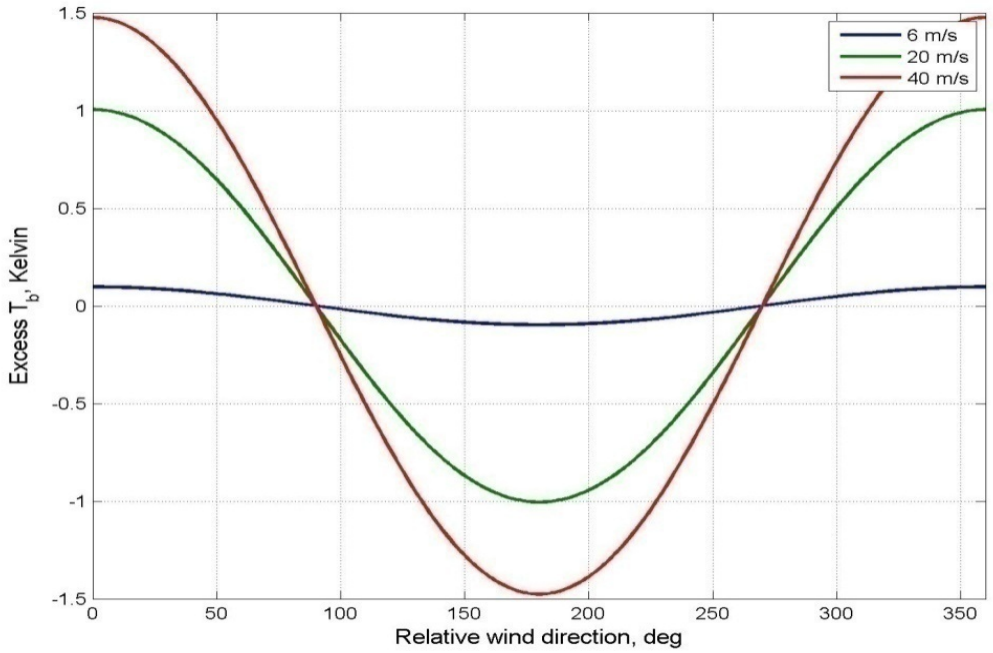

Figure 4.30 CFRSL excess emissivity for SST = 300 Kelvin, for wind speeds of (6, 20 and 40) m/s at 6.9 GHz.

CHAPTER 5 : CONCLUSION

5.1 Summary and Conclusion

Airborne hurricane surveillance provides crucial real time measurements that are vital to hurricane forecast warnings issued by the National Oceanic and Atmospheric Administration (NOAA) National Hurricane Center (NHC). For this purpose, NOAA and the U.S. Air Force (USAF) Reserve 53rd Weather Reconnaissance Squadron fly especially equipped "Hurricane Hunter" aircraft into storms of the Caribbean Sea and the Atlantic Ocean that threaten the continental United States. Currently these aircraft are equipped with a nadir looking radiometer known as the Stepped Frequency Microwave Radiometer, SFMR, which measures hurricane surface wind speeds and rain rates.

The Hurricane Imaging Radiometer, HIRAD, is an instrument concept that is envisioned as the next generation C-band microwave radiometer for hurricane surveillance [53] that is considered to be the replacement for SFMR. HIRAD is a synthetic aperture interferometric radiometer that provides a wide swath measurement of surface wind speed and rain rate from a high altitude aircraft. Current ocean surface emissivity models cannot meet the HIRAD requirements, therefore it was necessary to develop a C-band ocean emissivity model that accommodates a wide range of EIA and surface wind speeds up to hurricane force winds (Cat. 5). This was the principal motivation for this dissertation research.

As the work of this dissertation progressed, the idea of having a single unified emissivity model that covers a wider range of frequencies (rather than only C-band) became an attractive option. With additional effort to include other sources of ocean surface emissivity that were available in the open technical literature, it was possible to develop a unified model over a wider frequency range approximately 1 to > 100 GHz. Such a model would have application in a number of diverse radiometer system types (push brooms, conical scanners and cross-track scanners) and applications (instrument design, radiometric calibration and geophysical retrievals). Thus it was decided that the scope of this dissertation would be expanded to become this unified ocean surface emissivity model.

In this dissertation the CFRSL ocean surface emissivity model has been developed to calculate the ocean surface emissivity for a wide range of frequencies, wind speeds, and incidence angles. It is a physically realistic model that defines the relationship between the ocean surface emissivity, or brightness temperature, and the surface wind vector at 10 meters height. It relies on the increase of surface roughness and the generation of sea foam and bubble streaks on the surface with increasing wind speed. This model is a significant advancement to the state of the art by combining several models of lesser scope into a single unified model. It has a significant number of empirically derived coefficients that have been tuned to match published emissivity data where they exists, and the model architecture allows constrained monotonic extrapolation in frequency, EIA and wind speed to new regions where data do not presently exist. Because of its physics-based formulation, our model is adaptable to a range of instrument characteristics and measurement geometries, and we believe that our extrapolations to new

regions of parameter space are a reasonable approximation of the true ocean emission. As data become available, this model can be easily tuned to accommodate the new sources of measurements in these regions.

The CFRSL model is formulated with a foam-free term and a foam dependent term that are both wind speed and EIA dependent and frequency dispersive. The foam-free term accounts for surface roughness effects that monotonically increase with wind speed, and the sea foam term increases almost exponentially with wind speeds > 7 m/s and asymptotically approaches 100% foam cover at wind speeds well beyond 100 m/s. Further, the CFRSL ocean emissivity model also incorporates an anisotropic wind directional emissivity, which is available in the open literature. Our model extrapolates these peer-reviewed results in EIA, frequency and wind speeds.

While the CFRSL model is capable of calculating surface emissivity over a wide range of frequencies, wind speeds and EIA, unfortunately it has yet to be fully validated. The difficulty is the lack of independent emissivity measurements over parameter space (that were **NOT** used in the model tuning). However, there are several instances, where independent validation has been obtained. First, SFMR flight measurements made at 30 deg and 45 deg EIA during hurricanes Dolly and Gustav in the 2008 hurricane season (see Fig. 4.7 and Fig. 4.8) compare very favorably to the corresponding CFRSL results. Second, there is one occurrence of SFMR hurricane observations [54] as a function of wind direction, which compares well with our model. Third, a limited set of satellite comparisons are available with WindSat [37] that agree to

within 1-4 Kelvin for H-pol and 2-5 Kelvin for V-pol. These satellite results at 50 degrees EIA are encouraging considering the fact that WindSat measurements were averaged over its large footprint that reduced the peak wind speed and causes WindSat emissivities to be low compared to the CFRSL model (see Fig. 4.7 and Fig. 4.8). Finally, the CFRSL foam fraction dependence derived from the nadir SFMR T_b observations agrees well with numerous independent optical measurements of foam cover (see Fig. 4.1), which indicates that the CFRSL model has the same trend in comparison with peer-reviewed results.

5.2 Model Applicability

The original motivation for and principal application of the CFRSL emissivity model is for use in the HIRAD instrument development. It has been incorporated into a comprehensive end – to-end simulation of the HIRAD hurricane measurements by Amarin [55] and used in the evaluation of the geophysical (wind speed and rain rate) retrieval error estimates.

In a broader context, the CFRSL emissivity model has potential applicability in a number of satellite radiometry applications. For example, inter-satellite radiometric calibration techniques have been developed that require the use of an ocean radiative transfer model to normalize brightness temperatures between similar but not identical radiometers before inter-comparison. These include conical scanners and cross-track scanners that cover the frequency range from 6 GHz to 183 GHz and incidence angles from nadir to > 60 deg. The use of the CFRSL surface model would be an advantage in that it could accommodate all of the instrument

configurations, which has the potential to eliminate certain uncertainties introduced by using several different RTM's for inter-calibration. Further, most geophysical retrievals rely on RTM's for support and having a single unified model could be a definite advantage.

5.3 Future Work and Recommendations

Because there are many uncertainties that are associated with extrapolating the CFRSL emissivity model, there is a pressing need to validate this model over the full range of parameter space. It is recommended that extensive analysis of existing satellite microwave imagers and cross-track scanners be performed over the range of frequencies 6 - 183 GHz to validate the CRFSL model. Presently, we are conducting an emissivity model validation activity using independent data collected from WindSat measurements and collocated numerical weather model (GDAS) analyses. This dataset will be used to validate the CFRSL model and fine-tune its empirical coefficients for frequencies between 6.8 to 37 GHz at EIA's of 50 to 55 degs and wind speeds between 4 – 30 m/s. It is recommended that others in the microwave radiometer community perform their own independent evaluations.

Also, there is also a need to improve the knowledge of foam emissivity across all frequencies as a function of wind speed. This is especially important for C-band where recent circle flights in hurricanes have shown that there is a strong wind direction signal that exists at high wind speeds

[54]. Such improvements will lead to an improved unified total ocean emissivity model that could be available to interested users.

APPENDIX A. ROUGH EMISSIVITY MODEL

This appendix shows a Matlab subroutine (function) which computes the rough emissivity in the range of frequency between 4-7 GHz as a function of wind speed and incidence angle. It contains all the coefficients for the functional form shown in Eq. 3.16a.

```
%---------------------------------------------------------------
                              Matlab Code
              Usage: variablename=Filename(xValue,yValue)
          Example: result=func(5,10) where "func" is the file name
                          given while saving the .m file
               xValue & yValue are the single set of values or
                              array names.
%---------------------------------------------------------------
function [za]=g_ws_EIA_fix_4_7_eqn409(xa,ya)
%---------------------------------------------------------------
%   X= WS
%   Y= EIA
%   Z= G(WS,EIA), H-Pol
%   Eqn= Chebyshev X,Y Bivariate Polynomial Order 10
%   r2=0.9997749573730617
%   r2adj=0.9997712909170316
%   StdErr=0.05566631094396879
%   Fstat=276945.0107085867
  [rowx colx]=size(xa);
  if(rowx~=1 & colx~=1)
    error('x must be scalar or 1D array');
    return;
  end
  [rowy coly]=size(ya);
  if(rowy~=1 & coly~=1)
    error('y must be scalar or 1D array');
    return;
  end
  c=[
    6.099819238317017,
    5.309057855821564,
    2.174747926850547,
    -0.7963977493285743,
    1.476399176062425,
    0.1162406319502817,
    -0.2913562464620839,
    -1.315473728033350,
    -0.003084044920483652,
    -0.04880245646317465,
    0.2152753417460734,
    0.0003684208895205712,
    -0.3534173578783878,
```

```
-0.01433053585585735,
-0.02101899986104839,
-0.01747034090306732,
0.3615499482449378,
0.1230083891755488,
-0.04109409512445508,
0.009154316259444349,
-0.006063720462762434,
-0.07913845370454646,
-0.2034989724150650,
0.1079129328425777,
0.04693447293410319,
0.003133547959526183,
0.005823774892592893,
-0.001380526392073879,
0.09270869346136754,
0.03678422461351521,
-0.1198851659515575,
0.01267370787251389,
0.007370800692676593,
0.001691449295857653,
0.001778273914013807,
-0.0002902768647382242,
-0.07949981815910359,
0.01839122603218115,
0.05061633902750617,
-0.04158925107839948,
-0.001464768289729144,
-0.001057594123380018,
0.0004409685029354500,
0.0003678109164081555,
-4.177334132002115E-05,
0.05331444289650395,
-0.01471507749042444,
-0.003904545422102304,
0.02717382458687180,
-0.007608380603219743,
-0.001589158998989952,
-0.001097456270841817,
1.269747869074145E-06,
9.449266426174246E-05,
2.242515433496379E-06,
-0.04606261661946276,
0.0003834944489842436,
-0.001646531874136751,
-0.007319246065922135,
0.009982147126280992,
-0.0003904189469627936,
2.941753298340733E-05,
-0.0003962329197702733,
-1.608894765695398E-05,
1.645440848682135E-06,
3.927938605304365E-06,
];
```

```
  lenx=length(xa);
  leny=length(ya);
  for(j=1:leny)
    for(i=1:lenx)
      x=xa(i);
      y=ya(j);
      z=evalcpoly(65,0,0,x,y,c,...
        35.00000000000000,35.00000000000000,...
        0.000000000000000,0.000000000000000,...
        28.50000000000000,28.50000000000000,...
        0.000000000000000,0.000000000000000);
       za(i,j)=z;
       end
     end
%-----------------------------------------------------------------
function z=evalcpoly(order,logx,logy,x,y,p,s0,s1,s2,s3,s4,s5,s6,s7)
%-----------------------------------------------------------------
  tx=[];
  ty=[];
  v=[];
  if(logx==0)
    x=(x-s0)/s1;
  else
    x=(log(x)-s2)/s3;
  end
  if(logy==0)
    y=(y-s4)/s5;
  else
    y=(log(y)-s6)/s7;
  end
  if (order==5)
    tcnt=3;
  elseif (order==9)
    tcnt=4;
  elseif (order==14)
    tcnt=5;
  elseif (order==20)
    tcnt=6;
  elseif (order==27)
    tcnt=7;
  elseif (order==35)
    tcnt=8;
  elseif (order==44)
    tcnt=9;
  elseif (order==54)
    tcnt=10;
  elseif (order==65)
    tcnt=11;
  else
    return;
  end
  if(tcnt>6)
    if(x<-1.0)
      x=-1.0;
```

```
  end
  if(x>1.0)
    x= 1.0;
  end
  if(y<-1.0)
    y=-1.0;
  end
  if(y>1.0)
    y= 1.0;
  end
end
tx(1)=1.0;
ty(1)=1.0;
tx(2)=x;
ty(2)=y;
for j=2:1:tcnt-1
  tx(j+1)=2*x*tx(j)-tx(j-1);
  ty(j+1)=2*y*ty(j)-ty(j-1);
end
iv=1;
for j=1:1:tcnt
  for m=j:-1:1
    v(iv)=tx(m)*ty(j-m+1);
    iv=iv+1;
    end
  end
z=0.0;
for j=1:1:order+1
  z = z + p(j)*v(j);
end
return;
```

APPENDIX B. FOAM EMISSIVITY MODEL

This appendix shows a Matlab subroutine (function) which computes the foam emissivity for frequencies > 7 GHz as a function of frequency and incidence angle. It contains all the coefficients for the functional form shown in Eq. 3.17b.

```
%---------------------------------------------------------------
                              Matlab Code
              Usage: variablename=Filename(xValue,yValue)
        Example: result=func(5,10) where "func" is the file name
                          given while saving the .m file
            xValue & yValue are the single set of values or
                              array names.
%---------------------------------------------------------------
function [za]=fomfix_Emis_Vpol_eqn1409(xa,ya)
%---------------------------------------------------------------
%   X= freq
%   Y= EIA
%   Z= emis, Vpol
%   r2=0.9999998529546301
%   r2adj=0.9999998501788463
%   StdErr=9.409849816263255E-05
%   Fstat=369917998.0537065
  [rowx colx]=size(xa);
  if(rowx~=1 & colx~=1)
    error('x must be scalar or 1D array');
    return;
  end
  [rowy coly]=size(ya);
  if(rowy~=1 & coly~=1)
    error('y must be scalar or 1D array');
    return;
  end
  c=[
    0.8366781279670424,
    0.4923754393154391,
    0.008765269653834105,
    0.6633606867582748,
    -0.008707383013974312,
    -0.3190732013131856,
    -0.001996043792726086,
    -0.2901280515131776,
    0.001955584892509356,
    0.1828665105558679,
    -7.148270518407371E-06,
```

```
    0.04942985402633750,
    2.105384531001938E-05,
    -0.09419910907382063,
    8.609648925659489E-07,
    0.04435276145049907,
    -2.329331789066672E-06,
    0.04293773009137337,
    -3.784142208184952E-10,
    -0.06413327758809961,
    -1.661401198268504E-08,
    -0.009691458983531767,
    2.032428694802292E-08,
    0.05926695280201098,
    1.529114517733671E-08,
    -0.008584960388077224,
    1.074436090076842E-10,
    -0.04535940797124195,
    -1.100321489697625E-10,
    0.01470419382536589,
    8.012088683911149E-09,
    0.02972598123497492,
    5.499469274809064E-09,
    -0.01894468557059641,
    3.357802219085900E-11,
    -0.02270893786015087,
    -2.971287773406000E-11,
    -0.0004108745889316654,
    2.364655481774802E-10,
    ];
  lenx=length(xa);
  leny=length(ya);
  for(j=1:leny)
    for(i=1:lenx)
      x=xa(i);
      y=ya(j);
      z=evalcratl(38,0,0,x,y,c,...
        12.50000000000000,12.50000000000000,...
        0.000000000000000,0.000000000000000,...
        40.00000000000000,40.00000000000000,...
        0.000000000000000,0.000000000000000,...
        0.4884888657915565,0.4884888657915565);
       za(i,j)=z;
       end
     end
%-----------------------------------------------------------------
function z = evalcratl(order, logx, logy, x, y, p,...
  s0, s1, s2, s3, s4, s5, s6, s7, s8, s9)
%-----------------------------------------------------------------
  tx=[];
  ty=[];
  if(logx==0)
    x=(x-s0)/s1;
  else
    x=(log(x)-s2)/s3;
```

```
end
if(logy==0)
  y=(y-s4)/s5;
else
  y=(log(y)-s6)/s7;
end
if (order==6)
  tcnt=3;
elseif (order==10)
  tcnt=4;
elseif (order==14)
  tcnt=5;
elseif (order==18)
  tcnt=6;
elseif (order==22)
  tcnt=7;
elseif (order==26)
  tcnt=8;
elseif (order==30)
  tcnt=9;
elseif (order==34)
  tcnt=10;
elseif (order==38)
  tcnt=11;
elseif (order==42)
  tcnt=12;
else
  return;
end
if(tcnt>7)
  if(x<-1.0)
    x=-1.0;
  end
  if(x>1.0)
    x= 1.0;
  end
  if(y<-1.0)
    y=-1.0;
  end
  if(y>1.0)
    y= 1.0;
  end
end
tx(1)=1.0;
ty(1)=1.0;
tx(2)=x;
ty(2)=y;
for j=2:1:tcnt-1
  tx(j+1)=2*x*tx(j)-tx(j-1);
  ty(j+1)=2*y*ty(j)-ty(j-1);
end
m=2;
num=p(1);
den=1.0+p(2)*tx(m)+p(3)*ty(m);
```

```
for(j=3:4:order-1)
  num=num+p(j+1)*tx(m);
  num=num+p(j+2)*ty(m);
  m=m+1;
  den=den+p(j+3)*tx(m);
  den=den+p(j+4)*ty(m);
end
if (den==0)
  z=0;
else
  z=(num/den)*s8+s9;
end
return;
```

APPENDIX C. ROUGH EMISSIVITY MODEL

This appendix shows a Matlab subroutine (function) which computes the rough emissivity for frequencies < 2 or > 7 GHz as a function of wind speed and incidence angle. It contains all the coefficients for the functional form shown in Eqs. 3.18 a and b for both vertical and horizontal polarizations.

For Vertical polarization:

```
%-----------------------------------------------------------------
                                Matlab Code
                Usage: variablename=Filename(xValue,yValue)
          Example: result=func(5,10) where "func" is the file name
                              given while saving the .m file
                  xValue & yValue are the single set of values or
                                array names.
%-----------------------------------------------------------------
function [za]=G_Vpol_eqn2132_we(xa,ya)
%-----------------------------------------------------------------
%   X= EIA
%   Y= WS
%   Z= G(WS,EIA), V-Pol, 6 m/s & nadir weighted
%   Eqn= z=a+EXVCUMX(b,c,d)+EXVCUMY(e,f,g)+EXVCUMX(h,c,d)*EXVCUMY(1,f,g)
%   r2=0.9840811617660178
%   r2adj=0.983410894893008
%   StdErr=0.1664831292870609
%   Fstat=1686.766145822205
  [rowx colx]=size(xa);
  if(rowx~=1 & colx~=1)
    error('x must be scalar or 1D array');
    return;
  end
  [rowy coly]=size(ya);
  if(rowy~=1 & coly~=1)
    error('y must be scalar or 1D array');
    return;
  end
  lenx=length(xa);
  leny=length(ya);
  for(j=1:leny)
    for(i=1:lenx)
      x=xa(i);
      y=ya(j);
      z1=exp(-exp(-(x-53.25670680171918)/4.800510427783687));
      z2=exp(-exp(-(y-9.255211268934141)/3.829082843131137));
```

```
 z=0.4489778618429879-0.9995666300248580*z1+...
   3.704109473086860*z2-1.388563083910300*z1*z2;
  za(i,j)=z;
  end
end
```

For Horizontal polarization:

```
%--------------------------------------------------------------
                                Matlab Code
                Usage: variablename=Filename(xValue,yValue)
          Example: result=func(5,10) where "func" is the file name
                       given while saving the .m file
              xValue & yValue are the single set of values or
                                array names.
%--------------------------------------------------------------
function [za]=G_Hpol_eqn2095_we(xa,ya)
%--------------------------------------------------------------
%   X= EIA
%   Y= WS
%   Z= G(WS,EIA), H-Pol 6m/s & Nadir weighted
%   Eqn= z=LORCUMX(a,b,c)+LORCUMY(d,e,f)+LORCUMX(g,b,c)*LORCUMY(1,e,f)
%   r2=0.9949150167025811
%   r2adj=0.9947286560581731
%   StdErr=0.197163657584802
%   Fstat=6261.039352999082
  [rowx colx]=size(xa);
  if(rowx~=1 & colx~=1)
    error('x must be scalar or 1D array');
    return;
  end
  [rowy coly]=size(ya);
  if(rowy~=1 & coly~=1)
    error('y must be scalar or 1D array');
    return;
  end
  lenx=length(xa);
  leny=length(ya);
  for(j=1:leny)
    for(i=1:lenx)
      x=xa(i);
      y=ya(j);
      z1=0.5+atan(((x-67.07436265956480)/...
        29.24325818636037))/3.14159265358979323846;
      z2=0.5+atan(((y-11.85065714763983)/...
        10.98500629610563))/3.14159265358979323846;
      z=-14.44816121570469*z1+0.6658212838417320*z2+...
        61.27914900598514*z1*z2;
       za(i,j)=z;
       end
     end
```

APPENDIX D. WIND DIRECTIONAL EMISSIVITY MODEL AT 53º

This appendix shows a Matlab subroutine (function) which computes the wind induced emissivity for incidence angle 53 deg as a function of wind speed and frequency. It contains all the coefficients for the functional form shown in Eqs. 3.20 for both vertical and horizontal polarizations.

For Vertical Polarization:

```
%--------------------------------------------------------------------
                                Matlab Code
                Usage: variablename=Filename(xValue,yValue)
           Example: result=func(5,10) where "func" is the file name
                           given while saving the .m file
                xValue & yValue are the single set of values or
                                array names.
%--------------------------------------------------------------------
function [za]=a1V_53_eqn1125(xa,ya)
%--------------------------------------------------------------------
%   X= WS, m/s
%   Y= Freq, GHz
%   Eqn= z=(a+bx+cx^2+dx^3+elny+f(lny)^2)/(1+gx+hx^2+ilny+j(lny)^2)
%   r2=0.9998505006310699
%   r2adj=0.9998022750281892
%   StdErr=0.007196410484698329
%   Fstat=23779.52514238048
  [rowx colx]=size(xa);
  if(rowx~=1 & colx~=1)
    error('x must be scalar or 1D array');
    return;
  end
  [rowy coly]=size(ya);
  if(rowy~=1 & coly~=1)
    error('y must be scalar or 1D array');
    return;
  end
  lenx=length(xa);
  leny=length(ya);
  for(j=1:leny)
    for(i=1:lenx)
      x=xa(i);
      y=ya(j);
      y=log(y);
```

```
 z1=0.008600491282434296+x*(-0.001311619129798619+...
   x*(0.0009177321915749557+x*9.349367017907678E-06));
 z2=y*(-0.007172526030905561+...
   y*0.001481529513901506);
 z3=1.000000000000000+x*(-0.01991208026522926+...
   x*0.001124284066671228);
 z4=y*(-0.4431129282895224+...
   y*0.05853216785014886);
 z=(z1+z2)/(z3+z4);
  za(i,j)=z;
  end
end
```

For Horizontal Polarization:

```
%--------------------------------------------------------------------
                                Matlab Code
                 Usage: variablename=Filename(xValue,yValue)
           Example: result=func(5,10) where "func" is the file name
                              given while saving the .m file
                  xValue & yValue are the single set of values or
                                array names.
%--------------------------------------------------------------------
function [za]=a2H_53_eqn1125(xa,ya)
%--------------------------------------------------------------------
%   X= WS, m/s
%   Y= freq, GHz
%   Eqn= z=(a+bx+cx^2+dx^3+elny+f(lny)^2)/(1+gx+hx^2+ilny+j(lny)^2)
%   r2=0.9980627584274587
%   r2adj=0.9974378417911551
%   StdErr=0.02674447733262829
%   Fstat=1831.814697670744
  [rowx colx]=size(xa);
  if(rowx~=1 & colx~=1)
    error('x must be scalar or 1D array');
    return;
  end
  [rowy coly]=size(ya);
  if(rowy~=1 & coly~=1)
    error('y must be scalar or 1D array');
    return;
  end
  lenx=length(xa);
  leny=length(ya);
  for(j=1:leny)
    for(i=1:lenx)
      x=xa(i);
      y=ya(j);
      y=log(y);
      z1=-0.1106570115758933+x*(-0.0002645154397625481+...
        x*(-6.480581701960926E-05+x*-5.065422360100543E-05));
      z2=y*(0.07563751235451605+...
        y*-0.01252895590313455);
      z3=1.000000000000000+x*(-0.005149550647175991+...
        x*0.0005150493762855036);
      z4=y*(-0.5399159833066225+...
        y*0.07688869194664198);
      z=(z1+z2)/(z3+z4);
       za(i,j)=z;
       end
     end
```

APPENDIX E. CFRSL EMISSIVITY MODEL PARAMETRIC PLOTS WITH RESPECT TO EIA

In remote sensing the frequency range < 37 GHz is used mostly for observing ocean surface geophysical parameters like wind speed, sea surface temperature and salinity. Frequencies such as (10.7, 18.7, 23.5 and 36.5 GHz) are common among the majority of the spaceborne and airborne remote sensing sensors.

This appendix presents the extrapolated CFRSL surface emissivity model scaled to 300 Kelvin with respect to Earth Incidence Angles (EIA) up to 80 degrees for 10.7, 18.7, 23.5 and 36.5 GHz frequencies.

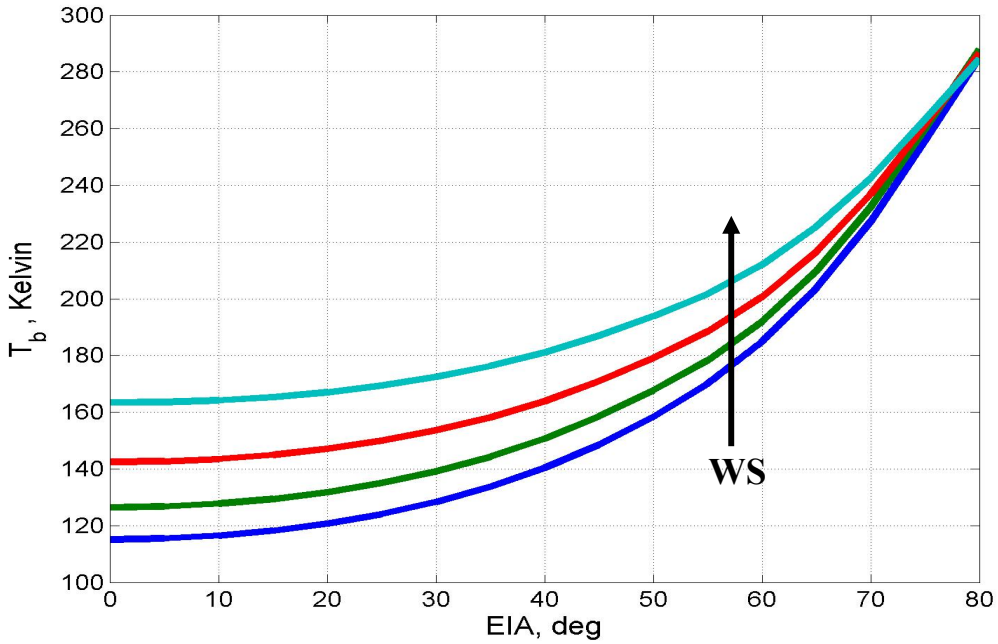

Figure. E.1 CFRSL vertical emissivity for SST = 300 Kelvin, at 10.7 GHz and wind speeds of 6, 20, 30 and 40 m/s.

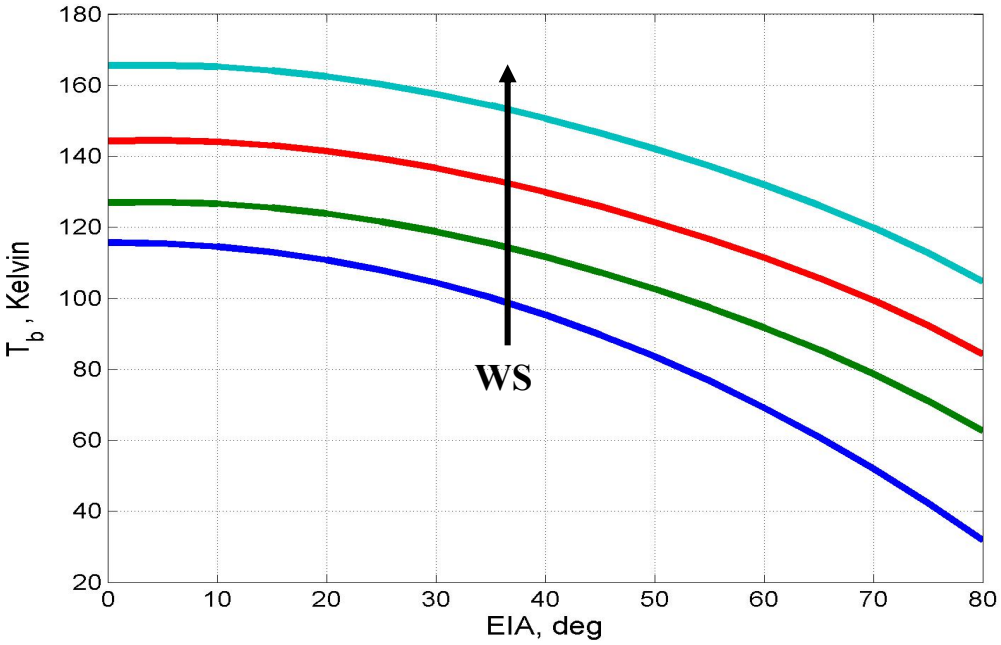

Figure. E.2 CFRSL horizontal emissivity for SST = 300 Kelvin, at 10.7 GHz and wind speeds of 6, 20, 30 and 40 m/s.

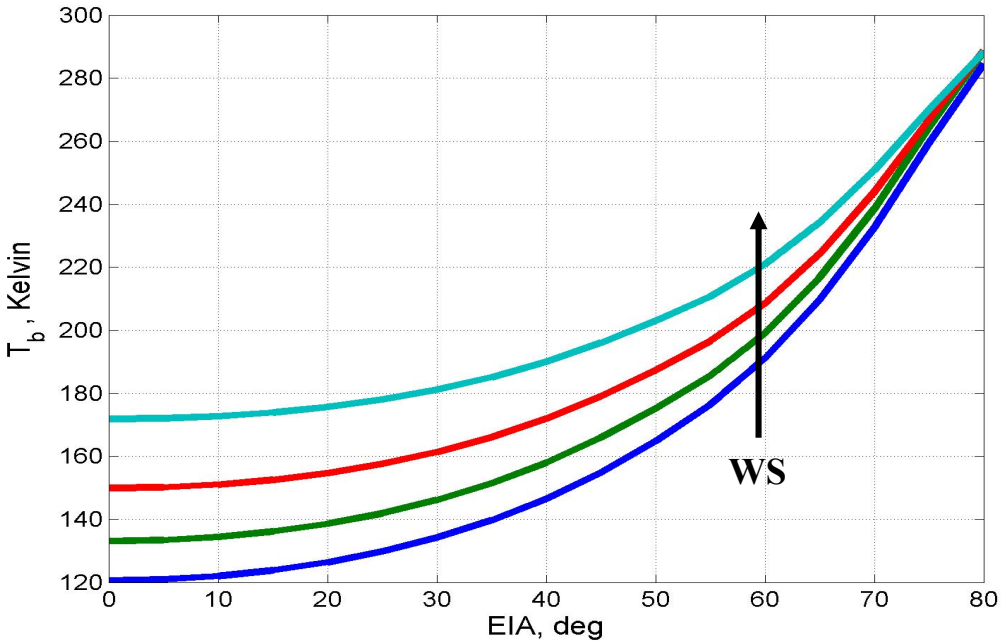

Figure. E.3 CFRSL vertical emissivity for SST = 300 Kelvin, at 18.7 GHz and wind speeds of 6, 20, 30 and 40 m/s.

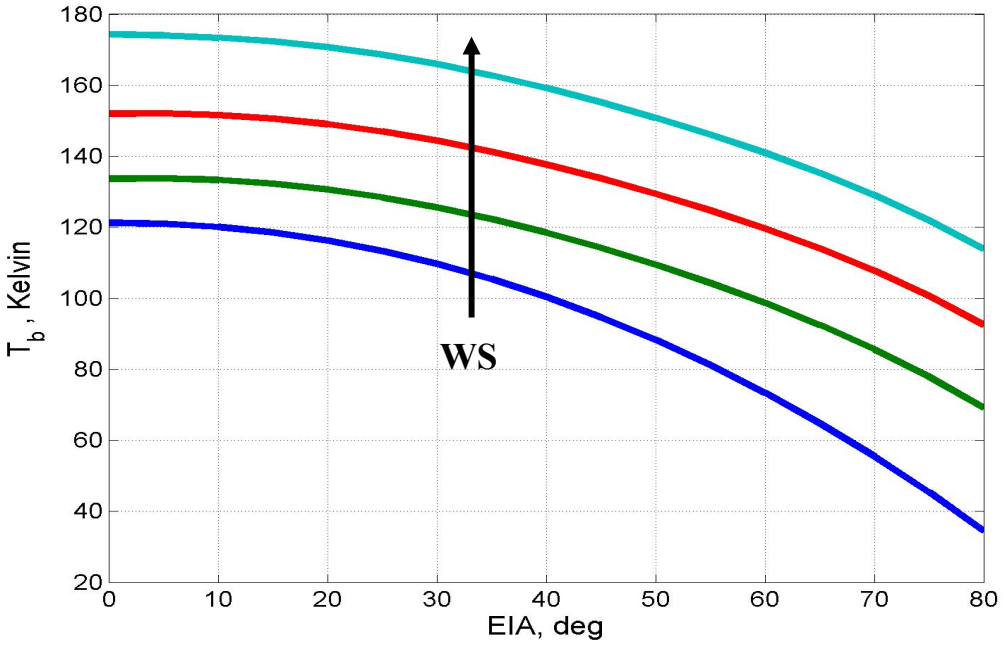

Figure. E.4 CFRSL horizontal emissivity for SST = 300 Kelvin, at 18.7 GHz and wind speeds of 6, 20, 30 and 40 m/s.

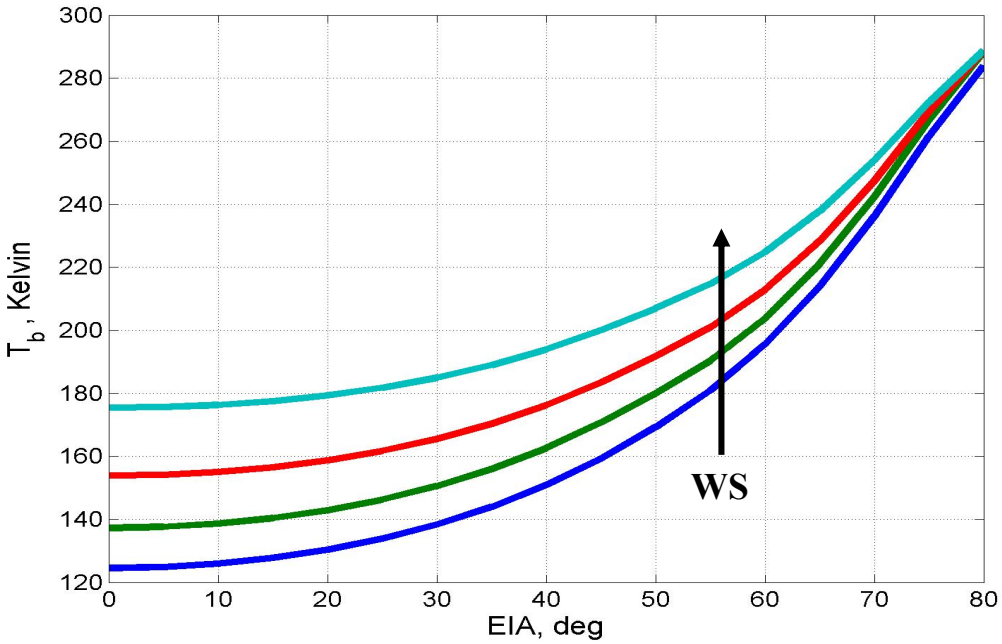

Figure. E.5 CFRSL vertical emissivity for SST = 300 Kelvin, at 23.5 GHz and wind speeds of 6, 20, 30 and 40 m/s.

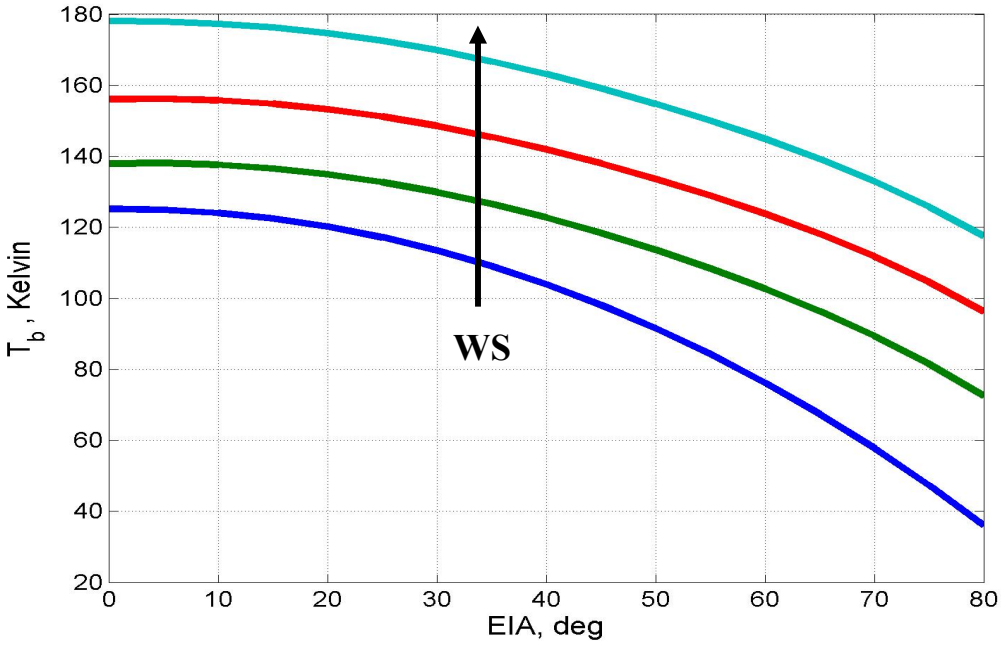

Figure. E.6 CFRSL Horizontal emissivity for SST = 300 Kelvin, at 23.8 GHz and wind speeds of 6, 20, 30 and 40 m/s.

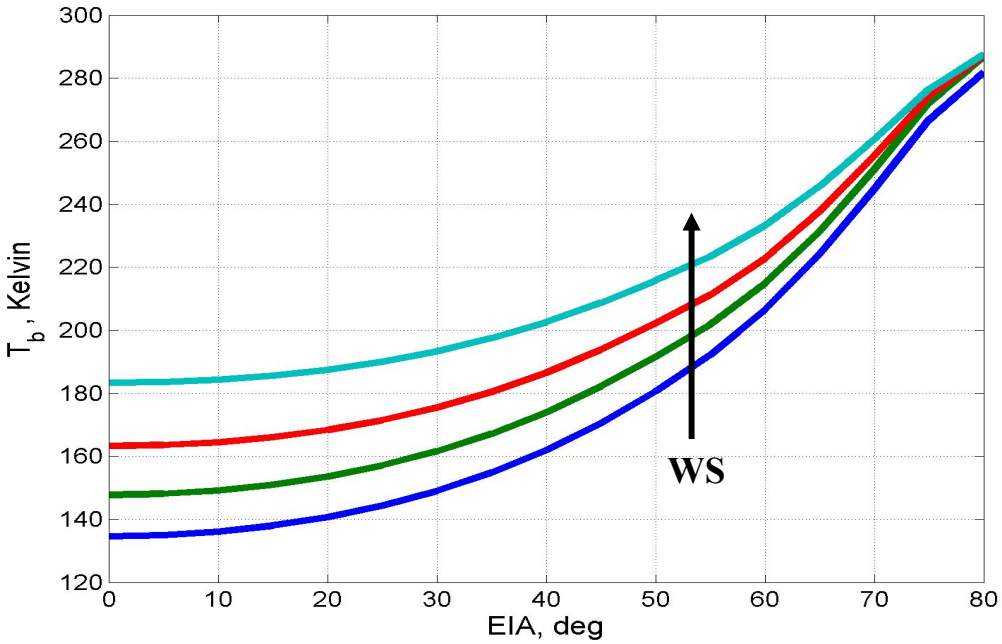

Figure. E.7 CFRSL vertical emissivity for SST = 300 Kelvin, at 36.5 GHz and wind speeds of 6, 20, 30 and 40 m/s.

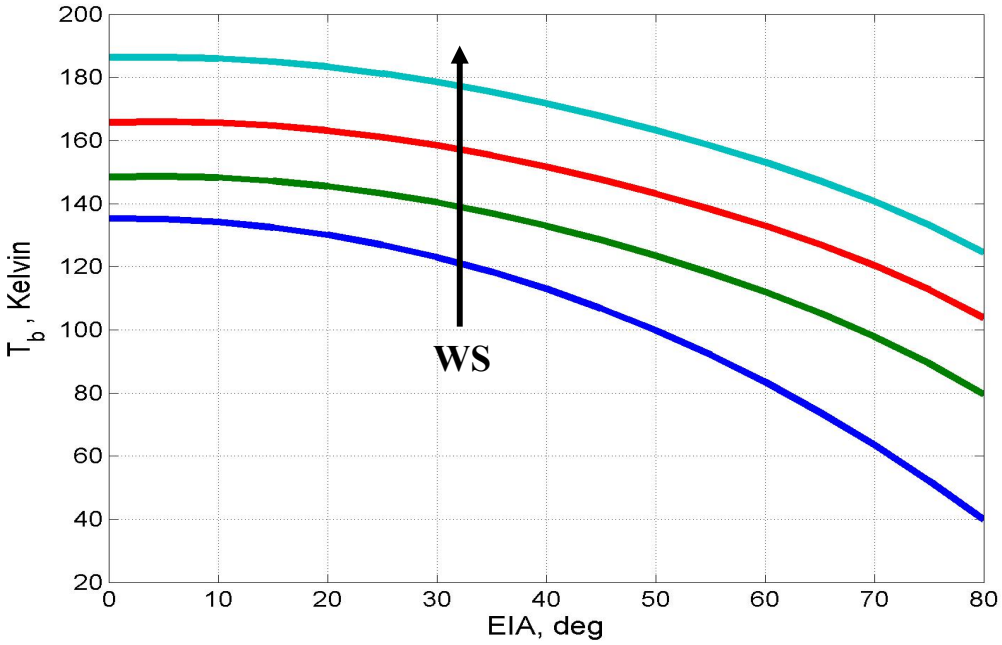

Figure. E.8 CFRSL horizontal emissivity for SST = 300 Kelvin, at 36.5 GHz and wind speeds of 6, 20, 30 and 40 m/s.

APPENDIX F. CFRSL EMISSIVITY MODEL PARAMETRIC PLOTS WITH RESPECT TO WS

In remote sensing the frequency range < 37 GHz is used mostly for observing ocean surface geophysical parameters like wind speed, sea surface temperature and salinity. Frequencies such as (10.7, 18.7, 23.5 and 36.5 GHz) are common among the majority of the spaceborne and airborne remote sensing sensors.

This appendix presents the extrapolated CFRSL surface emissivity model scaled to 300 Kelvin with respect to Wind Speed (*ws*) for 10.7, 18.7, 23.5 and 36.5 GHz frequencies.

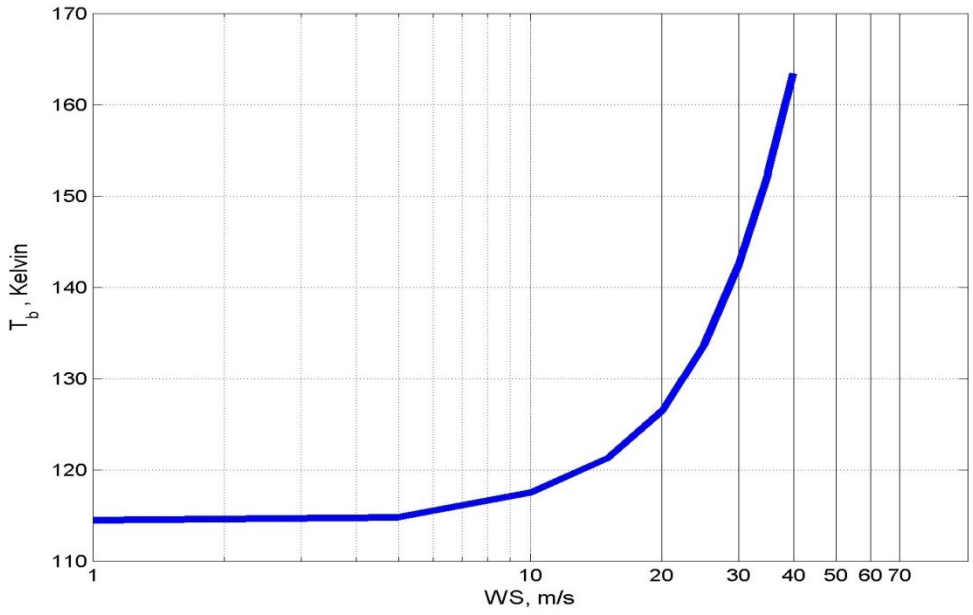

Figure. F.1 CFRSL emissivity for SST = 300 Kelvin, at 10.7 GHz frequency and Nadir incidence angle.

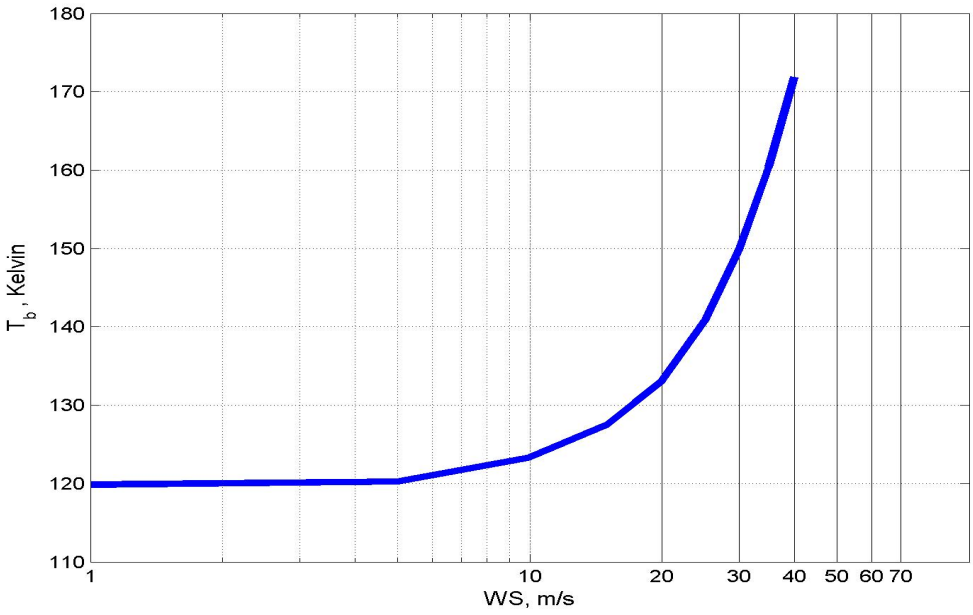

Figure. F.2 CFRSL emissivity for SST = 300 Kelvin, at 18.7 GHz frequency and Nadir incidence angle.

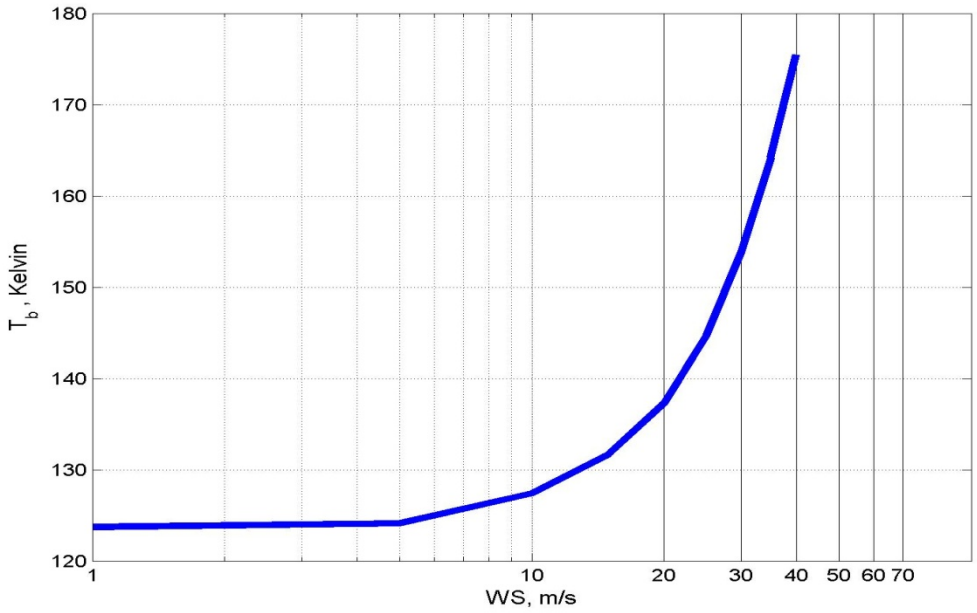

Figure. F.3 CFRSL emissivity for SST = 300 Kelvin, at 23.8 GHz frequency and Nadir incidence angle.

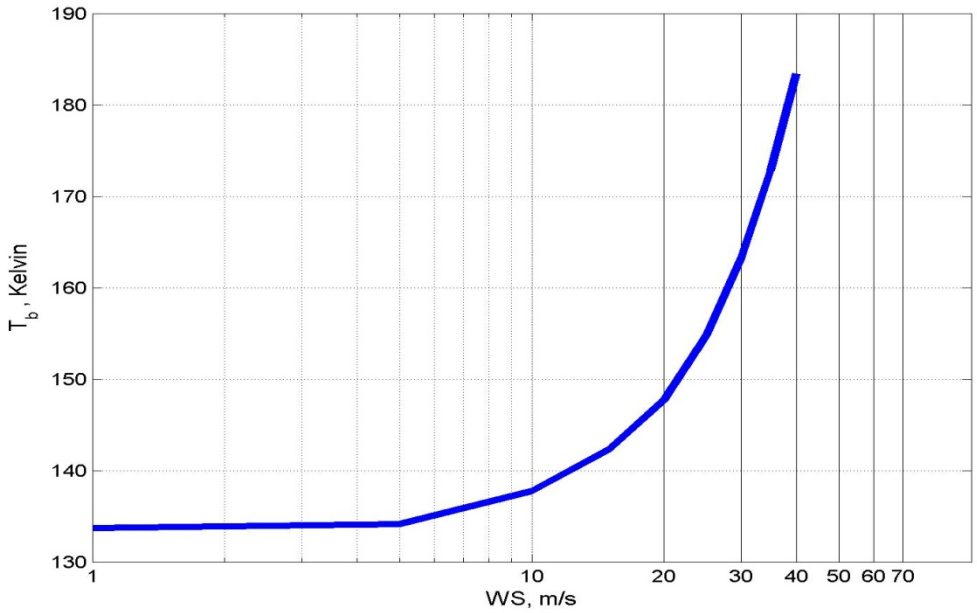

Figure. F.4 CFRSL emissivity for SST = 300 Kelvin, at 36.5 GHz frequency and Nadir incidence angle.

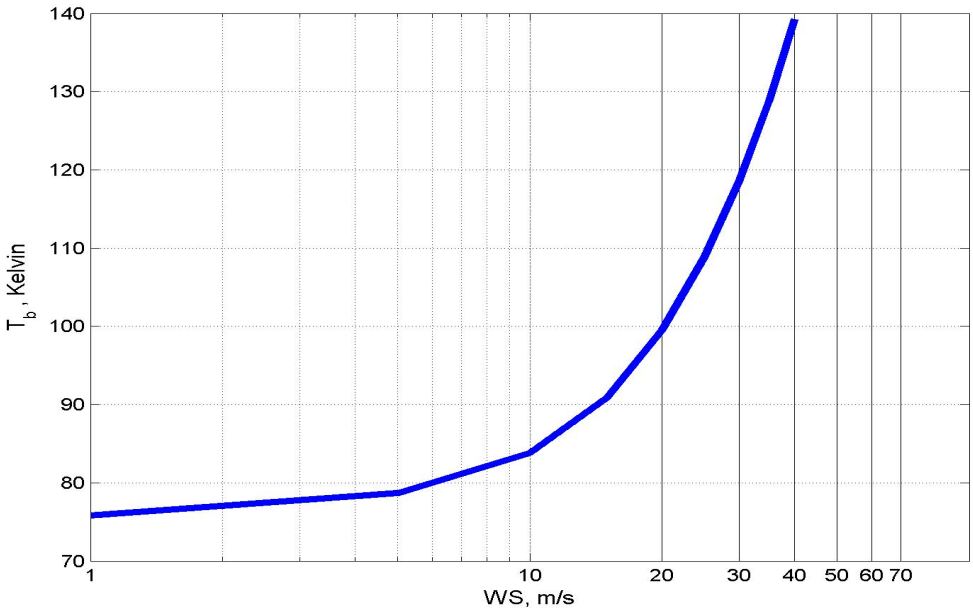

Figure. F.5 CFRSL horizontal emissivity for SST = 300 Kelvin, at 10.7 GHz frequency and 53 degrees incidence angle.

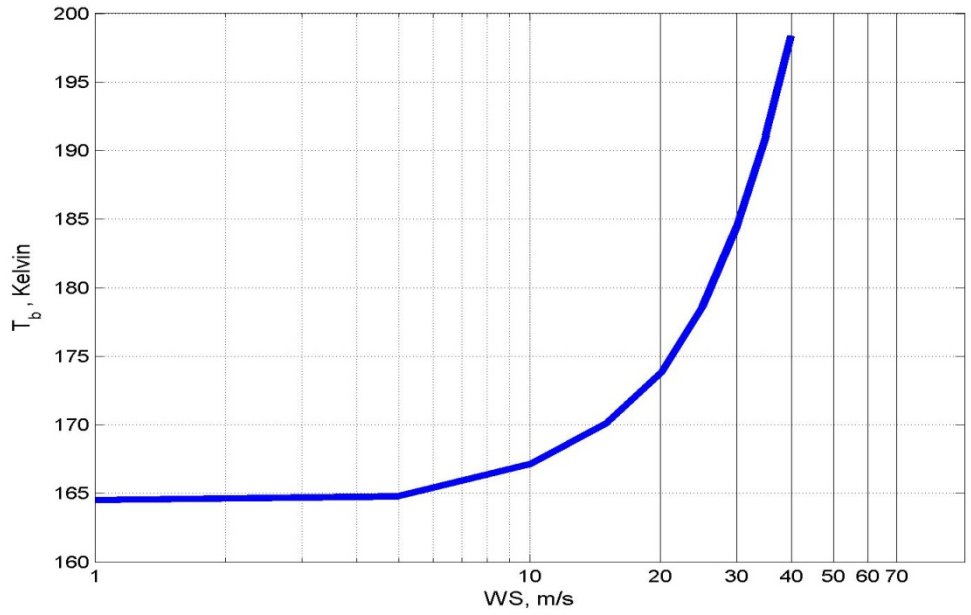

Figure. F.6 CFRSL vertical emissivity for SST = 300 Kelvin, at 10.7 GHz frequency and 53 degrees incidence angle.

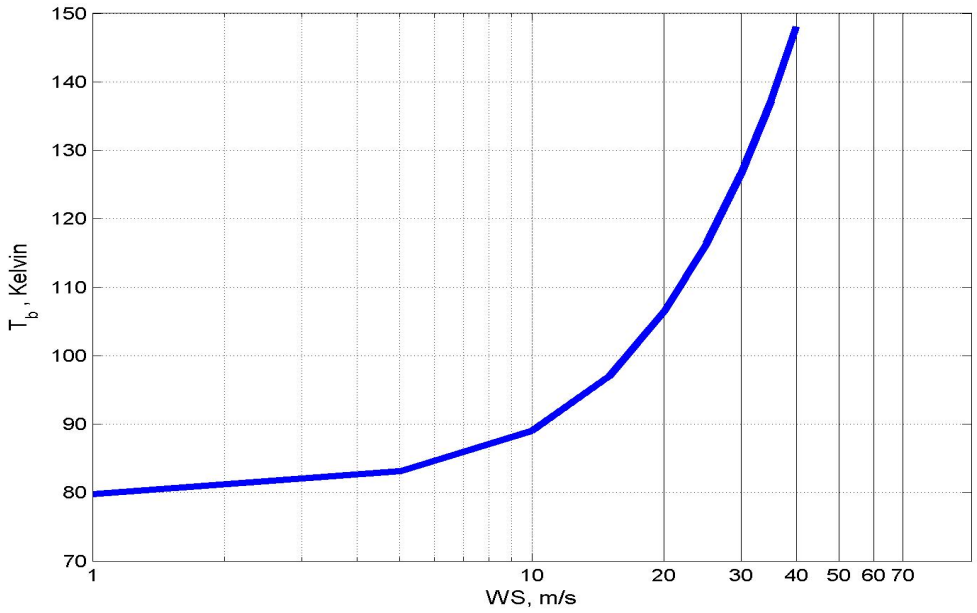

Figure. F.7 CFRSL horizontal emissivity for SST = 300 Kelvin, at 18.7 GHz frequency and 53 degrees incidence angle.

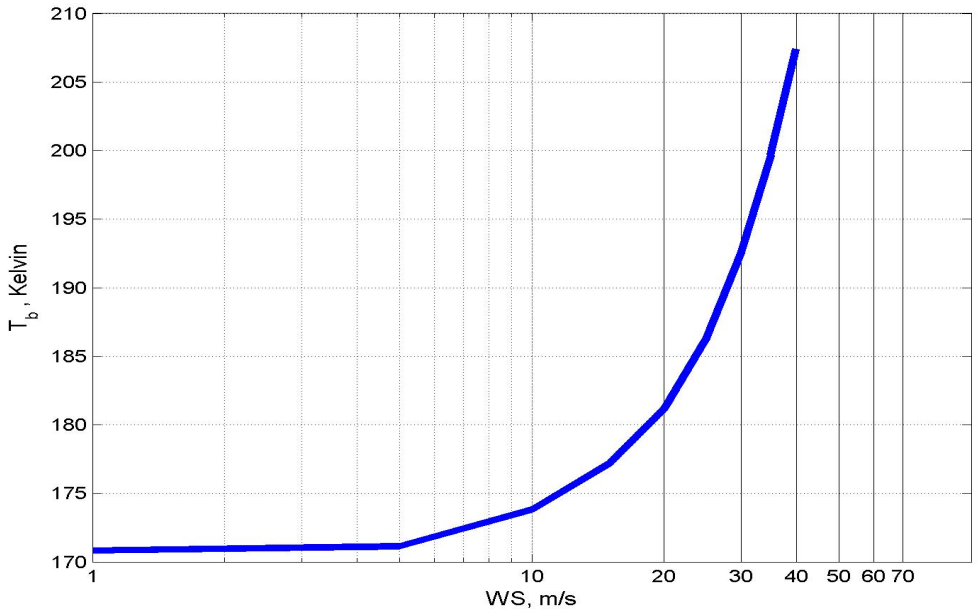

Figure. F.8 CFRSL vertical emissivity for SST = 300 Kelvin, at 18.7 GHz frequency and 53 degrees incidence angle.

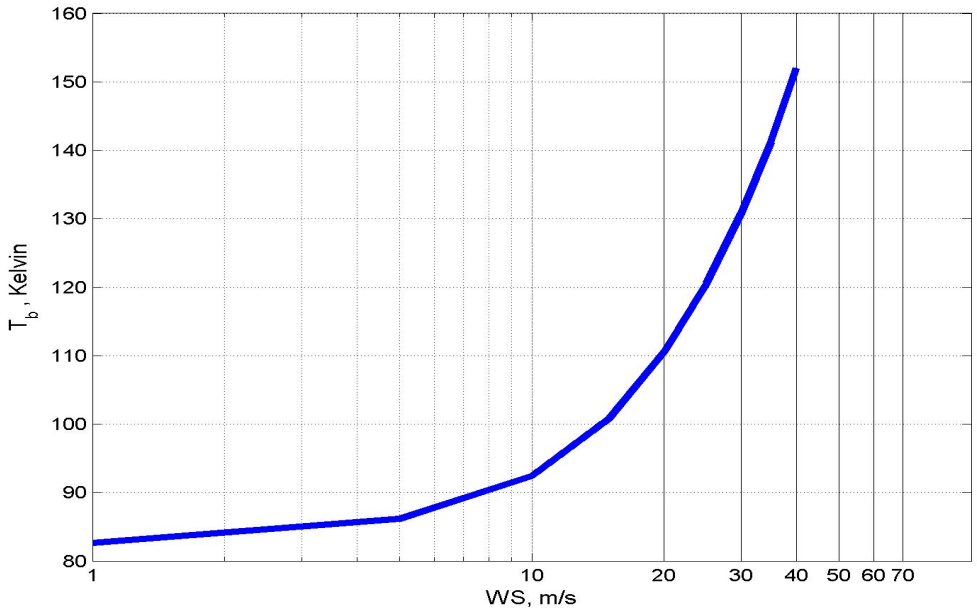

Figure. F.9 CFRSL horizontal emissivity for SST = 300 Kelvin, at 23.8 GHz frequency and 53 degrees incidence angle.

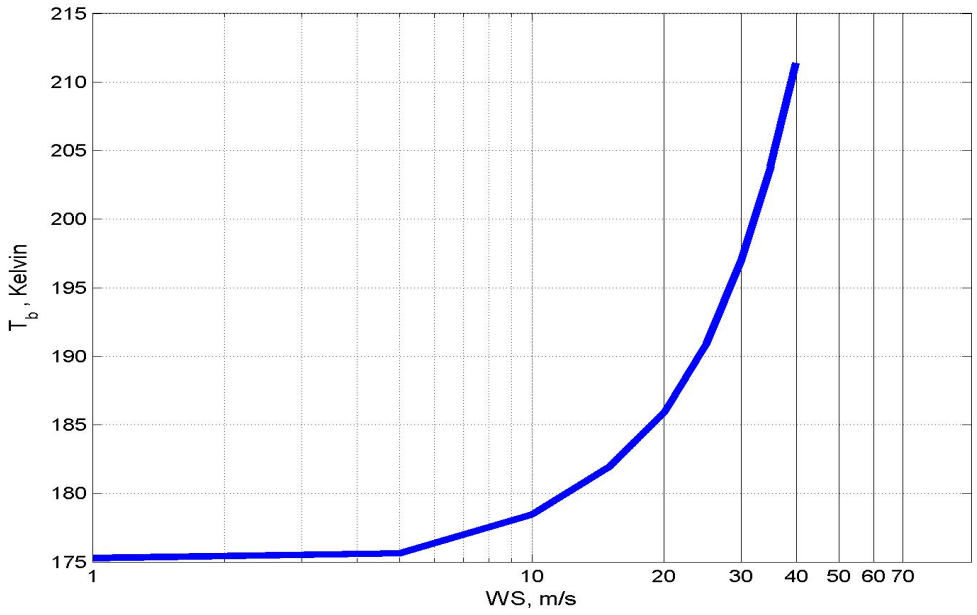

Figure. F.10 CFRSL vertical emissivity for SST = 300 Kelvin, at 23.8 GHz frequency and 53 degrees incidence angle.

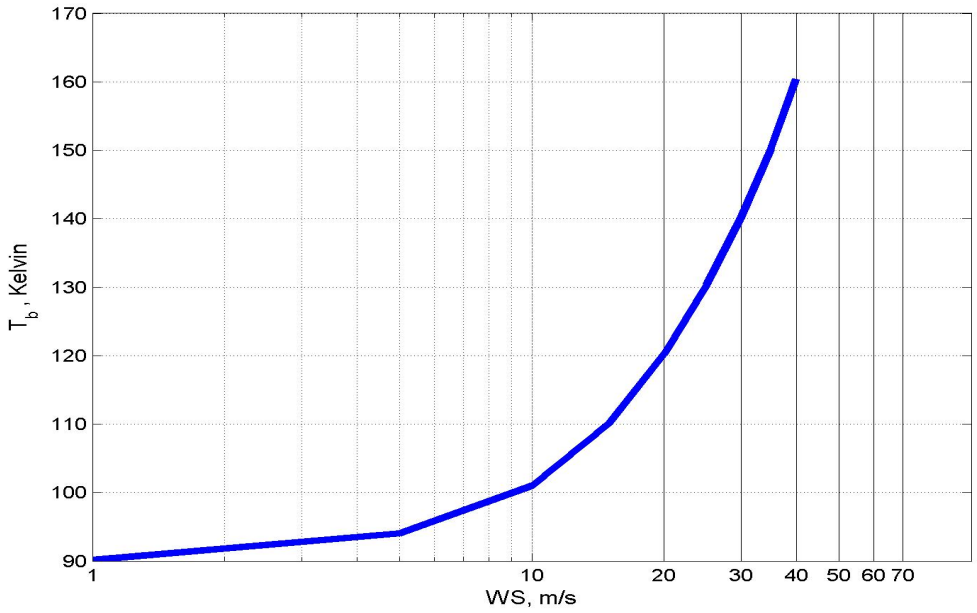

Figure. F.11 CFRSL horizontal emissivity for SST = 300 Kelvin, at 36.5 GHz frequency and 53 degrees incidence angle.

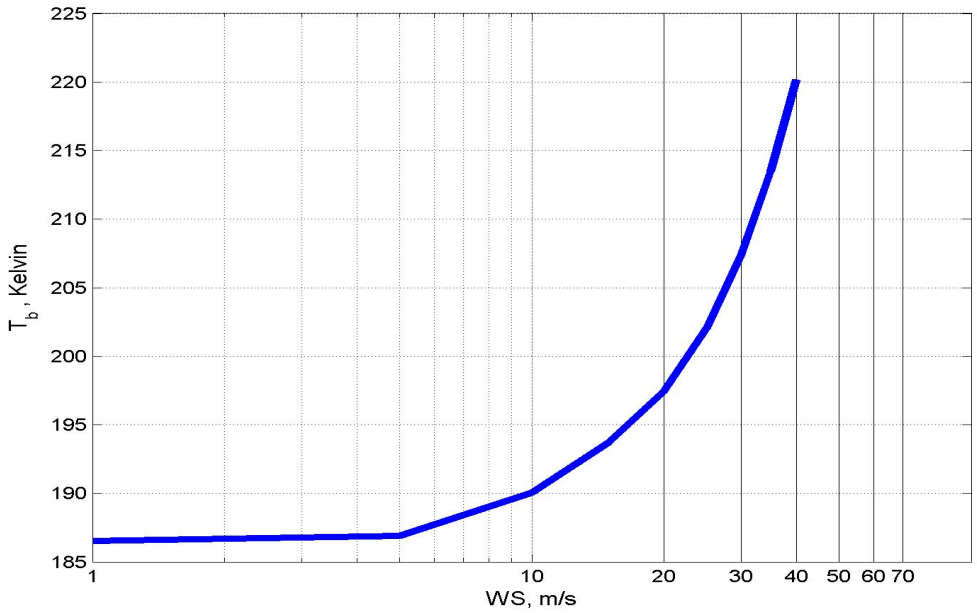

Figure. F.12 CFRSL vertical emissivity for SST = 300 Kelvin, at 36.5 GHz frequency and 53 degrees incidence angle.

APPENDIX G. CFRSL WIND DIRECTION EXCESS EMISSIVITY MODEL

In remote sensing the frequency range < 37 GHz is used mostly for observing ocean surface geophysical parameters like wind speed, sea surface temperature and salinity. Frequencies such as (10.7, 18.7, 23.5 and 36.5 GHz) are common among the majority of the spaceborne and airborne remote sensing sensors.

This appendix presents the extrapolated CFRSL excess wind directional emissivity model scaled to 300 Kelvin with respect to Relative wind direction for wind speeds 6, 20, and 40 m/s at 10.7, 18.7, 23.5 and 36.5 GHz frequencies.

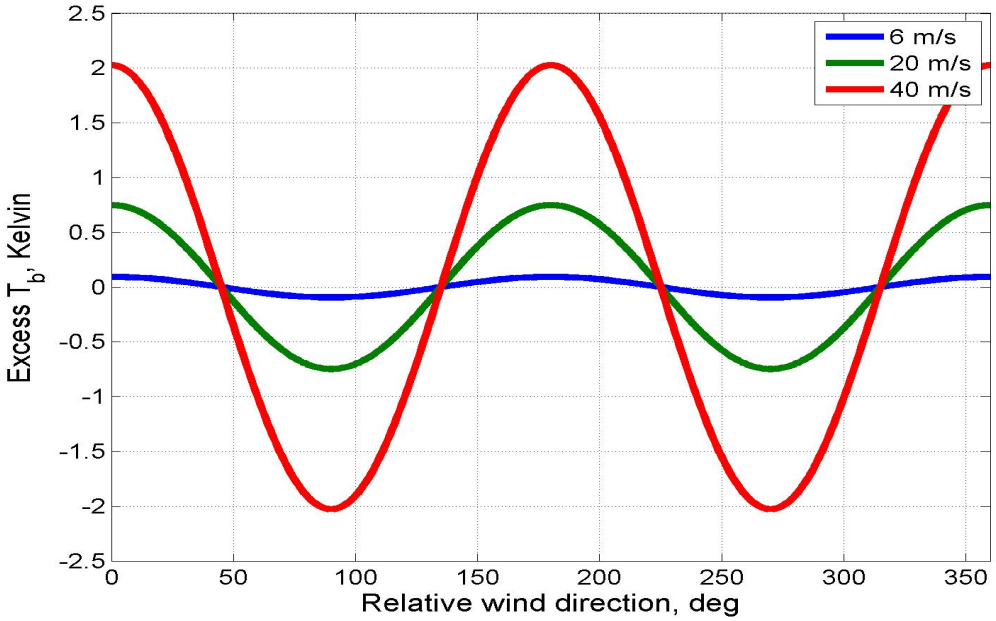

Figure. G.1 CFRSL excess emissivity for SST = 300 Kelvin, and wind speeds of (6, 20 and 40) m/s at 18.7 GHz and nadir incidence angle.

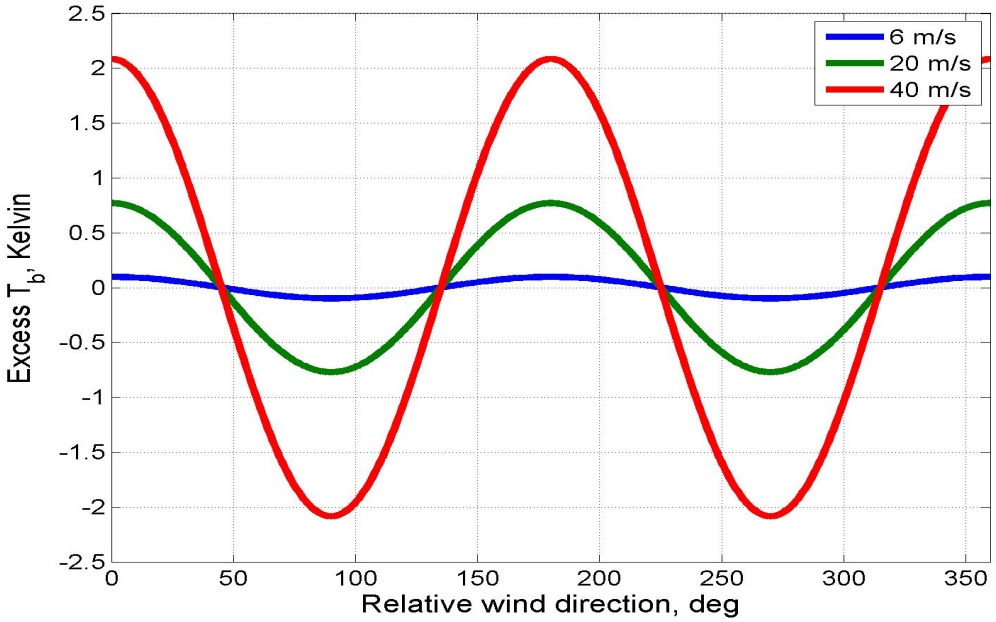

Figure. G.2 CFRSL excess emissivity for SST = 300 Kelvin, and wind speeds of (6, 20 and 40) m/s at 23.8 GHz and nadir incidence angle.

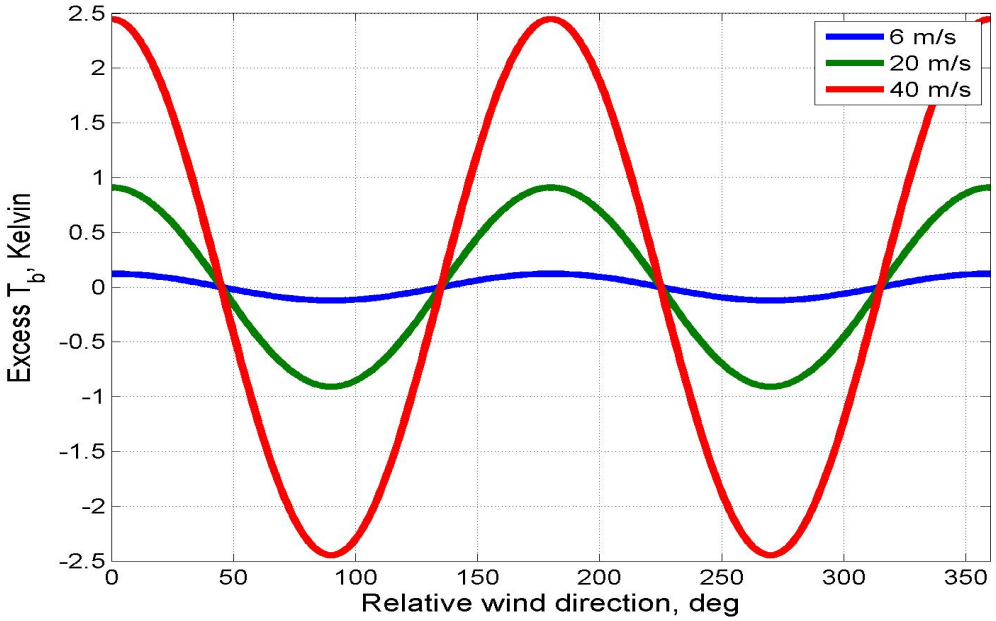

Figure. G.3 CFRSL excess emissivity for SST = 300 Kelvin, and wind speeds of (6, 20 and 40) m/s at 36.5 GHz and nadir incidence angle.

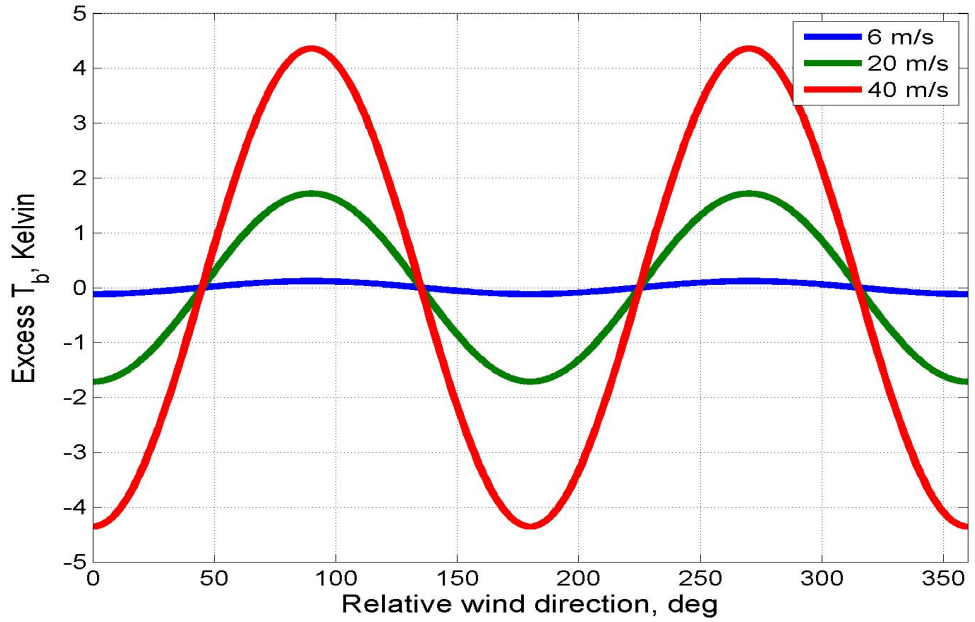

Figure. G.4 CFRSL horizontal excess emissivity for SST = 300 Kelvin, and wind speeds of (6, 20 and 40) m/s at 10.7 GHz and 53 degrees incidence angle.

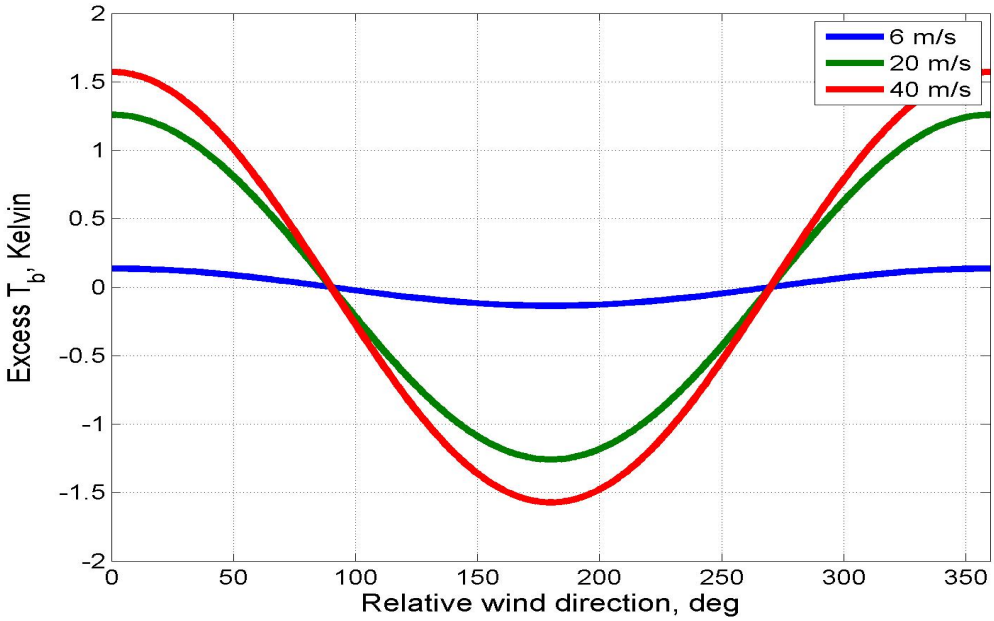

Figure. G.5 CFRSL vertical excess emissivity for SST = 300 Kelvin, and wind speeds of (6, 20 and 40) m/s at 10.7 GHz and 53 degrees incidence angle.

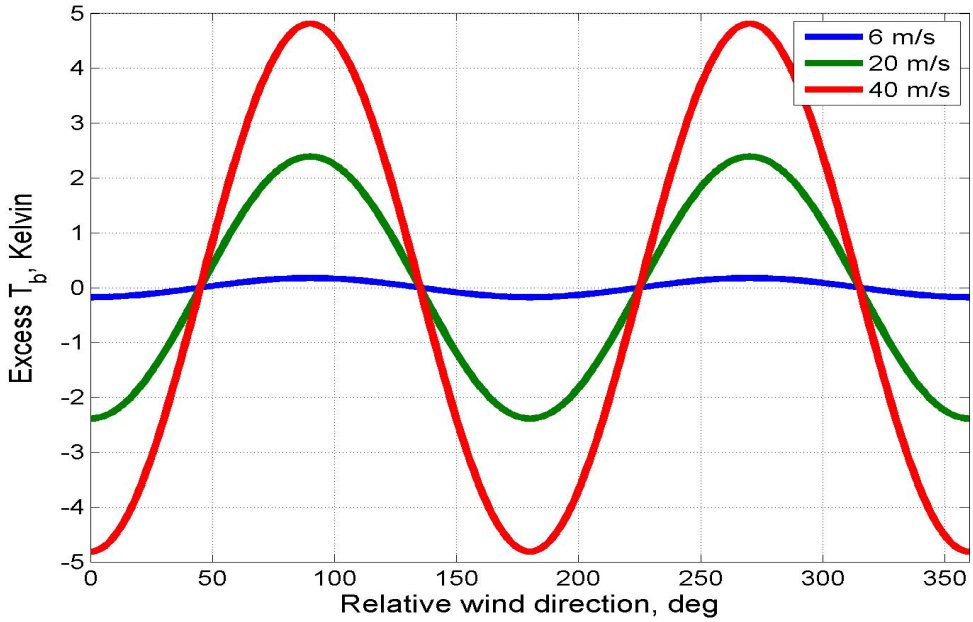

Figure. G.6 CFRSL horizontal excess emissivity for SST = 300 Kelvin, and wind speeds of (6, 20 and 40) m/s at 18.7 GHz and 53 degrees incidence angle.

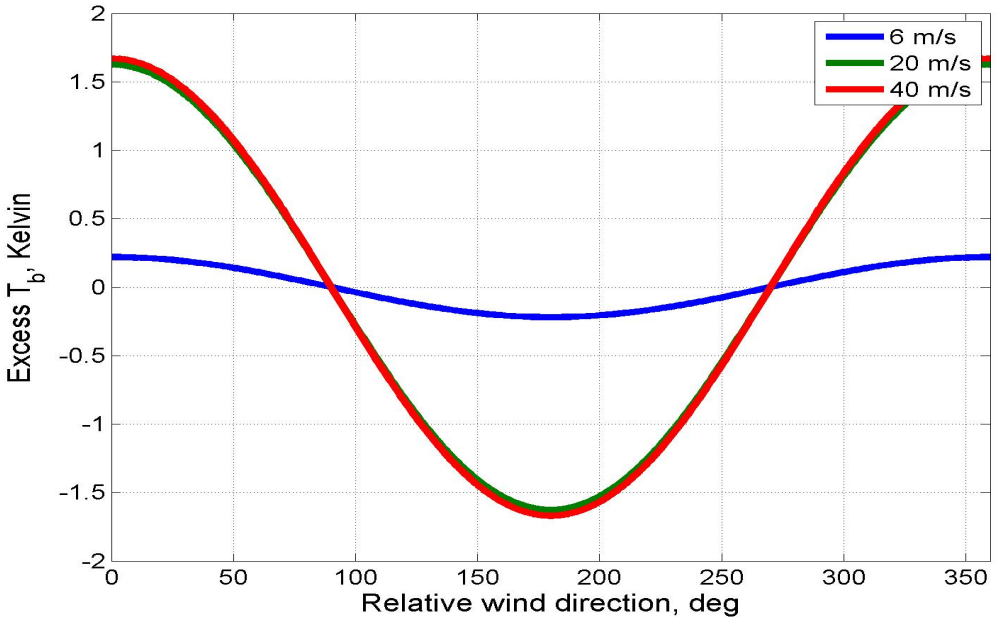

Figure. G.7 CFRSL vertical excess emissivity for SST = 300 Kelvin, and wind speeds of (6, 20 and 40) m/s at 18.7 GHz and 53 degrees incidence angle.

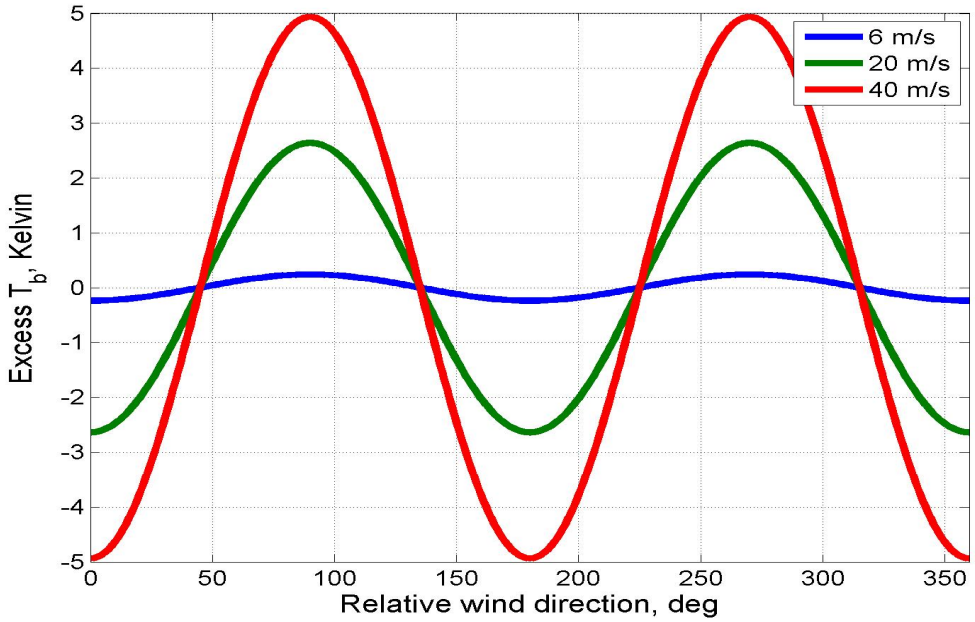

Figure. G.8 CFRSL horizontal excess emissivity for SST = 300 Kelvin, and wind speeds of (6, 20 and 40) m/s at 36.5 GHz and 53 degrees incidence angle.

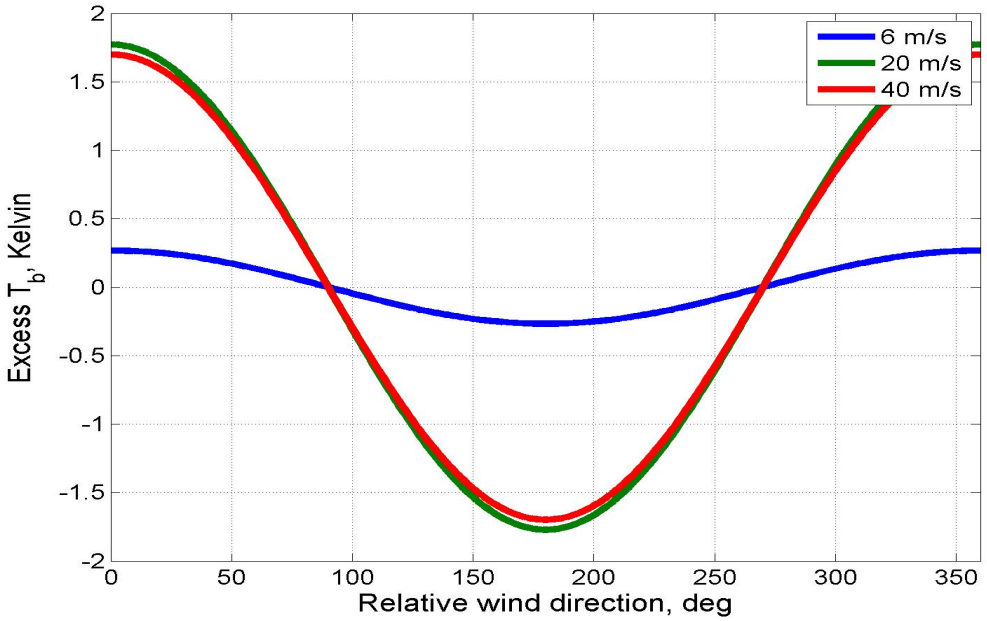

Figure. G.9 CFRSL vertical excess emissivity for SST = 300 Kelvin, and wind speeds of (6, 20 and 40) m/s at 23.8 GHz and 53 degrees incidence angle.

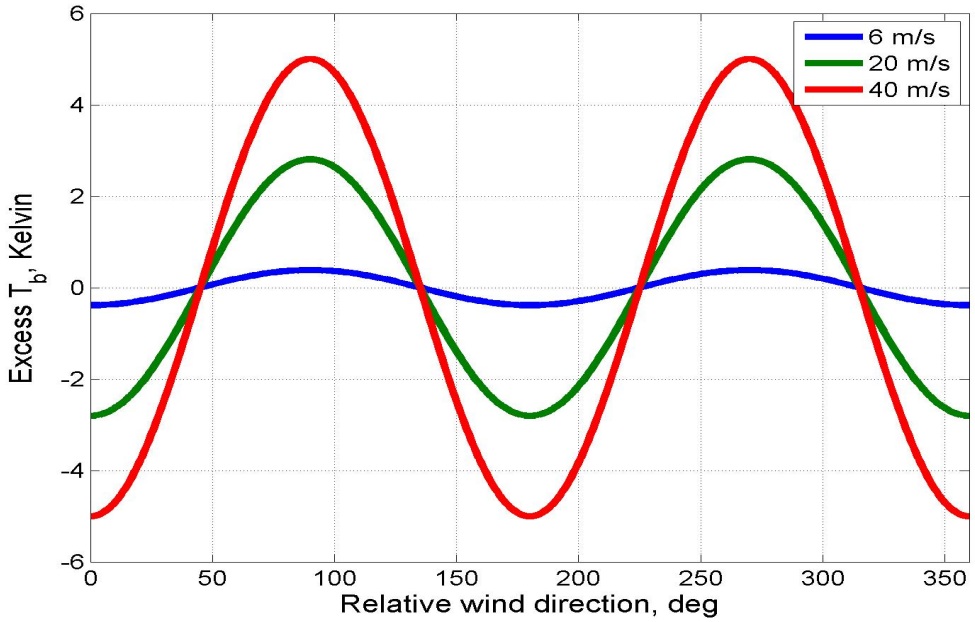

Figure. G.10 CFRSL horizontal excess emissivity for SST = 300 Kelvin, and wind speeds of (6, 20 and 40) m/s at 23.8 GHz and 53 degrees incidence angle.

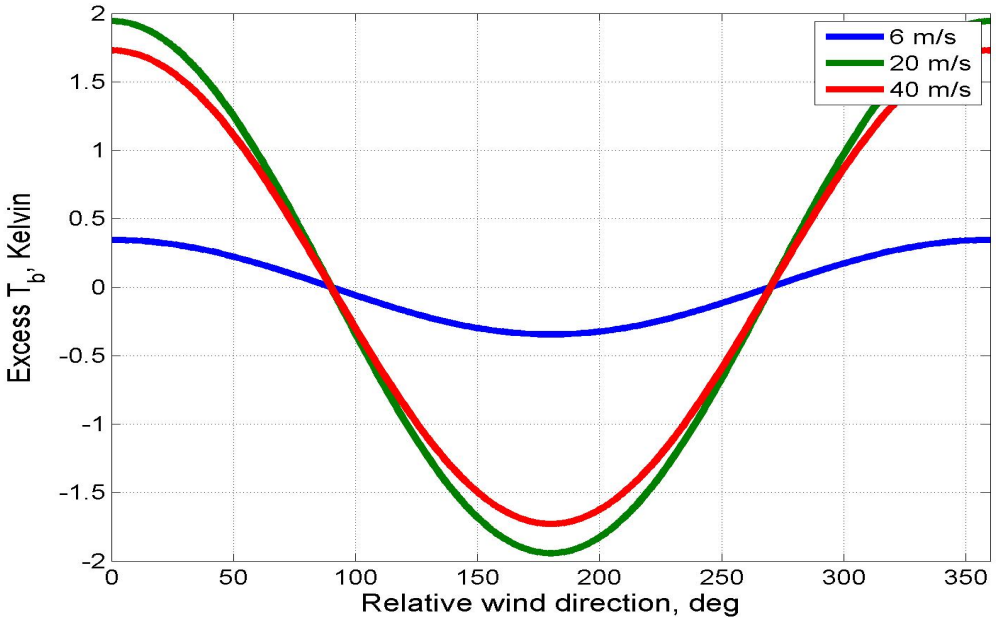

Figure. G.11 CFRSL vertical excess emissivity for SST = 300 Kelvin, and wind speeds of (6, 20 and 40) m/s at 36.5 GHz and 53 degrees incidence angle.

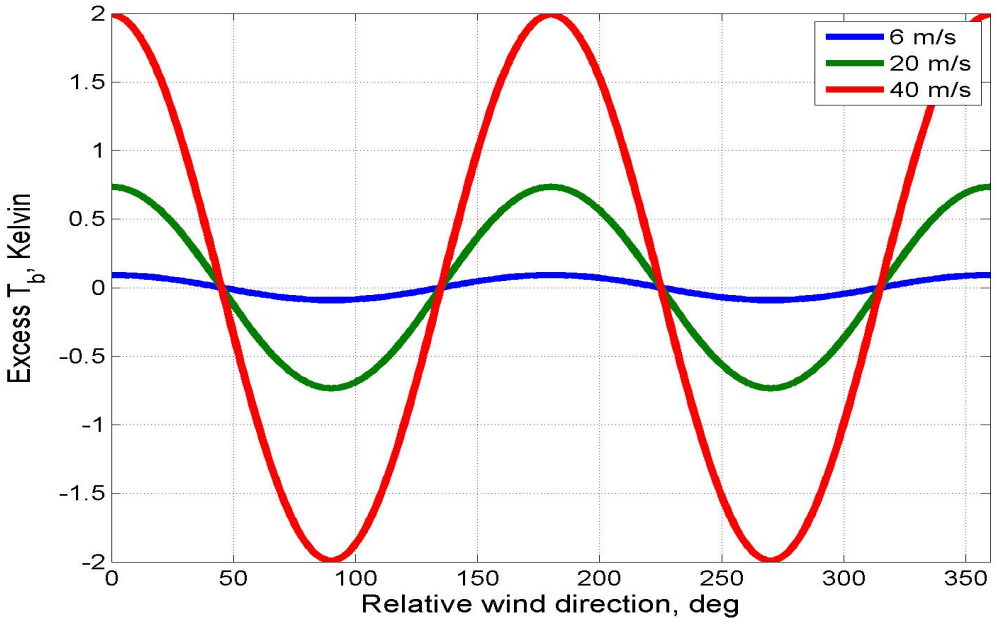

Figure. G.12 CFRSL excess emissivity for SST = 300 Kelvin, and wind speeds of (6, 20 and 40) m/s at 10.7 GHz and nadir incidence angle.

LIST OF REFERENCES

[1] F. Wentz and T. Meissner, "AMSR Ocean Algorithm " Remote Sensing Systems, Santa Rosa, CA November 2 2000.

[2] T. T. Wilheit, "A Model for the Microwave Emissivity of the Ocean's Surface as a Function of Wind Speed," *IEEE Trans. Gesoci. Electronics,* vol. 17, pp. 244-249, 1979.

[3] D. J. Kohn, "Refinement of a Semi-Empirical Model for the Microwave Emissivity of the Sea Surface as a Function of Wind Speed." vol. M.S: Texas A&M University, 1995.

[4] A. Stogryn, "The Apparent Temperature of the Sea at Microwave Frequencies " *IEEE Trans. Antennas Propagat.,* vol. 15, pp. 278-286, 1967.

[5] Eric W. Uhlhorn, Peter G. Black, James L. Franklin, and Alan S. Goldstein, "Hurricane Surface Wind Measurements from an Operational Stepped Frequency Microwave Radiometer," *Mon. Wea. Rev.,* vol. 135, pp. 3070-3085, September 2007.

[6] F. T. Ulaby, R. K. M. Moore, and A. K. Fung, *Microwave Remote Sensing, Active and Passive* vol. 1. Norwood, MA: Artech House Inc, 1981.

[7] A. J. Fresnel, "Sur La Loi Des Modifications Imprimees A La Lumiere Polarise Par Sa Reflexion Totale Dans L'interieur Descorps Transparents," *Ann. Chim.,* vol. 29, pp. 175-87, 1825.

[8] P. Debye, "Polar Molecules," *Chemical Catalog.,* 1929.

[9] L. A. Klein and C. T. Swift, "An Improved Model for the Dielectric Constant of Sea Water at Microwave Frequencies," *IEEE J. Oceanic Eng.,* vol. 2, pp. 104-111, 1977.

[10] A. Stogryn, "Equations for Calculating the Dielectric Constant of Saline Water," *IEEE Trans. Micrwave Theory Tech.,* vol. 19, pp. 733-736, 1971.

[11] J. A. Lane and J. A. Saxton, "Dielectric Dispersion in Pure Polar Liquids at Very High Frequencies," *Proc. Roy. Soc.,* vol. 3, pp. 531-545, 1952.

[12] T. Meissner and F. J. Wentz., "The Complex Dielectric Constant of Pure and Sea Water from Microwave Satellite Observations," *IEEE Trans. of Geoscience and Remote Sensing,* vol. 40, pp. 1836 - 1849, 2004.

[13] J. P. Hollinger, "Passive Microwave Measurements of Sea Surface Roughness," *IEEE Trans. of Geosci. Electron.,* vol. 9, pp. 165-169, 1971.

[14] F. Wentz, "A Two-Scale Scattering Model for Foam-Free Sea Microwave Brightness Temperatures," *Journal of Geophysical Research,* vol. 80, pp. 3441-3446, 1975.

[15] C. S. Cox and W. H. Munk, "Measurement of the Roughness of the Sea Surface from Photographs of the Sun's Glitter," *J. Opt. Soc. Am.,* vol. 44, pp. 838-850, 1954.

[16] J. D. Droppleman, "Apparent Emissivity of Sea Foam," *Journal of Geophysical Research,* vol. 75, pp. 696-698, January 20 1970.

[17] A. Stogryn, "The Emissivity of Sea Foam at Microwave Frequencies," *Journal of Geophysical Research,* vol. 77, pp. 1658-1666, March 20 1972.

[18] L. A. Rose, W. E. Asher, S. C. Reising, P. W. Gaiser, K. M. S. Germain, D. J. Dowgiallo, K. A. Horgan, G. Farquharson, and E. J. Knapp, "Radiometric Measurements of the Microwave Emissivity of Foam " *IEEE Trans. of Geoscience and Remote Sensing,* vol. 40, pp. 2619-2625, December 2002.

[19] S. Padmanabhan, S. C. Reising, W. E. Asher, L. A. Rose, and P. W. Gaiser, "Effects of Foam on Ocean Surface Microwave Emission Inferred from Radiometric Observations of

Reproducible Breaking Waves," *IEEE Trans. of Geoscience and Remote Sensing,* vol. 44, pp. 569-583, 2006.

[20] Adriano Camps, Mercè Vall-llossera, Ramón Villarino, Nicolas Reul, Bertrand Chapron, Ignasi Corbella, M. Núria Duffo, Francesc Torres, Jorge José Miranda, Roberto Sabia, Alessandra Monerris, and R. Rodríguez, "The Emissivity of Foam-Covered Water Surface at L-Band: Theoretical Modeling and Experimental Results from the FROG 2003 Field Experiment," *IEEE Trans. Geoscience and Remote Sensing,* vol. 43, pp. 925-937, 2005.

[21] N. Reul and B. Chapron, "A Model of Sea-Foam Thickness Distribution for Passive Microwave Remote Sensing Applications," *Journal of Geophysical Research,* vol. 108, pp. 19.4 - 19.14, 2003.

[22] E. Monahan and D. K. Woolf, "Comments on Variations of Whitecap Coverage with Wind Stress and Water Temperature," *J. Phys. Oceanogr.,* vol. 19, pp. 706-709, 1989.

[23] S. H. Yueh, R. Kwok, and S. V. Nghiem, "Polarimetric Scattering and Emission Properties of Targets with Reflection Symmetry,," *Radio Sci.,* vol. 29, pp. 1409-1420, 1994.

[24] T. Meissner and F. Wentz, "An Updated Analysis of the Ocean Surface Wind Direction Signal in Passive Microwave Brightness Temperatures," Remote Sensing Systems, Santa Rosa, CA 2000.

[25] N. Tran, D. Vandemark, C. S. Ruf, and B. Chapron, "The Dependence of Nadir Ocean Surface Emissivity on Wind Vector as Measured with Microwave Radiometer," *IEEE Trans. Geoscience and Remote Sensing,* vol. 40, pp. 515-423, 2002.

[26] W. Nordberg, J. Conaway, D.B. Ross, and T.T. Wilheit, "Measurement of Microwave Emission from a Foam Covered Wind Driven Sea," *J. Atmos. Sci.,* vol. 38, pp. 429-433, 1971.

[27] S. T. Wu and A. K. Fung, "A Non-Coherent Model for Microwave Emission and Backscattering From the Sea Surface," *Journal of Geophysical Research,* vol. 77, pp. 5917-5929, 1972.

[28] Wilheit T.T. and M. G. Fowler, "Microwave Radiometric Determination of Wind Speed at the Surface of the Ocean during BESEX," *IEEE Trans. Antennas Propagat.,* vol. AP-25, pp. 111-120, 1977.

[29] T. T. Wilheit and A. T. C. Chang, "An Algorithm for Retrieval of Ocean Surface and Atmospheric Parameters from the Observations of the Scanning Multichannel Microwave Radiometer (SMMR)," *Radio Science,* vol. 15, 1980.

[30] Wilheit T.T., "The Effect of Wind on the Microwave Emission from the Ocean's Surface at 37 GHz," *Journal of Geophysical Research,* vol. 84, 1979.

[31] F. J. Wentz, L. A. Mattox, and S. Peteherych, "New Algorithms for Microwave Measurements of Ocean Winds: Applications to SeaSat and the Special Sensor Microwave Imager," *Journal of Geophysical Research,* vol. 91, pp. 2289-2307, 1986.

[32] M. A. Goodberlet, C.T. Swift, and J.C. Wilkerson, "Remote Sensing of Ocean Surface Winds with the SSM/I," *Journal of Geophysical Research,* vol. 94, pp. 14547-14555, 1989.

[33] P. Schluessel and H. Luthardt, "Surface Wind Speeds over the North Sea from Special Sensor Microwave/Imager Observations," *J. Geophys. Res.,* vol. 96, pp. 4845-4853, 1991.
[34] F. J. Wentz, "Measurement of Oceanic Wind Vector using Satellite Microwave Radiometers," *IEEE Trans. Geosci. and Remote Sensing,* vol. 30, pp. 960-972, 1992.
[35] F. J. Wentz, "A Well-Calibrated Ocean Algorithm for SSM/I," *Journal of Geophysical Research,* vol. 102, pp. 8703-8718, 1997.
[36] L. A. Rose, J. P. Bobak, P. W. Gaiser, M. D. Anguelova, D. J. Dowgiallo, W. E. Asher, S. C. Reising, and S. Padmanabhan, "Azimuthal Variation of the Emissivity of Foam from C and X band Polarimetric Measurements," in *MicroRad*: IEEE, 2006.
[37] C. S. Ruf, A. M. Mims, and C. C. Hennon, "The Dependence of the Microwave Emissivity of the Ocean on Hurricane Force Wind Speed," in *Proc. 28th Conf. on Hurricanes and Tropical Meteorology*, Orlando, FL, 2008.
[38] S. El-Nimri, "An Improved Microwave Radiative Transfer Model for Ocean Emissivity at Hurricane Force Surface Wind Speed," in *EECS*. vol. M.S Orlando: University of Central Florida, 2006.
[39] W. M. Frank, "The structure and energetics of the tropical cyclone I. Storm structure," *Mon. Wea. Rev.,* vol. 105, pp. 1119-1135, 1977.
[40] E. W. Uhlhorn and P. G. Black, "Verification of Remotely Sensed Sea Surface Winds in Hurricanes," *J. Atmos. Oceanic Technol.,* pp. 100-115, Jan. 2003 2003.
[41] R. Villarino, A. Camps, M. Vall-llossera, J. Miranda, and J. Arenas, "Sea Foam Effects On the Brightness Temperature at L-Band," in *International Geoscience and Remote Sensing Symposium IEEE*, Toulouse, France, 2003.
[42] L. Yang, Juhong Zoub, Mingsen Linc, and D. Panb, "Method to Correct both Foam and Rain Effects On Dual Frequency Altimeter Jason1 Wind Measurements in Typhoon Shanshan," *Proc. of SPIE,* vol. 7105, 2008.
[43] Lin Zhou, Leung Tsang, and K.-H. Ding, "Foam Effects on Polarimetric Passive Microwave Remote Sensing of Ocean Wind Vectors," in *International Geoscience and Remote Sensing Symposium IEEE*, Toronto, Canada, 2002, pp. 457- 459.
[44] Q. A. Zheng, V. Klemas, G. S. Hayne, and N. E. Huang, "The Effect of Oceanic Whitecaps and Foams on Pulselimited Radar Altimeters," *Journal of Geophysical Research,* vol. 88, pp. 2571–2578, 1983.
[45] Y. A. Bespalova, V. M. Veselov, and V. Y. Gershenzon, "Determining Surface Wind Velocity by Measurements of Polarization Anisotropy of Natural and Scattered Microwave Radiation," *Issledovaniye Zemli Iz Kosmosa,* pp. 87-94, 1982.
[46] Yuri G. Trokhimovski, Galina A. Bolotnikova, Valentin S. Etkin, Svetlana I. Grechko, and A. V. Kuzmin, "The Dependence of S-Band Sea Surface Brightness and Temperature on Wind Vector at Normal Incidence," *IEEE Trans. Geosci. and Remote Sensing,* vol. 33, pp. 1085-1088, 1995.
[47] S. H. Yueh, W. J. Wilson, F. K. Li, S. V. Nghiem, and W. B. Ricketts, "Polarimetric Measurements of Sea Surface Brightness Temperatures using an Aircraft K-band Radiometer," *IEEE Transactionson Geoscience and Remote Sensing,* vol. 33, pp. 85-92, 1995.

[48] G. Poe and K. S. Germain, "Polarimetric Emission Model of the Sea at Microwave Frequencies, Part I: Theory,," Naval Research Laboratory,, Washington, D.C., 1998.
[49] S. S. Chen, "CBLAST- Hurricane and High-Resolution Fully Coupled Atmosphere-Wave-Ocean Models," in *10th Wave Hindcasting Workshop* Oahu, Hawaii, 2007.
[50] Adrian Callaghan, Gerrit de Leeuw, and L. Cohen, "Observations of Oceanic Whitecap Coverage in the North Atlantic during Gale Force Winds," *Nucleation and Atmospheric Aerosols,* vol. IX, pp. 1088-1092, 2007.
[51] V. G. Bondur and E. A. Sharkov, "Statistical Properties of Whitecaps on a Rough Sea," *Oceanology,* vol. 22, pp. 274-279, 1982.
[52] Adriano Camps, Jordi Font, Mercè Vall-llossera, Carolina Gabarró, Ignasi Corbella, Núria Duffo, Francesc Torres, Sebastián Blanch, Albert Aguasca, Ramón Villarino, Luis Enrique, Jorge José Miranda, Juan José Arenas, Agustí Julià, Jacqueline Etcheto, Vicente Caselles, Alain Weill, Jacqueline Boutin, Stéphanie Contardo, Raquel Niclós, Raúl Rivas, Steven C. Reising, P. Wursteisen, Michael Berger, and Manuel Martín-Neira, "The WISE 2000 and 2001 Field Experiments In Support Of the SMOS Mission: Sea Surface L-Band Brightness Temperature Observations and Their Application to Sea Surface Salinity Retrieval," *IEEE Trans. Geoscience and Remote Sensing,* vol. 42, pp. 804-823, 2004.
[53] M. C. Bailey, R. A. Amarin, J. Johnson, P. Nelson, M. James, D. Simmons, C. S. Ruf, W. L. Jones, and X. Gong, "Multi-Frequency Synthetic Thinned Array Antenna for the Hurricane Imaging Radiometer," *IEEE AP-S Transactions on Antennas and Propagation,* 2010.
[54] Eric W. Uhlhorn, Salem F. El-Nimri, C. S. Ruf, and W. Linwood Jones, "Sea Surface Passive Microwave Measurements At Large Incidence Angle In Hurricane Conditions," in *IEEE GRL*, 2009.
[55] R. A. Amarin, "Hurricane Wind Speed and Rain Rate Measurements Using The Airborne Hurricane Imaging Radiometer (HIRAD)," in *Electrical Engineering and Computer Science*. vol. Ph.D. Orlando: University of Central Florida, 2010.